



IntechOpen

Vibration Analysis and  
Control in Mechanical  
Structures and Wind Energy  
Conversion Systems

*Edited by Francisco Beltran-Carbajal*





---

# **VIBRATION ANALYSIS AND CONTROL IN MECHANICAL STRUCTURES AND WIND ENERGY CONVERSION SYSTEMS**

---

Edited by **Francisco Beltran-Carbajal**

## **Vibration Analysis and Control in Mechanical Structures and Wind Energy Conversion Systems**

<http://dx.doi.org/10.5772/intechopen.68733>

Edited by Francisco Beltran-Carbajal

### **Contributors**

Yasser Boussairi, Abdelmajid Abouloifa, Ibtissam Lachkar, Chaouqi Aouadi, Abdellatif Hamdoun, Carlos Alberto Reusser, Dimitrij Kovriguine, Svetlana Nikitenkova, Abdel Rahman Elbakheit, Dirk Mayer, Sven Herold, Mohamed Soliman

### **© The Editor(s) and the Author(s) 2018**

The rights of the editor(s) and the author(s) have been asserted in accordance with the Copyright, Designs and Patents Act 1988. All rights to the book as a whole are reserved by INTECHOPEN LIMITED. The book as a whole (compilation) cannot be reproduced, distributed or used for commercial or non-commercial purposes without INTECHOPEN LIMITED's written permission. Enquiries concerning the use of the book should be directed to INTECHOPEN LIMITED rights and permissions department ([permissions@intechopen.com](mailto:permissions@intechopen.com)). Violations are liable to prosecution under the governing Copyright Law.



Individual chapters of this publication are distributed under the terms of the Creative Commons Attribution 3.0 Unported License which permits commercial use, distribution and reproduction of the individual chapters, provided the original author(s) and source publication are appropriately acknowledged. If so indicated, certain images may not be included under the Creative Commons license. In such cases users will need to obtain permission from the license holder to reproduce the material. More details and guidelines concerning content reuse and adaptation can be found at <http://www.intechopen.com/copyright-policy.html>.

### **Notice**

Statements and opinions expressed in the chapters are these of the individual contributors and not necessarily those of the editors or publisher. No responsibility is accepted for the accuracy of information contained in the published chapters. The publisher assumes no responsibility for any damage or injury to persons or property arising out of the use of any materials, instructions, methods or ideas contained in the book.

First published in London, United Kingdom, 2018 by IntechOpen

eBook (PDF) Published by IntechOpen, 2019

IntechOpen is the global imprint of INTECHOPEN LIMITED, registered in England and Wales, registration number: 11086078, The Shard, 25th floor, 32 London Bridge Street  
London, SE19SG – United Kingdom

Printed in Croatia

British Library Cataloguing-in-Publication Data

A catalogue record for this book is available from the British Library

Additional hard and PDF copies can be obtained from [orders@intechopen.com](mailto:orders@intechopen.com)

Vibration Analysis and Control in Mechanical Structures and Wind Energy Conversion Systems

Edited by Francisco Beltran-Carbajal

p. cm.

Print ISBN 978-1-78923-056-7

Online ISBN 978-1-78923-057-4

eBook (PDF) ISBN 978-1-83881-349-9

# We are IntechOpen, the first native scientific publisher of Open Access books

3,400+

Open access books available

109,000+

International authors and editors

115M+

Downloads

151

Countries delivered to

Our authors are among the  
Top 1%

most cited scientists

12.2%

Contributors from top 500 universities



WEB OF SCIENCE™

Selection of our books indexed in the Book Citation Index  
in Web of Science™ Core Collection (BKCI)

Interested in publishing with us?  
Contact [book.department@intechopen.com](mailto:book.department@intechopen.com)

Numbers displayed above are based on latest data collected.  
For more information visit [www.intechopen.com](http://www.intechopen.com)





# Meet the editor



Francisco Beltran-Carbajal received his BS degree in Electromechanical Engineering from the Instituto Tecnológico de Zacatepec (México) and his PhD degree in Electrical Engineering (Mechatronics) from the Centro de Investigación y Estudios Avanzados del Instituto Politécnico Nacional (CINVESTAV-IPN) in Mexico City.

He is currently a titular professor in the Energy Department at Universidad Autónoma Metropolitana (UAM), Unidad Azcapotzalco in Mexico City. His main research interests are vibration control, system identification, rotating machinery, mechatronics, and automatic control of electromechanical and electronic systems.





---

# Contents

---

## **Preface XI**

- Chapter 1 **Passive, Adaptive, Active Vibration Control, and Integrated Approaches 1**  
Dirk Mayer and Sven Herold
- Chapter 2 **Design of Robust Digital Pole Placer for Car Active Suspension with Input Constraint 23**  
Hisham M. Soliman, Rashid Al-Abri and Mohammed Albadi
- Chapter 3 **Bifurcation Makes a Wave Resonant Solid-State Gyro Be Stable 41**  
Svetlana Pavlovna Nikitenkova and Dmitry Anatolyevich Kovrigin
- Chapter 4 **Wind-Induced Vibrations to Tall Buildings and Wind Turbines 61**  
Abdel Rahman Elbakheit
- Chapter 5 **State Feedback Nonlinear Control Strategy for Wind Turbine System Driven by Permanent Magnet Synchronous Generator for Maximum Power Extraction and Power Factor Correction 75**  
Yasser Boussairi, Abdelmajid Abouloifa, Ibtissam Lachkar, Chaouqi Aouadi and Abdelatif Hamdoun
- Chapter 6 **DC-Link Control Schemes in Multilevel Converters for WECS 95**  
Carlos A. Reusser



---

## Preface

---

This book focuses on recent and innovative methods on vibration analysis and diverse control design methods for both wind energy conversion systems and vibrating systems. Advances on both theoretical and experimental studies about analysis and control of oscillating systems in several engineering disciplines are discussed. Various control devices are synthesized and implemented for vibration attenuation tasks. The book is addressed to researchers and practitioners on the subject, as well as undergraduate and postgraduate students, other experts, and newcomers seeking more information about the state of the art, new challenges, innovative solutions, and new trends and developments in these areas. The six chapters of the book cover a wide range of interesting issues related to modeling, vibration control, active vehicle suspensions, tuned vibration absorbers, electronically controlled wind energy conversion systems, and other relevant case studies.

The book is organized into six chapters. A brief description of every chapter follows. Chapter 1 describes the fundamentals of active, passive, and adaptive vibration control, including their main advantages and design challenges. An inertial mass device is also proposed to implement both adaptive tuned vibration absorbers and active control systems. Chapter 2 focuses on the state feedback control for an active quarter-car suspension system with control input constraint. The efficiency of the proposed controller is verified in different road tests as step and bump disturbances. Chapter 3 demonstrates that in combining both the primary resonant pumping over the axisymmetric mode of oscillations and the advantages of the principal parametric resonance, a solid-state wave gyro can operate without any feedback at the expense of the natural nonlinearity of the resonator in a post-bifurcation regime. Chapter 4 highlights the novelty of aerodynamic design and optimization in providing vibration-free tall buildings and wind turbines with added savings that otherwise be incurred by the adoption of costly structural and/or supplementary damping technologies. The current state of the art in wind vibrations is reviewed, together with key factors to study the control vibration in tall buildings and wind turbines. Chapter 5 addresses the problem of controlling the complete chain of the wind turbine system using the permanent magnet synchronous generator connected with the distribution network through AC/DC/AC converters. Chapter 6 focuses on full-scale power converters employed with squirrel cage, permanent magnet, and wound rotor synchronous generators in diverse configurations of wind energy conversion systems. The main advantages and drawbacks of classical multilevel converter topologies are analyzed, in terms of their DC-link voltage stability capability and different approaches to DC-link control and to new converter topologies.

Finally, I would like to express my sincere gratitude to all the authors for their excellent contributions, which will be valuable to the readers. I would also like to thank the editorial staff of InTechOpen for their great effort and support in the process of edition and publication of the book. I truly hope that this book can be useful and inspiring for contributing to the technology development, new academic and industrial research, and many inventions and innovations in vibration engineering, wind energy conversion systems, and control of oscillating systems.

**Dr. Francisco Beltran-Carbajal**  
Universidad Autónoma Metropolitana  
Unidad Azcapotzalco  
Departamento de Energía  
Mexico

---

# Passive, Adaptive, Active Vibration Control, and Integrated Approaches

---

Dirk Mayer and Sven Herold

Additional information is available at the end of the chapter

<http://dx.doi.org/10.5772/intechopen.71838>

---

## Abstract

Passive vibration control solutions like tuned vibration absorbers are often limited to tackle a single structural resonance or a specific disturbance frequency. Active vibration control systems can overcome these limitations, yet requiring continuously electrical energy for a sufficient performance. Thus, in some cases, a passive vibration control system is still preferable. Yet, the integration of active elements enables adaptation of the system parameters, for instance, the resonance of a tuned vibration absorber. These adaptive or semi-active systems only require external energy for the adaptation, while the compensating forces are generated by the inertia of the absorber's mass. In this contribution, the fundamentals of active, passive, and adaptive vibration control are briefly summarized and compared regarding their main advantages and design challenges. In the second part, a design of an inertial mass device with integrated piezoelectric actuators is presented. By applying a lever mechanism, the stiffness of the inertial mass device can be tuned even to very low frequencies. The device can be used to implement both adaptive tuned vibration absorbers and active control systems. In the last section of the chapter, the device is used in an experiment for vibration control of a large elastic structure. The setup is used to demonstrate different strategies for the realization of a vibration control system and the integration of different vibration control strategies.

**Keywords:** vibration control, active vibration control, passive vibration control, piezoelectric actuators, adaptive vibration absorbers

---

## 1. Introduction

Tuned vibration absorbers (TVA) and tuned mass dampers (TMD) are used since the beginning of the twentieth century to reduce disturbing vibrations [1]. Basically, this method uses an inertial mass that is elastically coupled to the vibrating host structure [2]. This resonant spring-mass

---

system can be tuned to certain resonance frequencies of the host structure (**Figure 1**). Then, the device is usually referred to as tuned mass damper (TMD), which is frequently applied to elastic infrastructure objects like towers or bridges. For large objects, several TMDs are distributed among the structure [3].

When the oscillator is tuned to a harmonic disturbance frequency, it is called tuned vibration absorber or vibration neutralizer [4]. Potential applications range from Optical Disc Drives, using an absorber mass of about 40 g [5] to vibrations of ship engines, requiring over 10 tons of oscillating mass [6]. The performance of these devices is mainly limited by the precise tuning to the target frequency. If a certain bandwidth is to be tackled, a high inertial mass has to be used, which usually prevents the application of TVAs in such cases.

In this chapter, several improvements to the traditional passive vibration absorber are introduced that have been made over the last decades, ranging from semi-active or adaptive to active dynamic systems (**Figure 2**).

In the next section, the basics of the different vibration control systems are summarized and examples for realized systems are given. In the last two sections, a system that can be used for

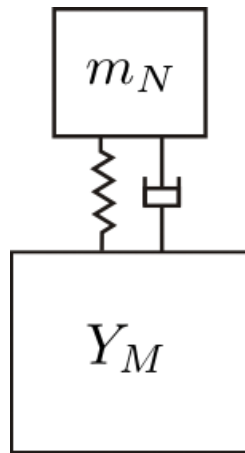


**Figure 1.** Generic vibration control set up with a passive TVA.

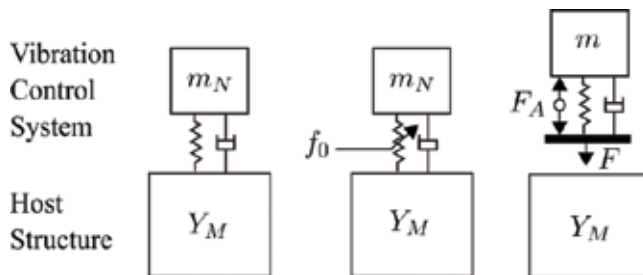


**Figure 2.** Vibration control systems—passive, adaptive, and active.

adaptive and active vibration control methods is presented and the application to an elastic vibrating structure is investigated.

## 2. Passive, adaptive, and active vibration control systems

### 2.1. Passive vibration control with tuned vibration absorbers

To illustrate the working principle of a passive TVA, the generic example from **Figure 1** is studied. The vibrating host structure is represented by a mechanical mobility  $Y_M$ . If the structure can be treated as a vibrating mass element of mass  $M$ , i.e., away from its resonance frequencies, the mobility reads [7]:

$$Y_m(s) = \frac{1}{sM} \tag{1}$$

The neutralizer is described by its mass  $m_N$ , resonance frequency  $\omega_0$ , and damping coefficient  $\theta$ . Then, its input mobility at the base can be derived to:

$$Y_N(s) = \frac{1}{m_N} \frac{s^2 + s 2 \theta \omega_0 + \omega_0^2}{s^2 2 \theta \omega_0 + s \omega_0^2} \tag{2}$$

The connection of both systems is represented by:

$$Y(s) = \frac{Y_m(s)Y_N(s)}{Y_m(s) + Y_N(s)} = \frac{s^2 + s 2 \theta \omega_0 + \omega_0^2}{sM (s^2 + s2\theta\omega_0 + \omega_0^2) + m_N (s\omega_0^2 + s^22\theta\omega_0^2)} \tag{3}$$

Obviously, the mobility transfer function has a pair of conjugated complex zeros that match the resonance of the TVA. If the TVA is fully undamped, the mobility of the system at the resonance of the TVA turns to zero, i.e., complete cancellation of vibrations. It can be shown that the performance of the passive TVA is directly proportional to the mass ratio  $m_N/M$ , while increased damping has the contrary effect [8]. This issue is illustrated in **Figure 3** (left). Also the bandwidth of the absorption effect increases with a larger absorber mass. However, in most practical applications, a mass ratio of  $\frac{1}{2}$  will not be acceptable, so the passive TVA is restricted to situations where the disturbance frequency is known to be constant over time or where the added mass of a heavy TVA does not matter.

When the relevant frequency range of the host structure contains a resonance, the mobility formulation for  $Y_m$  becomes:

$$Y_m = \frac{s}{s^2M + 2\theta_H \omega_{0,H} s + \omega_{0,H}^2}, \tag{4}$$

where  $\omega_{0,H}$  is the resonance and  $\theta_H$  is the damping coefficient of the host structure. The TVA is then used as a Tuned Mass Damper (TMD). The main difference is that a significant damping is needed to reach optimal vibration control performance [2]. This effect is demonstrated in

**Figure 3** (right). Also, the TMD is usually designed with a lower mass ratio. In the given example, a ratio of  $\frac{m_N}{M} = 0.1$  already provides a sufficient vibration reduction performance. It should be noted that the formulae for optimal tuning of a TMD are restricted for the application example of a single-degree-of-freedom oscillator excited by a harmonic force. In case of other excitation mechanisms like base acceleration, which is relevant for seismic vibration reduction, other TMD parameter values might provide the optimal vibration reduction performance [9]. For structures with several resonances or larger objects which cannot be treated as simple point mass oscillators any more, the design of distributed TMD systems requires some advanced methods like numerical optimization [3].

**2.2. Adaptive tuned vibration absorbers**

Adaptive tuned vibration absorbers have been proposed to overcome this weakness of passive TVAs. By using actuating elements, the resonance frequency of the absorber can be adjusted. In turn, an adaptive TVA can be designed with a smaller inertial mass [10]. In the last decades, numerous concepts have been investigated [11–14], but the designs can be traced back to some basic principles of adaptation [15] (**Table 1**).

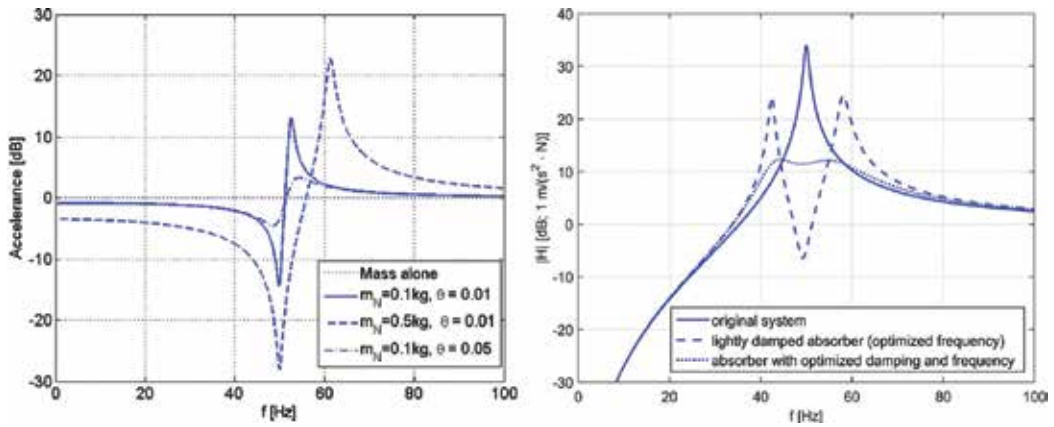


**Figure 3.** Accelerance of a 1 kg mass with a TVA tuned to 50 Hz (left); and a 50 Hz mass-spring-system with a TMD (right).

Concept	Static prestress	Variable geometry	Dynamic forces
Actuator principle	Static – high force	Static – high stroke	Dynamic force actuator
Actuator types	Motor, piezoelectric,...	Motor, shape memory alloy wires,...	Piezoelectric, electrodynamic

**Table 1.** Basic concepts for the realization of adaptive tuned vibration absorbers [15].



A common approach to alter the resonance frequency of a mechanical oscillator is the adjustment of the mechanical stiffness via the geometry of the spring element; for instance, by moving the inertial mass on a bending beam, which adjusts the effective beam length, as demonstrated for vibration control at ship engines [16]. The most advanced concept is the application of an active dynamic control loop for the adjustment of the resonance frequency. The principle can be briefly explained with a TVA represented by a simple mechanical oscillator (**Figure 4**), which can be excited by an integrated actuation force  $F_A$ . The differential equation of this system reads:

$$m_N \ddot{x} + d \dot{x} + kx = F_A \tag{5}$$

where  $d$  is the damping coefficient and  $k$  is the stiffness of the oscillator. The feedback loop is closed by using the acceleration  $\ddot{x}$  as the control input and the actuation force as output. If a simple proportional controller

$$G(s) = g \tag{6}$$

is applied, Eq. (5) can be reformulated to:

$$(m_N - g)\ddot{x} + d \dot{x} + kx = 0 \tag{7}$$

Thus, by feeding back forces proportional to the acceleration of the mass, the effective mass of the system can be altered. Similarly, by using an integral controller, a velocity feedback loop can be realized to adjust the damping of the system. In order to enhance the vibration absorption effect, active removal of system damping can be considered [8]. Also, a further integration can be implemented in order to obtain the position of the mass. By feeding back this signal, the stiffness of the absorber can be adjusted [17].

The frequency range that can be covered by the adaptation mechanism is a key performance parameter for an adaptive TVA. As studied in [15], the active control system is limited by the stability margins of the control loop. These margins are mainly defined by the inherent phase lag of many signal processing components, but also by the geometrical arrangement of the sensor and the actuator.

By applying an electrical shunt circuit to the piezoelectric element, the stiffness can be varied without using a sensor component [18]. By using active circuits to realize negative capacitances, a broad adaptation frequency range can be realized. However, the active circuits have

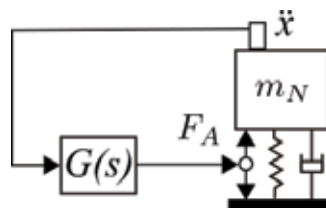


**Figure 4.** Feedback control to adjust the resonance frequency.

to be designed with respect to the high voltages that occur at the piezoelectric elements, which still remain a challenge [19].

### 2.3. Active systems with inertial mass actuators

#### 2.3.1. Inertial mass actuators

Most versatile are active vibration control systems using dynamic actuation [20]. In this case, the force is generated by an inertial mass, which is excited by an active element. To enable a broad band actuation, the inertial mass is usually mounted with soft springs to the host structure, which causes a resonance in the system. Thus, the resulting force exciting the host structure exhibits a dynamic behavior, and the inertial mass actuator can be treated as a constant force generator only when being driven well above the resonance frequency. The frequency response of an inertial mass actuator with a mass  $m$ , resonance frequency  $\omega_0$ , damping coefficient  $\theta$ , and an internal actuation force  $F_A$  reads:

$$\frac{F(s)}{F_{A(s)}} = \frac{s^2}{s^2 + 2\theta\omega_0^2 s + \omega_0^2}. \quad (8)$$

A simple example of an inertial mass actuator with a resonance frequency of 10 Hz is shown in **Figure 5**.

Inertial mass actuators have been used for active vibration control in cars [21], trains [22], or building floors [23]. For very large structure like wind turbines actuation for the first dominating mode with a large force is required. Then, the concepts of the TMD and the inertial mass

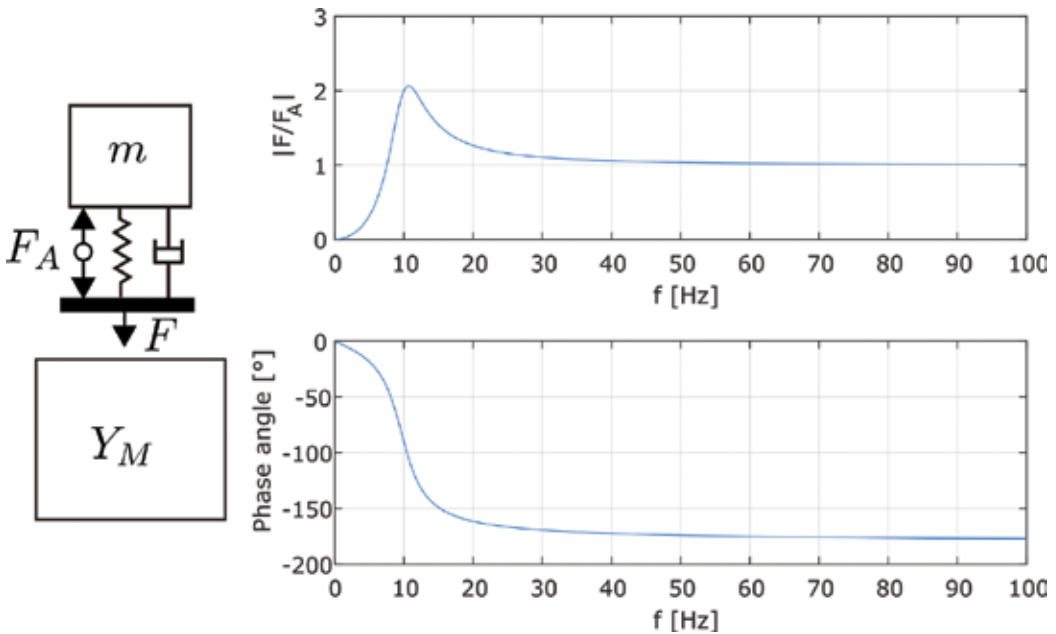


**Figure 5.** Basic model of an inertial mass actuator and its frequency response function.

actuator converge to the active tuned mass damper [24]. Recent developments also treat nonlinearities in the host structures by extending the theoretical considerations for tuning of the system and the control law [26].

If the host structure is a non-linearly oscillating system, extended considerations are necessary in the design of those systems.

Mostly, electrodynamic actuation is preferred, because it enables a straightforward system design for a low resonance frequency.

Still, some work is dedicated to the integration of piezoelectric actuation. Since piezoelectric actuators possess very high resonance frequencies, proper designs have to be found that make such stiff actuators applicable for an oscillator with a low resonance frequency. However, the advantage of using piezoelectric actuation is the capability of the piezoelectric actuators to function as structural elements and partly carry the inertial mass, enabling compact systems with less movable parts.

Piezoelectric TVA systems can also be used in a hybrid mode. While being tuned to one resonance frequency, they can be actively driven at higher frequencies and work as inertial mass actuators [25].

### 2.3.2. Control methods

When the inertial mass actuator is driven well above its resonance frequency, it represents an ideal force generator. Thus, arbitrary active vibration control methods are applicable. Two basic concepts should be briefly repeated (**Figure 6**).

The feedback control system (**Figure 6**, left) is often applied to implement skyhook damping or other concepts which aim at influencing the characteristics of the host structure. Further details on control methods like velocity feedback or positive position feedback can be found in [27].

Feedforward control is usually implemented with adaptive digital filters [28]. The main field of application for active control of vibrations is narrowband or harmonic disturbance forces exciting the host structure. To compensate those, a reference signal with the same frequency is

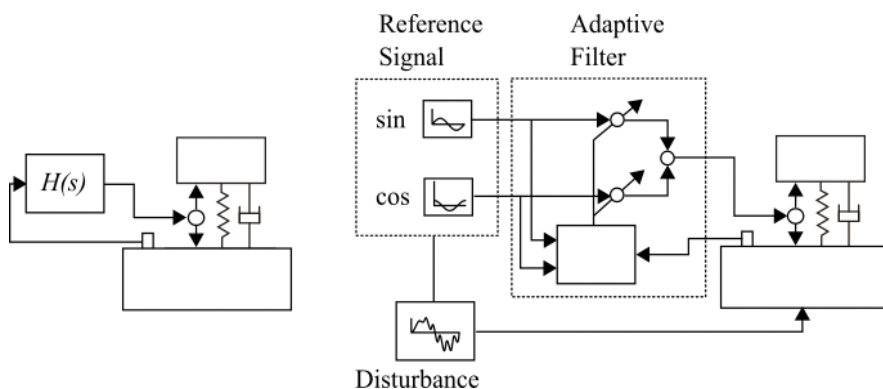


**Figure 6.** Feedback and feedforward control of an inertial mass actuator.

generated and filtered in order to match the phase angle and amplitude for an optimal suppression of the disturbance.

## 2.4. Comparison of the methods

To illustrate the characteristics of the introduced vibration control systems, the basic example (**Figure 1**) is used once more [7]. As disturbance, a harmonic excitation force of 1 N with slowly sweeping frequency between 40 and 60 Hz is considered. As a performance indicator, the RMS of the acceleration of the host structure is used. A passive TVA, an adaptive TVA, and an active system with an inertial mass actuator driven by an adaptive FXLMS algorithm are compared. The mechanical parameters of the different devices are summarized in (**Table 2**).

The result summarizing numerical simulations of all three configurations is presented in **Figure 7**. Obviously, the active system shows the best performance using just a moderate

System	Passive	Adaptive	Active
Resonance frequency [Hz]	50	50 (+/ 5Hz adaptation range)	10
Mass [kg]	0.5	0.1	0.1
Damping coefficient [-]	0.01	0.01	0.03

**Table 2.** Parameters of the compared vibration control systems (from [7]).

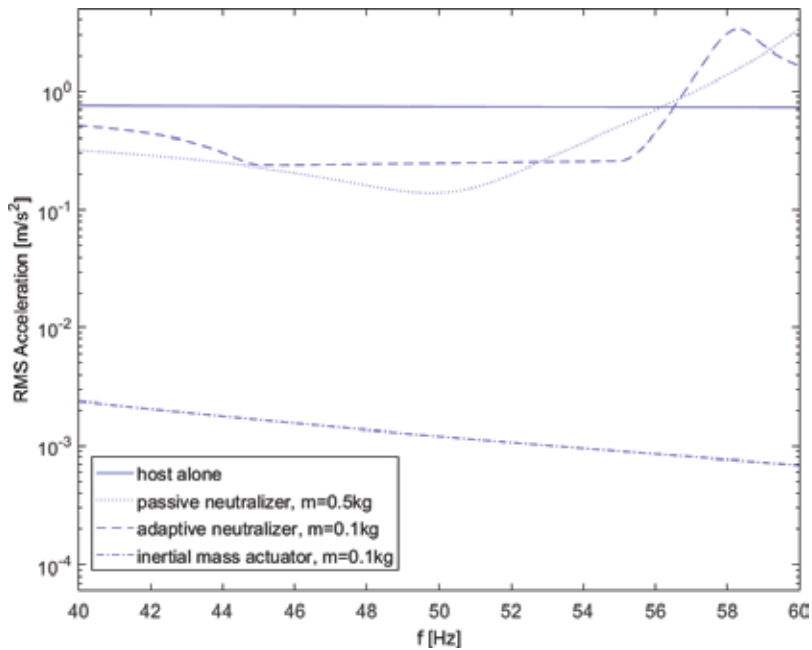


**Figure 7.** RMS acceleration of a vibrating host structure with different vibration control systems.

System	Passive	Adaptive	Active
Vibration reduction	Medium	Medium	High
System complexity	Low	Medium	High
Energy supply	None	During adaptation (depending to the concept)	Continuously
Added mass	High	Low	Low
Bandwidth	Low	Medium	High

**Table 3.** Comparison of passive, adaptive and active control systems.

additional mass, however at the expense of a complex system set up using digital signal processing and a dynamic actuation, which can cause issues when scaling the system for vibration control of very large structures. The adaptive and the passive vibration absorber cause similar vibration reduction; however, the passive system uses a five times higher mass than the adaptive (**Figure 7**).

Summarizing, the solution for an optimal vibration control system depends to the given vibration problem and the respective requirements and restrictions like allowed amount of added mass, possibility for energy supply, or the characteristics of the disturbance (**Table 3**).

This motivated the development of a vibration control system that can be used to realize passive, adaptive, and active vibration control systems, which will be introduced in the next section. This might be especially useful for prototyping purposes when an evaluation of different system concepts is needed. Furthermore, the system can be used to implement hybrid systems that combine passive, adaptive and active control.

### 3. Design of a hybrid piezoelectric absorber and inertial mass actuator

The vibration control device introduced here utilizes piezoelectric actuators due to their ability to carry high static mechanical loads while providing static and dynamic actuation forces. This should enable a multifunctional system. The design follows the well-known mechanical oscillator consisting of a bending beam as spring element and a tip mass. In parallel to the bending beam, two piezoelectric stack actuators are connecting the base and the tip mass (**Figure 6**).

In phase static actuation or static preloads by the screws apply tensile forces to the bending beam, which alters the stiffness and enables adaptation of the resonance frequency. Alternatively, out-of-phase dynamic operation of the piezoelectric actuators generates bending movements of the beam, which causes transverse dynamic forces at the base of the absorber. More details on the design can be found in [29, 30].

#### 3.1. Adaptation by static preloading

The adaptation by static preloading can be described by the differential equation for the axially loaded Euler-Bernoulli beam:

$$EIw'''' + F_N w'' = 0 \quad (9)$$

Here, additional beam stiffness is generated by the tensile force  $F_N$ . This force can be provided mechanically by the preloading screws or electrically by applying static voltages to the piezoelectric actuators. To compute the tensile beam force, a serial connection of actuators and beam with the respective stiffness's  $k_A$  and  $k_{N,b}$  has to be considered. The overall longitudinal stiffness  $k_{N,eff}$  of this configuration is defined by:

$$k_{N,eff} = \frac{2k_A k_{N,b}}{2k_A + k_{N,b}} \quad (10)$$

Thus, for the mechanical preloading the force is evaluated by:

$$F_N = k_{N,eff} u_s \quad \text{with} \quad u_s = \eta \alpha \quad (11)$$

Hereby, the displacement of the screw  $u_s$  is defined by the product of their thread pitch  $\eta$  and turning angle  $\alpha$ . For the electrical preloading the tensile force is calculated differently to Eq. (11):

$$F_N = k_{N,eff} u_{el} \quad \text{with} \quad u_{el} = d_{33} n_A U_{el} \quad (12)$$

The product of the electro-mechanical constant  $d_{33}$ , the number of actuator layers  $n_a$  and electrical voltage  $U_{el}$  yield to piezo actuator's displacement  $u_{el}$ .

To solve the aforementioned differential Eq. (9), an adequate trial function is chosen and the boundary conditions are defined. From this, follows the system of equations to be solved to gain the constants of the trial function [30].

Also, the effective transverse stiffness of the beam  $k_{t,eff}$  w.r.t. to the position  $x = l + a$  (refer to **Figure 8**) is derived from this solution:

$$k_{t,eff} = \left( \frac{w(x = l + a)}{F} \right)^{-1} \quad (13)$$

Considering a tip mass at position  $x = l + a$ , the natural frequency of the system can be evaluated depending on the tensile preload. In Section 3.3, the analytical and experimental results are compared. A good match is observed for both, mechanical and electrical tuning.

### 3.2. Generation of dynamic forces

As mentioned above, the piezo actuators can be used in dynamic operation (out of phase) to generate transverse forces. This enables the system to work as an inertial mass actuator at frequencies above its first natural frequency. To estimate the characteristics of the force  $F$  generated in transverse direction, a simplified analytical model with respect to the actuator force is used. Since the inertial mass at the tip is expected to be much heavier than the actuation unit depicted in **Figure 8**, the mass of the latter is neglected here in order to simplify the calculations using again the theory of the Euler beam. The system can be represented by a

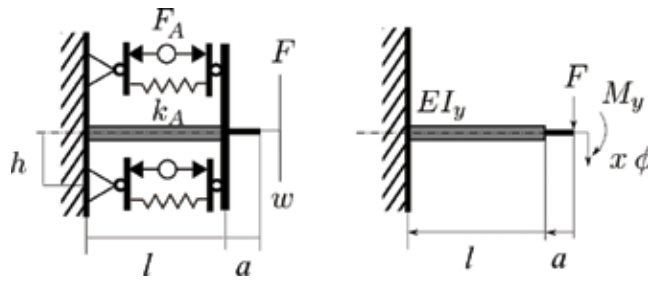


**Figure 8.** Mechanical model of the vibration control device.

bending beam with a tip force  $F$  and moment  $M_y$ . The respective tip displacement  $w$  and angle  $w'$  can be found too by solving Eq. (9). The moment  $M_y$  at the tip due to the actuator force  $F_A$  and the restoring force of the actuator stiffness  $k_A$  can be expressed by:

$$M_y = 2 (h F_A - k_A h^2 w'(x = l)) \quad (14)$$

In order to include the geometry of the mass, the distance from the end of the beam to the center of gravity of the mass is defined by  $a$  (refer to **Figure 8**). In Eq. (15), the displacement  $w(x = l + a)$  is evaluated

$$w(x = l + a) = w(x = l) + a w'(x = l) \quad (15)$$

The free stroke at this point due to the actuator force  $F_A$  can be calculated by setting the force  $F$  to zero and using the solution of Eq. (9) for  $w(x = l)$  and  $w'(x = l)$  and applying this to Eqs. (14) and (15).

In a similar manner, the stiffness  $k = F/w$  can be calculated by setting  $F_A = 0$ . The block force of the actuator system can be calculated by multiplying the free stroke due to out-of-phase actuator excitation and the stiffness of the system:

$$F = k w(x = l + a) \quad (16)$$

Hence, considering a tip mass  $m$  at position  $x = l + a$  all quantities are defined in order to calculate the dynamic behavior of the system due to actuator excitation.

### 3.3. Experimental characterization

According to the sketch (**Figure 9**) a prototype was built that is shown in **Figure 10**.

A thin beam is clamped between two steel blocks, which represents the mounting of the inertial mass actuator. The width of the beam is large compared to its length to prevent torsion. The whole pattern of the mounting is suited for a connection to a shaker, a heavy breadboard or the test structure addressed subsequently. On the other side of the beam, the inertial mass is attached. Two simple steel blocks are used to realize the clamping of the beam, which can be changed easily for experiments. For assembling the piezoelectric actuators the beam is

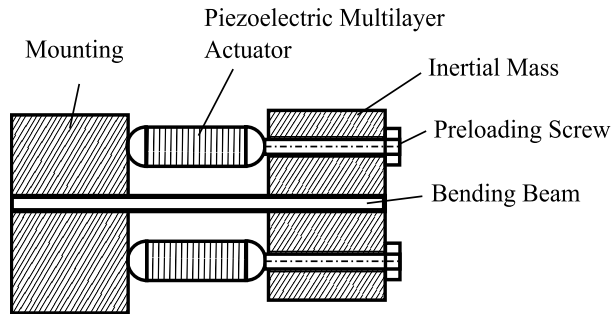


**Figure 9.** Design of the vibration control device.

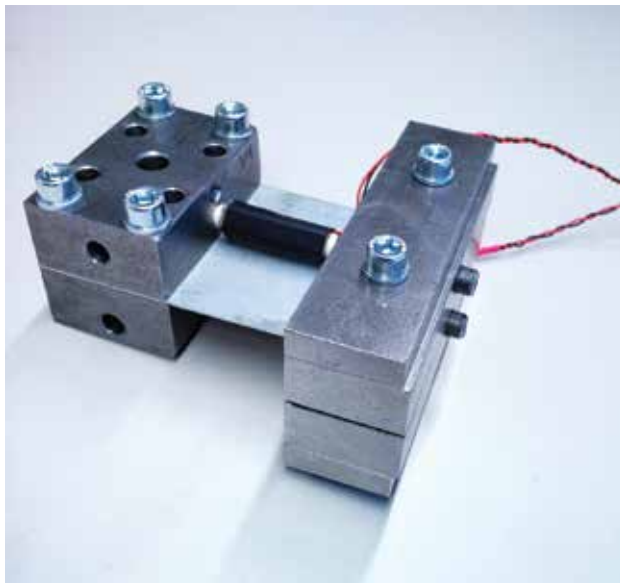


**Figure 10.** Implemented prototype of the adaptive vibration absorber/inertial mass actuator.

equipped with slotted holes. Monolithic multilayer actuators by CeramTec with a base area of  $7.6 \times 7.1$  mm and a length of 30 mm are integrated. On both sides of the piezoelectric actuators, spherical ceramic caps are glued to reduce damaging bending and shear forces. To ensure the force transmission of the actuators and to avoid loosening and, therefore, the non-linear behavior, the actuators have to be pre-loaded. This is done by screws in the two masses next to the beam with a distance of 7.5 mm to the beam's surface. The tips of the pre-loading screws are concave as counterparts of the actuator's ceramic caps. There are corresponding holes at the mounting at the same distance from the beam. This prevents shifting of the piezoelectric actuators in operation. The parameters for the actuator system are depicted in **Table 4**.



Quantity	Symbol	Value	Unit
Beam			
Length	$l$	41.5	mm
Width	$b$	60	mm
Thickness	$d$	0.5	mm
Young's modulus	$E$	$2.2 \cdot 10^{11}$	$\text{N/m}^{-2}$
Mass			
Mass	$m$	1.078	kg
Actuator			
Stiffness	$k_A$	$42 \cdot 10^6$	$\text{Nm}^{-1}$
Max. block force	$F_{B,\text{max}}$	2000	N

**Table 4.** Parameters of the actuator systems.

### 3.3.1. Adaptation of the resonance frequency by static preloads

To analyze the dynamic characteristics of the inertial mass actuator, tests were performed. The whole actuator was mounted to a rigid, heavy base plate which can be treated as an infinitely small mechanical admittance in the considered frequency range (**Figure 11**). The tip mass was instrumented with an accelerometer and excited by an impulse hammer in order to gain the resonance frequencies by evaluating the respective frequency response functions depending on both conditions—mechanical and electrical preload.

Exemplarily the frequency responses for electrical tuning are depicted in **Figure 12**. Obviously, the effect of preloading is significant and has to be taken into account. The analytical model which is introduced in the preceding section is validated by the experimental results. Some differences between experimental and analytical frequency responses can be observed for very low DC voltages, where the absorber does not exhibit perfect characteristics of a single-degree-of-freedom oscillator. This could be caused by a poor mechanical coupling between the piezo stacks and the structure when nearly no pre-load is applied. For very high pre-loads around 140 V, the model predicts higher tuning effects than measured in the experiment (**Figure 12**). In this case, the analytical model might not perfectly predict the contact characteristics of the ball joints, which can be non-linear for high mechanical loads.

The comparison of the measured and the calculated resonance frequencies is shown in **Figure 13** for both cases (mechanical and electrical tuning). By mechanical preloading a larger frequency shift compared to electrical preloading is realized. This can be explained by the limited blocking force of the piezo actuators. However, a good match between the experimental values for the resonance frequencies and the calculated results is observed for both cases.

The performance of both tuning concepts is comparable to adaptive absorbers, which use motors for the variation of the spring geometry investigated in preliminary work [15].

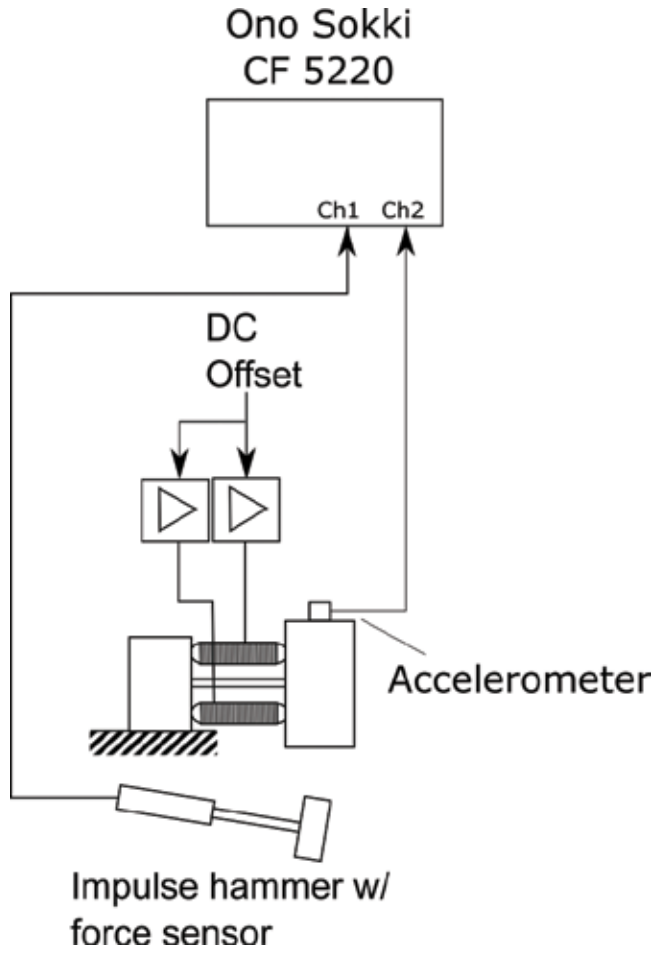


Figure 11. Test set up for the dynamic analysis of the adaptive vibration absorber.

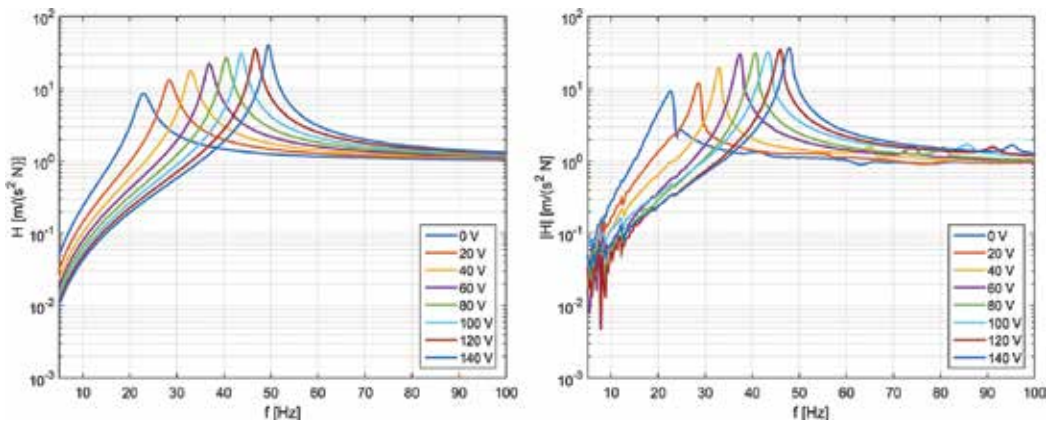


Figure 12. Frequency response functions of the adaptive vibration absorber for different DC voltages (electrical tuning) - simulation results (left) and experimental results (right).

### 3.3.2. Dynamic force generation

For the evaluation active force generated by the device, the piezoelectric actuators were driven with a swept sine signal by the analyzer. A simple analogue circuit realizes an out of phase driving signal for one of the actuators in order to excite the bending mode of the actuator system to produce transverse forces, and the acceleration of the tip mass was measured (Figure 14). Since the mounting can be assumed to be rigid, the block force can be directly derived from the acceleration and the mass.

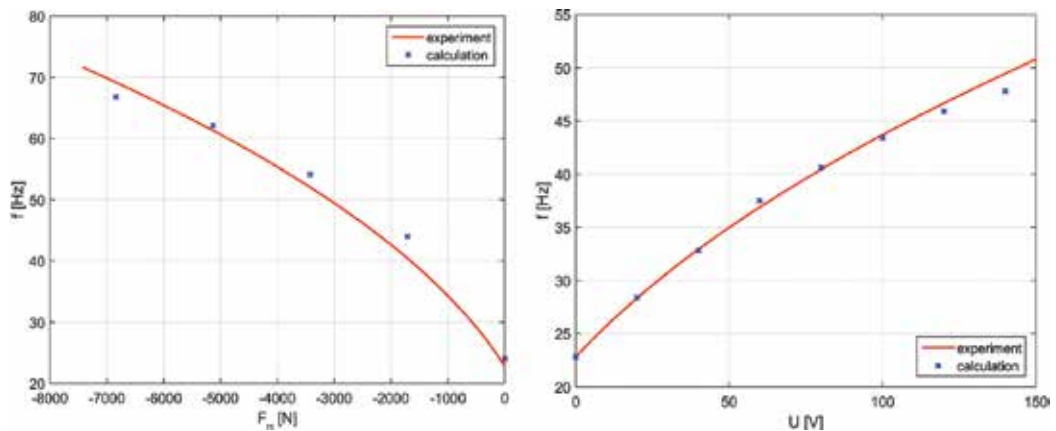


Figure 13. Variation of resonance frequency by mechanical (left) and electrical preloading (right).

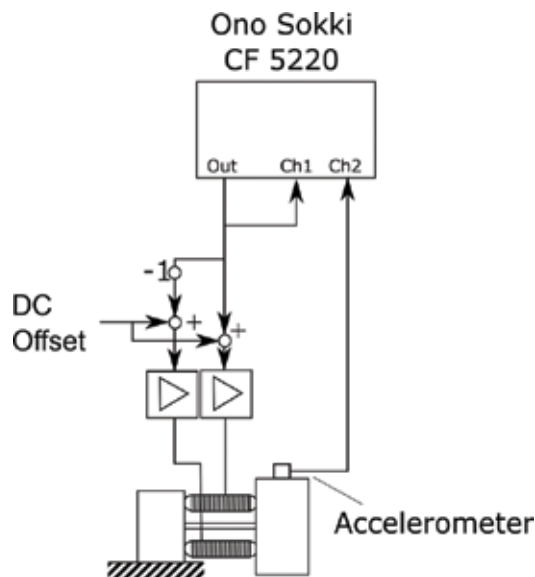
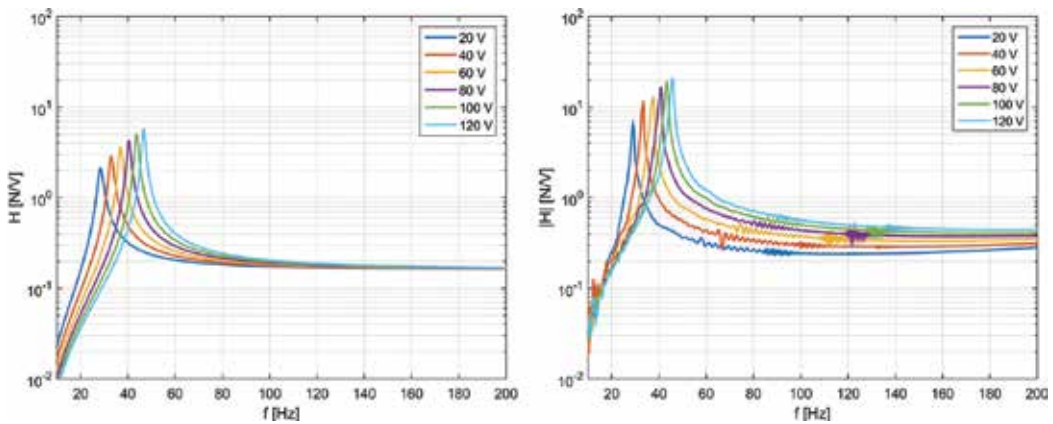


Figure 14. Test set up for the measurement of the dynamic block force of the actuator.



**Figure 15.** Calculation (left) and measurement (right) of the dynamic block force of the actuator.

For this test, different preloads from 20 to 120  $V_{DC}$  were applied to the actuators. The resulting frequency responses between applied driving voltage and the generated force show the expected characteristics (**Figure 15**).

In the frequency range above the first resonance and 250 Hz, no further resonances are excited. However, it was observed that, compared to the analytical frequency responses, the measured ones are influenced by the pre-load. Additionally, the block force is underestimated by the analytical frequency responses. Above the resonance the block force increases slightly with the pre-loading voltage. This might be caused by a non-linearity in the piezoelectric elements, i.e., a dependency of the piezoelectric constant to the pre-load. In the next section, the application of the actuator system to a truss structure is conducted. Therefore, the adaptive and active mode of the actuator system is used simultaneously in order to attenuate unwanted vibration in different frequency regions.

#### 4. Application to an elastic truss structure

To evaluate the performance in an active vibration control system, the actuator was mounted to a lightweight truss structure (**Figure 16**). The actuator was instrumented with accelerometers at its base and at the inertial mass.

In the first step, the adaptive absorber was tuned by mechanical pre-load to a structural mode, which resulted in a vibration absorption effect at 43 Hz (**Figure 17**). This effect was enhanced by choosing an additional electrical pre-load of 50  $V_{DC}$ , which resulted in an absorption frequency of 50 Hz. Although this frequency does not match the structural resonance at 48 Hz exactly, this configuration served well as a basis for adjusting the active control system.

In the next step, the active control system was set up and tuned. Two control loops were implemented successively and connected (**Figure 18**). First, an active velocity feedback loop  $H_v(s)$  was used to enhance the damping of the inertial mass actuator, which caused the better

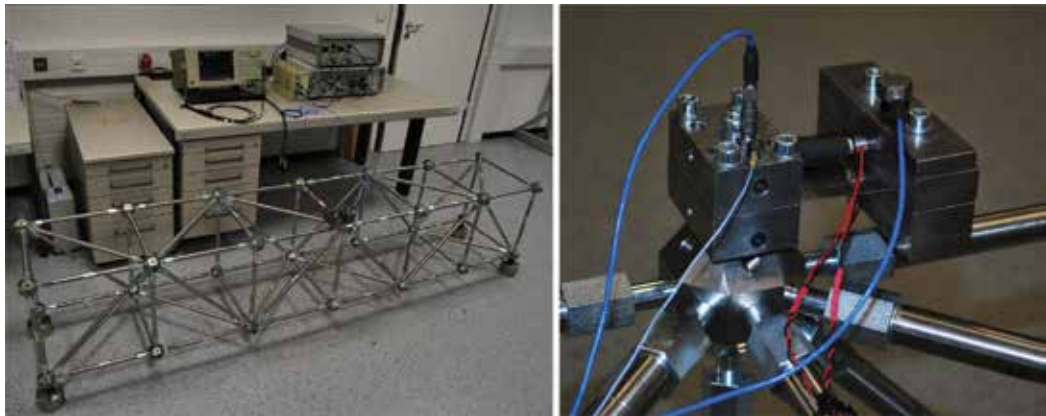


Figure 16. Test set up for the active control experiment (left) and detail of the actuator instrumentation (right).

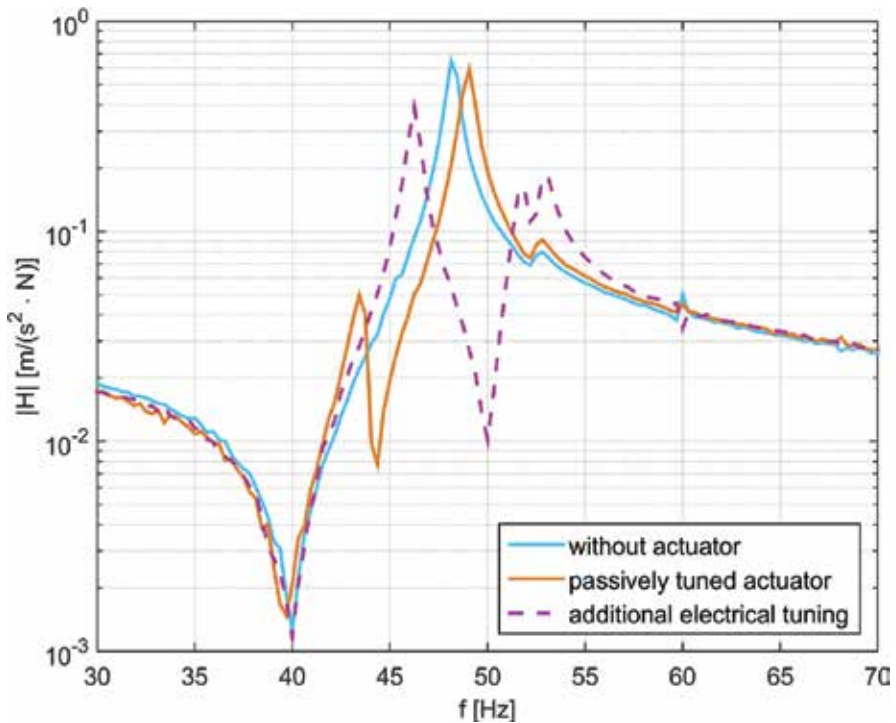


Figure 17. Tuning of the adaptive absorber to the first elastic mode of the truss.

performance of the absorption at the first mode at 48 Hz and a higher robustness against the interaction between different control loops. In order to derive the dynamic velocity from the measured acceleration at the tip mass, an integrator is used. In a practical control system, this is implemented with a low pass filter:

$$H_v(s) = \frac{g_v}{s + \omega_{LP}} \tag{17}$$

The cut-off frequency  $\omega_{LP}$  is set well below the resonance of the actuator, here at about 5 Hz, and  $g_v$  is chosen appropriately. Second, an acceleration feedback loop was tuned to the second

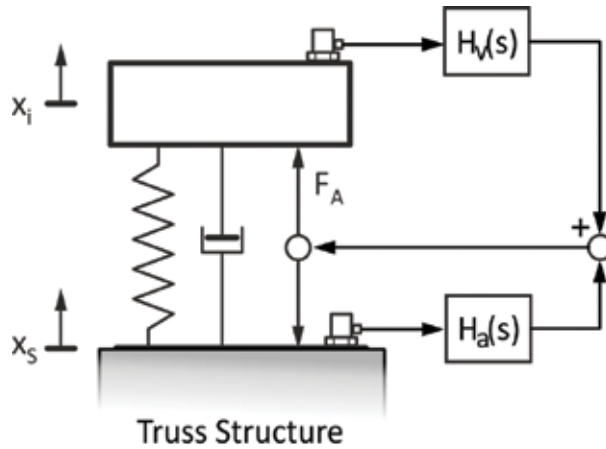


Figure 18. Block diagram of the control system.

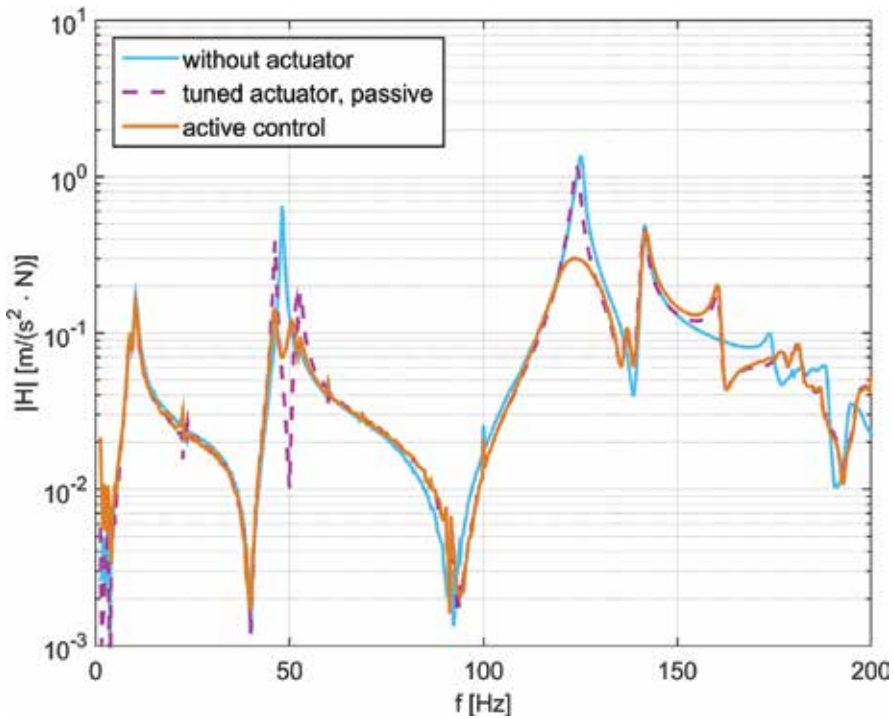


Figure 19. Control results for the truss structure.

mode of the truss at 125 Hz (**Figure 19**). The corresponding transfer function is a second order low pass filter:

$$H_a(s) = \frac{g_a \omega_c}{s^2 M + 2\theta \omega_c s + \omega_c^2} \quad (18)$$

Here,  $\omega_c$  is the tuning frequency and  $\theta$  the damping coefficient, while  $g_a$  is the control loop gain. The control system was implemented with analog circuitry.

Since the actuator is not symmetric, a bending moment is exciting at its base additional to the transverse force. This results in lowering of a higher resonance frequency from 180 to 160 Hz and a deterioration of the vibration amplitudes in this frequency region.

## 5. Conclusions

Adaptive and active vibration control systems can outperform passive systems in terms of additional mass and vibration reduction. However, the different systems cause an increase of system complexity and need for additional power supply. Thus, alternative feasible approaches should be evaluated to find the optimal solution for a given vibration problem. To enable experimental prototyping, a design for a TVA has been introduced, that can be used for passive, adaptive, and active vibration control. It has also been shown that an advantage of such an integrated system can be applied to hybrid systems that work as passive absorbers in the lower frequency range and a can excite active forces at higher frequencies.

## Author details

Dirk Mayer\* and Sven Herold

\*Address all correspondence to: [dirk.mayer@lbf.fraunhofer.de](mailto:dirk.mayer@lbf.fraunhofer.de)

Fraunhofer Institute for System Reliability and Structural Durability LBF, Darmstadt, Germany

## References

- [1] Frahm H. Device for Damping Vibrations of Bodies; United States Patent US 98958A, 1911
- [2] den Hartog JP. Mechanical Vibrations. New York: Dover Publications, Inc., 1985
- [3] Debnath N, Deb S, Dutta A. Multi-modal vibration control of truss bridges with tuned mass dampers under general loading. *Journal of Vibration and Control*. 2016;22(20):1-20. DOI: 10.1177/1077546315571172

- [4] Kegerise M, Cattafesta L, Ha C-S. Adaptive identification and control of flow-induced cavity oscillations. In: 1st Flow Control Conference; 24–26 June 2002. DOI: 10.2514/6.2002-3158
- [5] Chung J. Vibration absorber for reduction of the in-plane vibration in an optical disk drive. *IEEE Transactions on Consumer Electronics*. 2004;**50**:552-557. DOI: 10.1109/TCE.2004.1309422
- [6] McGoldrick RT. *Ship Vibration: Report*. Vol. 1451. Washington, DC: David Taylor Model Basin—Department of the Navy; 1960
- [7] Gardonio P, Brennan MJ. On the origins and development of mobility and impedance methods in structural dynamics. *Journal of Sound and Vibration*. 2002;**249**:557-573. DOI: 10.1006/jsvi.2001.3879
- [8] Kidner M, Brennan MJ. Improving the performance of a vibration neutraliser by actively removing damping. *Journal of Sound and Vibration*. 1999:587-606
- [9] Soto MG, Adeli H. Optimum tuning parameters of tuned mass dampers for vibration control of irregular highrise building structures. *Journal of Civil Engineering and Management*. 2014;**20**:609-620. DOI: 10.3846/13923730.2014.967287
- [10] Mayer D, Herold S, Kauba M, Koch T. Approaches for distributed active and passive vibration compensation. In: Proceedings of ISMA 24, 20.-22.09.2010, Leuven, Belgium, pp. 581-593
- [11] Brennan MJ. Some recent developments in adaptive tuned vibration absorbers/neutralisers. *Shock and Vibration*. 2006;**13**:531-543. DOI: 10.1155/2006/563934
- [12] Bonello P. Adaptive tuned vibration absorbers: Design principles, concepts and physical implementation. In: Beltran-Carbajal F, editor. *Vibration Analysis and Control—New Trends and Developments*. Rijeka, Croatia: InTech; 2011
- [13] Wright RI, Kidner MRF. Vibration absorbers: A review of applications in interior noise control of propeller aircraft. *Journal of Vibration and Control*. 2004;**10**:1221-1237. DOI: 10.1177/1077546304041368
- [14] Kela L, Vähäoja P. Recent studies of adaptive tuned vibration absorbers/neutralizers. *Applied Mechanics Reviews*. 2009;**62**:60801. DOI: 10.1115/1.3183639
- [15] Mayer D, Pfeiffer T, Vrbata J, Melz T. Adaptive-passive vibration control systems for industrial applications. *SPIE Smart Structures and Materials + Nondestructive Evaluation and Health Monitoring*; 8 March 2015. SPIE; 2015. p. 94330E. DOI: 10.1117/12.2086359
- [16] Howard CQ. Recent developments in submarine vibration isolation and noise control. In: Proceedings of the 1st Submarine Science Technology and Engineering Conference; 2011
- [17] Hassan A, Torres-Perez A, Kaczmarczyk S, Picton P. Vibration control of a Stirling engine with an electromagnetic active tuned mass damper. *Control Engineering Practice*. 2016;**51**:108-120. DOI: 10.1016/j.conengprac.2016.03.014



- [18] Davis CL, Lesieutre GA. An actively tuned solid-state vibration absorber using capacitive shunting of piezoelectric stiffness. *Journal of Sound and Vibration*. 2000;**232**:601-617. DOI: 10.1006/jsvi.1999.2755
- [19] Heuss O, Salloum R, Mayer D, Melz T. Tuning of a vibration absorber with shunted piezoelectric transducers. *Archive of Applied Mechanics*. 2016;**86**:1715-1732. DOI: 10.1007/s00419-014-0972-5
- [20] Winberg M, Johansson S, Claesson I. Inertial mass actuators—Understanding and tuning. In: *Proceedings ICSV 11; St. Petersburg; 2004*
- [21] Belgacem W, Berry A, Masson P. Active vibration control on a quarter-car for cancellation of road noise disturbance. *Journal of Sound and Vibration*. 2012;**331**:3240-3254. DOI: 10.1016/j.jsv.2012.02.030
- [22] Persson P, Lagö TL, Norberg A. Active control of sleeper-induced sound in a high speed train (Conference Paper by Per Persson, Thomas L Lagö, Arvid Norberg)—*Electronic Research Archive @ Blekinge Institute of Technology (BTH); 1999*
- [23] Díaz IM, Reynolds P. Robust saturated control of human-induced floor vibrations via a proof-mass actuator. *Smart Materials and Structures*. 2009;**18**:125024. DOI: 10.1088/0964-1726/18/12/125024
- [24] Rahman M, Ong ZC, Chong WT, Julai S, Khoo SY. Performance enhancement of wind turbine systems with vibration control: A review. *Renewable and Sustainable Energy Reviews*. 2015;**51**:43-54. DOI: 10.1016/j.rser.2015.05.078
- [25] Konstanzer P, Grünewald M, Jänker P, Storm S. Piezo tuneable vibration absorber system for aircraft interior noise reduction. In: *Proceedings of Euronoise 2006; 30 May–01 June 2006; Tampere, Finland. 2006*
- [26] Beltrán-Carbajal F, Silva-Navarro G. Active vibration control in Duffing mechanical systems using dynamic vibration absorbers. *Journal of Sound and Vibration*. 2014;**333**:3019-3030
- [27] Preumont A. *Vibration Control of Active Structures: An Introduction*. 3rd ed. Berlin, Heidelberg, New York, Hong Kong, London, Milan, Paris, Tokyo: Springer; 2011
- [28] Kuo SM, Lee BH. *Real-Time Digital Signal Processing*. New York, Chichester: Wiley; 2001
- [29] Herold S, Mayer D, Melz T, Röglin T. Design and test of a piezoelectric inertial mass actuator for active vibration control. In: Sinha J, editor. *Vibration Engineering and Technology of Machinery*. 23rd ed. United Kingdom: Springer International Publishing; 2014. pp. 587-597
- [30] Herold S, Mayer D. Adaptive piezoelectric absorber for active vibration control. *Actuators*. 2016;**5**:7. DOI: 10.3390/act5010007



---

# Design of Robust Digital Pole Placer for Car Active Suspension with Input Constraint

---

Hisham M. Soliman, Rashid Al-Abri and  
Mohammed Albadi

Additional information is available at the end of the chapter

<http://dx.doi.org/10.5772/intechopen.70587>

---

## Abstract

This chapter deals with the problem of state feedback control for an active quarter-car suspension system with control input constraint. The dynamics of the suspension system is first formed in terms of the control objectives: ride comfort, suspension deflection, and maximum actuator control force. The control task is formulated as robustly placing the closed poles in a desired region against different passenger load. Since digital computers are widely used in the vehicle industry, a new saturated controller design method is presented for regional pole-placement of uncertain discrete time systems. The constraint of control input saturation is considered in the design phase. The desired dynamic performance for uncertain discrete-time systems is represented by the settling time and damping ratio. A sufficient condition is derived to place the poles in a desired region. The design is formulated in terms of linear matrix inequality optimization. The effectiveness of the proposed design is illustrated by applying it to a quarter-car active suspension system. Different road tests for the proposed controller are carried out: step and bump disturbances. The proposed design achieves the desired oscillation damping due to road disturbances in addition to passenger comfort. The results are compared with the passive suspension system.

**Keywords:** constrained control, regional pole placement, linear matrix inequality (LMI) optimization, discrete-time systems, vehicle active suspension

---

## 1. Introduction

The design of a car suspension system is of paramount importance for improving the ride comfort, maintaining vehicle maneuverability, and retaining the safety of passengers [1]. Vehicle suspension systems include wishbone, spring, and shock absorber (e.g., damper) to transmit and mitigate forces between the car body and the road. This contributes to the passenger

---

comfort and the ride. However, the widely used passive suspension systems which use springs and dampers with fixed parameters (stiffness and damper coefficients) do not achieve satisfactory suspension performance under wider driving maneuvers. This problem is alleviated by the recent developments of semi-active suspension and active suspension [2].

Semi-active suspensions use the springs and dampers whose parameters (e.g., stiffness and damper coefficients) are adjusted corresponding to different vehicle driving scenarios [3]. These varying parameters provide considerable improvements over passive suspension systems. However, special springs and/or dampers (e.g., a magneto rheological fluid, MR, damper) are used in this case, and the construction and tuning of such components are not easy. Moreover, using such elements can lead to potential difficulties, for example, MR dampers exhibit hysteresis dynamics, which are highly nonlinear and difficult to model.

Active suspension has attracted extensive research because in this framework an extra actuator is placed between the car body and the wheel-axle. It is installed in parallel to other suspension mechanisms (e.g., damper and spring [4]). So, this actuator can be controlled to dissipate energy from the road disturbances and thus reduces the impact on the displacement of vehicles. It is well known that active suspension requires high energy demand and cost. Therefore, active suspensions have not been widely used in commercial vehicles. However, it is expected that active suspension techniques will be adopted by the industry due to its potentials to improve the suspension performance.

Extensive research work on active suspension has been carried out in the past few decades [5, 6]. A crucial issue in the active suspension system designs is the control strategies, which should make the actuators pull down or push up the suspension motions and also achieve other suspension requirements. A model-reaching adaptive control is presented in [7] to achieve the ideal isolation of a skyhook target; the vehicle maintains a stable posture. An LPV gain-scheduling controller is proposed in [8] for a quarter-vehicle active suspension system. To manage the trade-off between the conflicting performances, the  $H^\infty$  control method can manage the trade-off and obtain a compromise performance [9, 10]. An  $H^\infty$  control is designed for active suspension systems that are subject to actuator time delay which is given in [11]. Sampled-data  $H^\infty$  control of uncertain active suspension systems via fuzzy control is presented in [12]. Adaptive sliding-mode control for active suspensions using fuzzy approach is shown in [13]. In [14], a linear-quadratic-Gaussian (LQG) control is used to obtain a trade-off between the conflicting suspension requirements.

Many physical systems are inherently nonlinear and subject to variation in the operating point. To overcome such difficulties, the system to be controlled is represented by an uncertain linear time-invariant model. The uncertainty can be cast into either polytopic or norm-bounded form. The powerful, robust control techniques of linear systems can then be applied [15]. The poles of systems without uncertainty can be placed in desired locations so as to achieve good dynamic behavior in terms of settling time and damping ratio [16]. However, for systems with uncertainties, the closed-loop poles can be assigned to a domain (D) or region, rather than specific locations [17]. This is termed D-stability or regional pole placement by using robust controllers against system uncertainty. Regional pole placement for continuous-time systems with polytopic uncertainty using state feedback is presented in [18], while output feedback is

presented in [19]. Regional pole placement with guaranteed-cost control of active suspension system of a quarter-car model is given in [20].

In many practical control problems, the actuator has limited output, called saturated (or constrained) control [21]. Combining robust pole placement with saturated control is termed multi-objective control. When the actuator saturation is not considered in the design phase, the performance of the designed control system seriously deteriorates. A state-feedback control achieving guaranteed-cost regional pole placement with the control limits, i.e., the actuator force must not exceed a certain limit, is presented in [22] for continuous-time case.

This chapter is concerned with the digital state-feedback controller design problem for active quarter-car suspension systems. The main contributions of this chapter can be summarized as follows: (1) formulate multi-object control constraints in LMIs via state-feedback control approach for the suspension vehicle system and (2) construct a simple new-type state-feedback controller. The proposed design achieves four constraints: (1) damps effectively the car oscillations due to disturbance of road irregularities, (2) robustness against different car loads, (3) no control limits violation, and (4) optimal passenger comfort against road roughness. It is expected that the proposed research pave the way for implementing the theoretical findings into vehicle suspension systems.

**Notations:** Capital and small letters denote matrices and vectors, respectively.  $I$  and  $0$  denote the identity matrix and zero matrix, respectively.  $W'$  and  $W^{-1}$  denote the transpose and the inverse of any square matrix  $W$ , respectively.  $W > 0$  ( $W < 0$ ) denotes a symmetric positive (negative)-definite matrix  $W$ . The symbol  $\bullet$  is as an ellipsis for terms in matrix expressions that are induced by symmetry. For example,

$$\begin{bmatrix} L + (W + N + W' + N') & N \\ N' & M \end{bmatrix} = \begin{bmatrix} L + (W + N + \bullet) & N \\ \bullet & M \end{bmatrix} \quad (1)$$

**Facts:** the following facts [15] are used in the sequel:

Fact 1 (congruence transformation):

The definiteness of a matrix  $W$  does not change under the congruence transformation  $H'WH$ .

Fact 2:

For any real matrices  $W_1, W_2$  and  $\Delta_k$  with appropriate dimensions and  $\Delta_k' \Delta_k \leq I, \leftrightarrow \|\Delta_k\| \leq 1$ , it follows that

$$W_1 \Delta_k W_2 + \dots W_2' \Delta_k' W_1 \leq \varepsilon^{-1} W_1 W_1' + \varepsilon W_2' W_2, \dots \varepsilon > 0 \quad (2)$$

where  $\Delta_k$  represents system uncertainty at discrete time  $k$ . The use of this lemma is to eliminate the uncertainty.

Fact 3 (Schur complement):

This fact is useful in transforming a nonlinear matrix inequality into a linear one.

For constant matrices  $W_1, W_2,$  and  $W_3,$  where  $W_1' = W_1$  and  $0 < W_2 = W_2',$  it follows that

$$W_1 + W_3'W_2^{-1}W_3 < 0 \leftrightarrow \begin{bmatrix} W_1 & W_3' \\ W_3 & -W_2 \end{bmatrix} < 0 \tag{3}$$

## 2. Problem formulation

The quarter-vehicle suspension model is shown in **Figure 1** [9].

The dynamics of the quarter-car model can be described by the state equation as follows [9]:

$$\dot{x} = Ax + Bu + D_w w, x(0) = x_0 \tag{4}$$

where

$$A = \begin{bmatrix} 0 & 1 & 0 & -1 \\ \frac{-k_s}{M_s} & \frac{-c_s}{M_s} & 0 & \frac{c_s}{M_s} \\ 0 & 0 & 0 & 1 \\ \frac{k_s}{m} & \frac{c_s}{m} & \frac{-k_t}{m} & \frac{-c_s}{m} \end{bmatrix}, D_w = \begin{bmatrix} 0 \\ 0 \\ -1 \\ 0 \end{bmatrix}, B = \begin{bmatrix} 0 \\ \frac{u_s}{M_s} \\ 0 \\ \frac{-u_s}{m} \end{bmatrix} \tag{5}$$

where  $k_s$  and  $c_s$  are the parameters of the so-called passive suspension;  $k_t$  stands for the tire stiffness; and  $M_s$  and  $m$  represent sprung (body) and unsprung (tire) masses, respectively. Moreover,  $x_s - x_u$  is the suspension stroke,  $x_u - x_0$  is the tire deflection, and  $x_0$  is the vertical ground displacement caused by road unevenness. The state variables of the model (4) are defined as  $x_1 = x_s - x_u, x_2 = \dot{x}_s, x_3 = x_u - x_0,$  and  $x_4 = \dot{x}_u.$  The disturbance due to the road roughness is  $\omega = \dot{x}_0.$  The normalized active force,  $u = u_f u_s,$  is the control input, and  $u_f$  is the active force generated by a hydraulic actuator.

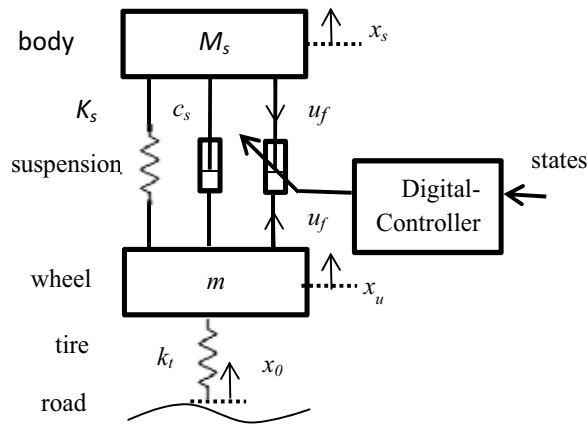


**Figure 1.** Quarter-car model with an active suspension.

The suspension performance, such as ride comfort, suspension deflection, and road holding, are considered as the control design objectives. Since the ride comfort can be quantified by the body acceleration in the vertical direction, it is reasonable to choose body acceleration as the regulated output,  $z(t)$ . The less the vertical body acceleration, the more comfort ride results [9]. One of the main objectives of the proposed controller is to minimize the vertical acceleration  $z(t)$  to improve vehicle ride comfort. The body acceleration is given by [9]

$$z = Cx + B_1u \tag{6}$$

where

$$C = \frac{1}{M_s}[-k_s \quad -c_s \quad 0 \quad c_s], B_1 = \frac{u_s}{M_s} \tag{7}$$

In addition, due to the mechanical structure, the suspension stroke should not exceed the allowable maximum. Or equivalently, the active control force provided for the active suspension system should be confined to a certain range. Due to actuator saturation, it is in addition assumed that the normalized active force is bounded as  $|u(t)| \leq 1$ , **Figure 2**. Therefore, the bound on the control input is  $u_{max} = 1$ , and the active force is bounded by  $u_s$ .

Since microprocessors are widely used in car industries, system (4) can be discretized to design a discrete-time controller. Considering the disturbance effect later, the resulting discrete-time uncertain system with saturated control input is

$$x_{k+1} = (A + \Delta A_k)x_k + (B + \Delta B_k).sat(u_k) \tag{8}$$

where  $x_k$  and  $u_k$  are the state and control vectors of dimension  $n$  and  $m$ , respectively. The pair  $(A,B)$  is assumed to be controllable. The matrices  $\Delta A_k$  and  $\Delta B_k$  are time varying which represents parametric uncertainty due to changes in passenger load and/or nonlinearities. The uncertainty is assumed to be of the norm-bounded form:

$$[\Delta A_k, \Delta B_k] = M\Delta_k[N, N_b] \tag{9}$$

$$\Delta_k' \Delta_k \leq I \leftrightarrow \|\Delta_k\| \leq 1 \tag{10}$$

where  $M$  and  $N$  are known constant matrices with appropriate dimensions.  $\Delta_k$  is an unknown matrix with Lebesgue measurable elements.

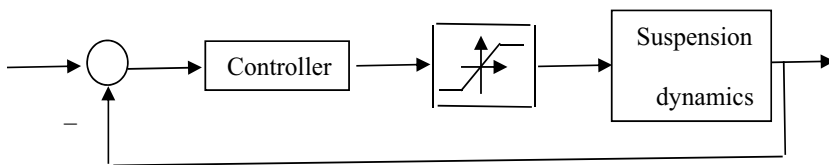


**Figure 2.** Feedback-saturated control systems.

The control signal is constrained due to practical limitation. The saturated controller to develop is assumed to be state feedback and symmetric and normalized as follows:

$$u = Fx, \quad -1 < u_j < +1, \quad j = 1 \dots m$$

or

$$sat(u_j) = \begin{cases} 1 & \text{if } u_j \geq 1 \\ u_j & \text{if } -1 < u_j < 1 \\ -1 & \text{if } u_j \leq -1 \end{cases} \quad (11)$$

$$u_k = Fx_k \quad (12)$$

The closed-loop system is given by

$$x_{k+1} = \{A + \Delta A_k + (B + \Delta B_k)F\}x_k \quad (13)$$

The problem is to develop a saturated discrete-time controller, which robustly stabilizes the closed-loop system (13) and ensures a good dynamic performance, described by maximum settling time and minimum damping ratio despite the system uncertainty. To achieve both constraints of max settling time and min damping ratio, the closed-loop poles must lie in the hatched area, as shown in **Figure 3**. This is termed D-stability in which the poles must lie inside

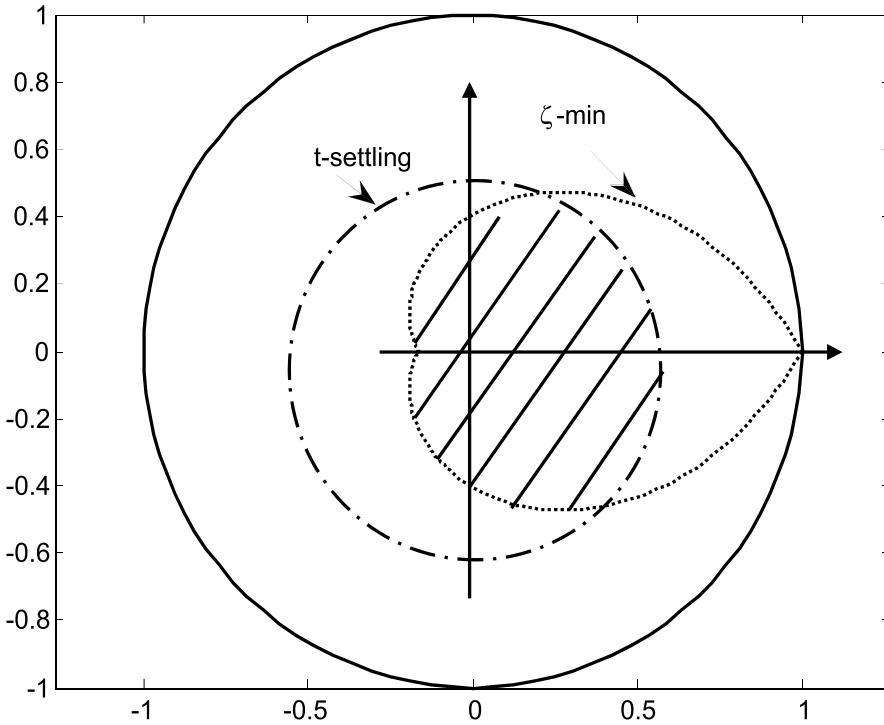


**Figure 3.** Desired region of closed-loop poles, hatched.



the region  $D$  for all admissible uncertainties. The proposed controller must achieve  $D$ -stability in addition to the constraint of maximum actuator control force.

### 3. Digital saturated regional pole placer

To design the abovementioned controller, the nonlinear saturated control function is first linearized and approximated by a convex hull. For this, the following two lemmas are used [21]:

#### Lemma-1

For all  $u \in \mathbb{R}^m$  and  $\theta \in \mathbb{R}^m$  such that  $|\theta_j| < 1, j \in [1, m]$ ,

$$\text{sat}(u) \in \text{co}\{D_i u + D_i^- \theta, i \in [1, \eta]\}, \quad (14)$$

with  $\text{co}$  denoting the convex hull.

Eq. (14) has the following equivalent form:

$$\text{sat}(u) = \sum_{i=1}^{\eta} \gamma_i [D_i u + D_i^- \theta], \gamma_i \geq 0 \quad (15)$$

Here,  $D_i$  is an  $m \times m$  diagonal matrix with elements either 1 or 0 and  $D_i^- = (I - D_i)$ , which results in  $\eta = 2^m$  possible matrices. The matrices  $D_i$  and  $D_i^-$  are introduced to model the saturation function as a linear one. If  $D_i$  is selected as  $I$ ,  $D_i^-$  becomes 0, and the resulting controller will be unsaturated. Recall that these controllers (14) work in a linear region and do not allow saturation to occur.

The following sets are defined:

$$D(F) = \{x \in \mathbb{R}^n : -1 \leq Fx \leq 1\} \text{ and } \varepsilon(P, \rho) = \{x \in \mathbb{R}^n : x^T P x \leq \rho; \rho > 0\} \quad (16)$$

where  $P$  is a symmetric positive-definite matrix. The sets  $D(F)$  and  $\varepsilon(P, \rho)$  represent, respectively, a symmetrical polyhedral and an ellipsoidal one. The following result is recalled:

#### Lemma-2

For a given positive scalar  $\rho$ , if there exist matrices  $Y \in \mathbb{R}^{m \times n}$  and  $Z \in \mathbb{R}^{m \times n}$  and a positive-definite matrix  $X = X' \in \mathbb{R}^{n \times n}$  and solutions to the following LMIs:

$$[AX + B(D_i Y + D_i^- Z)] + \bullet < 0, \quad (17)$$

$$\begin{bmatrix} 1/\rho & Z_j \\ \bullet & X \end{bmatrix} > 0 \quad (18)$$

$$i = 1, \dots, \eta; j = 1, \dots, m, \quad (19)$$

then when  $\Delta A = 0$  and  $\Delta B = 0$ , the closed-loop saturated control system is asymptotically stable at the origin  $\forall x_0 \in \varepsilon(P, \rho)$  with

$$F = YX^{-1} \tag{20}$$

$$P = X^{-1} \tag{21}$$

It is worth mentioning that LMI (17) guarantees asymptotic stability, while LMI (17) ensures that the ellipsoidal set  $\varepsilon(P, \rho)$  is contained inside the polyhedral set  $D(H)$ , allowing the control to be saturated. As a special case, by selecting  $D_i = I$ , the control works only in a linear region without reaching saturation. In this case,  $D_i^- = 0$  in LMI (18), and  $Z_i$  is replaced by  $Y_i$  in LMI (17) to have  $\varepsilon(P, \rho) \subset D(F)$ .

Our control target is to design a saturated controller that maintains asymptotic stability against system uncertainty, as well as to place the closed-loop poles in a desired region D-stability, if possible, so as to achieve a good dynamic response in terms of settling time  $t_s$  and damping ratio  $\zeta$ .

Pole placement in the region shown in **Figure 3** is difficult to solve. However, the problem can be easily solved by approximating the spiral of the constant damping ratio as a circle, as shown in **Figure 4**. The problem is thus reduced to placing the poles in between the two circles, one for  $t_s$  and the other for  $\zeta_{approx}$ .

We will consider two design cases: without and with saturated inputs.

**Design case 1: unsaturated control**

Consider the uncertain system with unsaturated control

$$x_{k+1} = (A + \Delta A)x_k + (B + \Delta B).u_k \tag{22}$$

**Theorem 1**

If there is a feasible solution to the following LMIs, then the closed-loop poles lie inside the two circles of center  $q_1$  and radius  $r_1$  and center  $q_2$  and radius  $r_2$ :

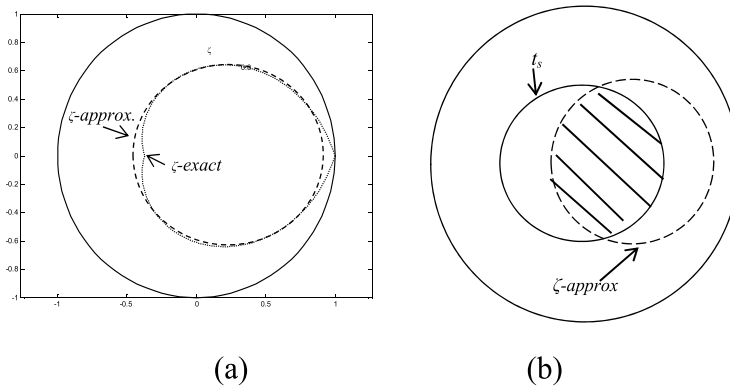


**Figure 4.** (a)  $\zeta$  circle approximation and (b) desired region of the poles, hatched.

$$X = X' > 0, \varepsilon_1 > 0, \varepsilon_2 > 0, v_1 > 0, v_2 > 0,$$

$$\begin{bmatrix} -r_1^2 X & \bullet & \bullet & \bullet \\ AX + BY + q_1 X & -X + (\varepsilon_1 + v_1)MM' & \bullet & \bullet \\ NX & 0 & -\varepsilon_1 I & \bullet \\ N_b X & 0 & 0 & -v_1 I \end{bmatrix} < 0 \quad (23)$$

$$\begin{bmatrix} -r_2^2 X & \bullet & \bullet & \bullet \\ AX + BY + q_2 X & -X + (\varepsilon_2 + v_2)MM' & \bullet & \bullet \\ NX & 0 & -\varepsilon_2 I & \bullet \\ N_b X & 0 & 0 & -v_2 I \end{bmatrix} < 0 \quad (24)$$

Moreover, the controller is given by

$$F = YX^{-1} \quad (25)$$

*Proof*

It is well known [17] that the eigenvalues of matrix  $A$  lie inside a circle of center  $-q$  and radius  $r$  if and only if

$$P = P' > 0, \begin{bmatrix} -r^2 P & \bullet \\ A + qI & -P^{-1} \end{bmatrix} < 0 \quad (26)$$

or equivalently,

$$P = P' > 0,$$

$$\begin{bmatrix} -r^2 P & \bullet \\ A + BF + qI & -P^{-1} \end{bmatrix} + \left( \begin{bmatrix} 0 \\ M \end{bmatrix} \Delta(t) \begin{bmatrix} N' \\ 0 \end{bmatrix}' + \bullet \right) + \left( \begin{bmatrix} 0 \\ M \end{bmatrix} \Delta(t) \begin{bmatrix} F' N_b' \\ 0 \end{bmatrix}' + \bullet \right) < 0 \quad (27)$$

The last matrix inequality is satisfied if

$$P = P' > 0,$$

$$\begin{bmatrix} -r^2 P & \bullet \\ A + BF + qI & -P^{-1} \end{bmatrix} + \left( \varepsilon \begin{bmatrix} 0 \\ M \end{bmatrix} \begin{bmatrix} 0 \\ M \end{bmatrix}' + \varepsilon^{-1} \begin{bmatrix} N' \\ 0 \end{bmatrix} \begin{bmatrix} N' \\ 0 \end{bmatrix}' \right) \\ + \left( v \begin{bmatrix} 0 \\ M \end{bmatrix} \begin{bmatrix} 0 \\ M \end{bmatrix}' + v^{-1} \begin{bmatrix} F' N_b' \\ 0 \end{bmatrix} \begin{bmatrix} F' N_b' \\ 0 \end{bmatrix}' \right) < 0$$

is satisfied or

$$\begin{bmatrix} -r^2 P & \bullet & \bullet & \bullet \\ A + BF + qI & -P^{-1} + (\varepsilon + v)MM' & \bullet & \bullet \\ N & 0 & -\varepsilon I & \bullet \\ N_b F & 0 & 0 & -vI \end{bmatrix} < 0 \quad (28)$$

The last matrix inequality can be linearized by pre- and postmultiplying by  $[P^{-1}, I, I, I]$ , that is, applying fact 1 and substituting  $P^{-1} = X, FX = Y$ .

Note that the above condition is only a sufficient condition for regional pole placement in one circle. Since we have to achieve pole placement in the area between the two circles, one for  $t_s$  and the other for  $\zeta$ , we have theorem 1.

### Design case 2: saturated control

Consider the uncertain system with saturated control

$$x_{k+1} = (A + \Delta A)x_k + (B + \Delta B).sat(u_k) \quad (29)$$

### Theorem 2

The regional pole placement with robust saturated state-feedback control (12) for the uncertain system (8) can be achieved if there exist  $X=X' > 0, \varepsilon_1 > 0, \varepsilon_2 > 0, \nu_1 > 0, \nu_2 > 0, Y$  and a feasible solution to the following LMIs:

$$\begin{bmatrix} -r_1^2 X & \bullet & \bullet & \bullet \\ AX + B(D_i Y + \bar{D}_i Z) + q_1 X & -X + (\varepsilon_1 + \nu_1)MM' & \bullet & \bullet \\ NX & 0 & -\varepsilon_1 I & \bullet \\ N_b(D_i Y + \bar{D}_i HX) & 0 & 0 & -\nu_1 I \end{bmatrix} < 0 \quad (30)$$

$$\begin{bmatrix} -r_2^2 X & \bullet & \bullet & \bullet \\ AX + B(D_i Y + \bar{D}_i Z) + q_2 X & -X + (\varepsilon_2 + \nu_2)MM' & \bullet & \bullet \\ NX & 0 & -\varepsilon_2 I & \bullet \\ N_b(D_i Y + \bar{D}_i HX) & 0 & 0 & -\nu_2 I \end{bmatrix} < 0 \quad (31)$$

$$\begin{bmatrix} 1/\rho & Z_j \\ \bullet & X \end{bmatrix} > 0 \quad (32)$$

for  $i = 1, \dots, \eta; j = 1, \dots, m$ .

Moreover, the saturated robust pole placer is given by

$$F = YX^{-1} \quad (33)$$

*Proof*

From (26), the poles of the closed-loop uncertain system (13) lie inside the circle of center  $(-q, 0)$  and radius  $r$  if and only if there is a feasible solution to the following LMI:

$$P = P' > 0$$

$$\begin{bmatrix} -r^2 P & \bullet \\ A + \Delta A + (B + \Delta B)(D_i F + \bar{D}_i^- H) + qI & -P^{-1} \end{bmatrix} < 0 \quad (34)$$

Eq. (34) is satisfied if the following inequality is satisfied:

$$\begin{aligned}
 &P = P' > 0 \\
 &\begin{bmatrix} -r^2P & \bullet \\ A + B(D_iF + \bar{D}_iH) + qI & -P^{-1} \end{bmatrix} + \varepsilon \begin{bmatrix} 0 \\ M \end{bmatrix} \begin{bmatrix} 0 \\ M \end{bmatrix}' + \varepsilon^{-1} \begin{bmatrix} N' \\ 0 \end{bmatrix} [N \ 0] + \\
 &v \begin{bmatrix} 0 \\ M \end{bmatrix} \begin{bmatrix} 0 \\ M \end{bmatrix}' + v^{-1} \begin{bmatrix} (D_iF + \bar{D}_iH)' N_b' \\ 0 \end{bmatrix} [N_b(D_iF + \bar{D}_iH) \ 0] < 0
 \end{aligned} \tag{35}$$

or equivalently,

$$\begin{bmatrix} -r^2P & \bullet & \bullet & \bullet \\ A + B(D_iF + \bar{D}_iH) + qI & -P^{-1} + (\varepsilon + v)MM' & \bullet & \bullet \\ N & 0 & -\varepsilon I & \bullet \\ N_b(D_iF + \bar{D}_iH) & 0 & 0 & -vI \end{bmatrix} < 0 \tag{36}$$

By post- and premultiplying (36) by  $P^{-1}$ , that is, by applying the congruence transformation and substituting  $P^{-1} = X$ , one gets (30). This completes the proof.

#### 4. Design of vehicle active suspension control

In this section, we present a design example to illustrate the effectiveness of the proposed controller design method. Unlike the previous approaches, the proposed design introduces a digital computer or a microprocessor into the control loop as given in theorem 2. It is used to design an active suspension system for the quarter-vehicle model shown in **Figure 1** [9].

Note that active forces generated by hydraulic actuators and considered as control inputs are bounded because of actuator saturation. The system parameters and nominal values are shown in **Table 1**.

The normalized input is bounded as  $|u(t)| \leq 1$ , and the active force is bounded by  $u_s =$  allowable spring stroke ( $\pm 0.08$  m) \*spring constant.

Parameter	Value
$M_s$	320 kg
$m$	40 kg
$K_s$	18 kN/m
$k_t$	200 kN/m
$c_s$	1 kN.s/m
$u_s$	1.5 KN

**Table 1.** Quarter-vehicle active suspension parameters.

Due to different passenger load variations, it is assumed that the mass  $M_s$  varies between 250 to 390 kg. The system is discretized with the zero order hold method at a sampling time  $T_s=0.001$  sec. Therefore, the discrete time norm-bounded model is obtained as

$$A = \begin{bmatrix} 0.9997 & 0.000986 & 0.002476 & -0.0009852 \\ -0.05546 & 0.9969 & -0.007783 & 0.003106 \\ 0.0002228 & 1.245e-5 & 0.9975 & 0.0009867 \\ 0.4433 & 0.02485 & -4.934 & 0.9727 \end{bmatrix} \quad (37)$$

$$B = [2.089e-5 \quad 0.004622 \quad -1.857e-5 \quad -0.03694]' \quad (38)$$

With uncertainty matrices

$$M = [-0.0004 \quad -0.1367 \quad 0 \quad -0.0016]' \quad (39)$$

$$N = [-0.0729 \quad -0.0037 \quad -0.0102 \quad 0.0041], \quad (40)$$

$$N_b = 0.0061 \quad (41)$$

For passenger comfort, the oscillations due road bumps should be damped out within 1 s with a minimum damping ratio  $\zeta = 0.25$  [20]. To achieve the first objective, we select  $r_1 = 0.9960$  and  $q_1 = 0$  for the first circle, while for the second,  $r_2 = 0.68$  and  $q_2 = -0.31$ .

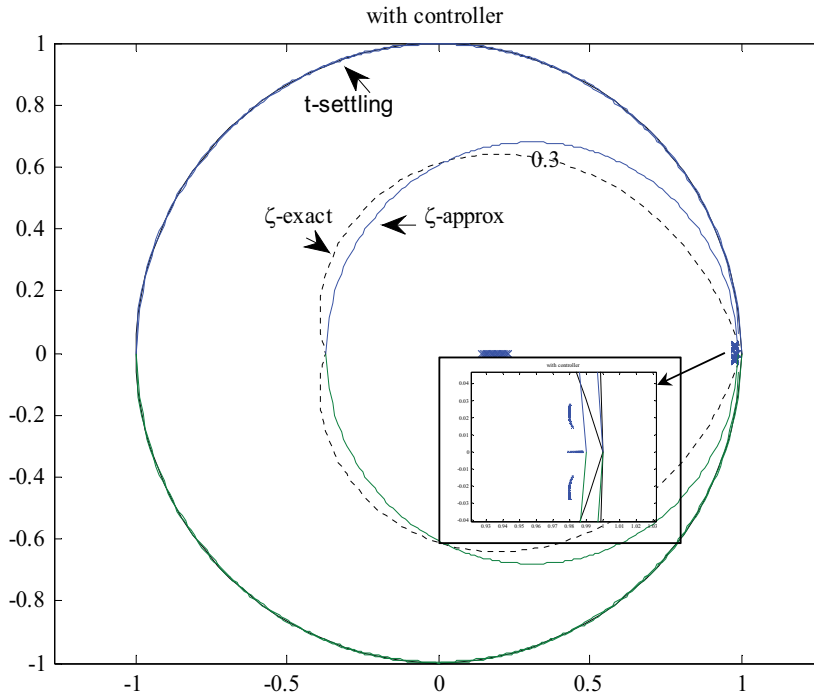


Figure 5. Closed-loop poles with system uncertainties using saturated control.

The LMIs (30) are solved to get the saturated control gain matrix as

$$F = [-402.7340, -47.9208, 546.4541, 16.1682] \quad (42)$$

As shown in **Figure 5**, all the closed-loop poles lie inside the desired domain.

In general, road disturbances can be classified as shock or vibration. For shock disturbances, the proposed controller is tested for two cases: step and bump road. The frequency response is studied when the system is subjected to resonant frequency disturbance forces for the vibration case.

### Case 1: step road test

For the simulation, we assume that the vehicle is subject to a 500 N unit step input due to a step road change. Two cases are considered: light and heavy passenger loads. With passive suspension, the vehicle will oscillate for an unacceptable long time, about 3.5 s, with large overshoot (**Figures 6 and 7**). This might damage the suspension system, whereas the active suspension damps the oscillations in about 0.3 s without overshoot (**Figures 6 and 7**).

### Case 2: road bump test

In order to study the system response due to road bump, the case of an isolated bump in an otherwise smooth road surface is considered [9]. The corresponding ground displacement in this case is given by

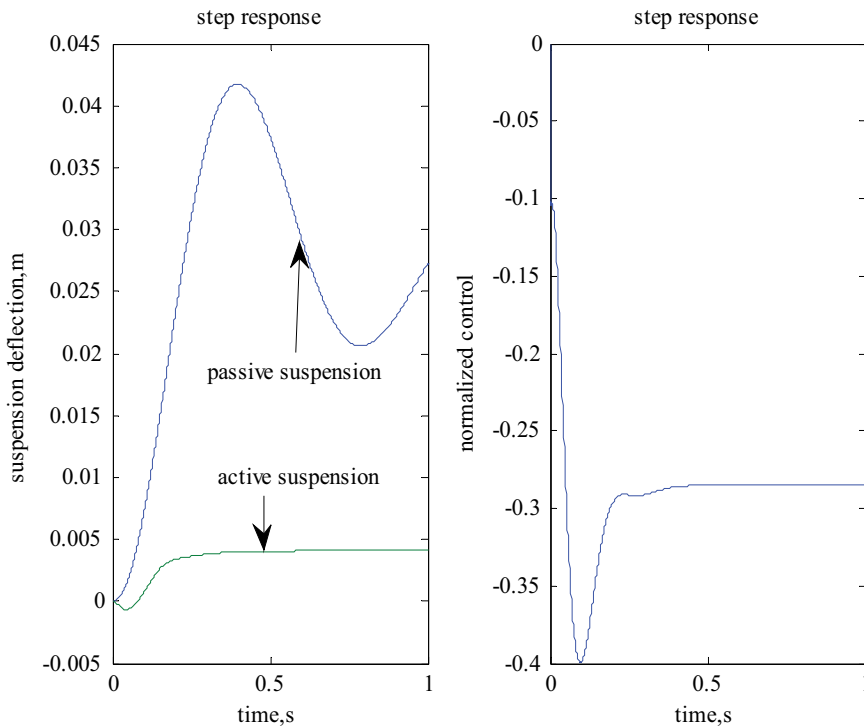


**Figure 6.** Step response at light load.

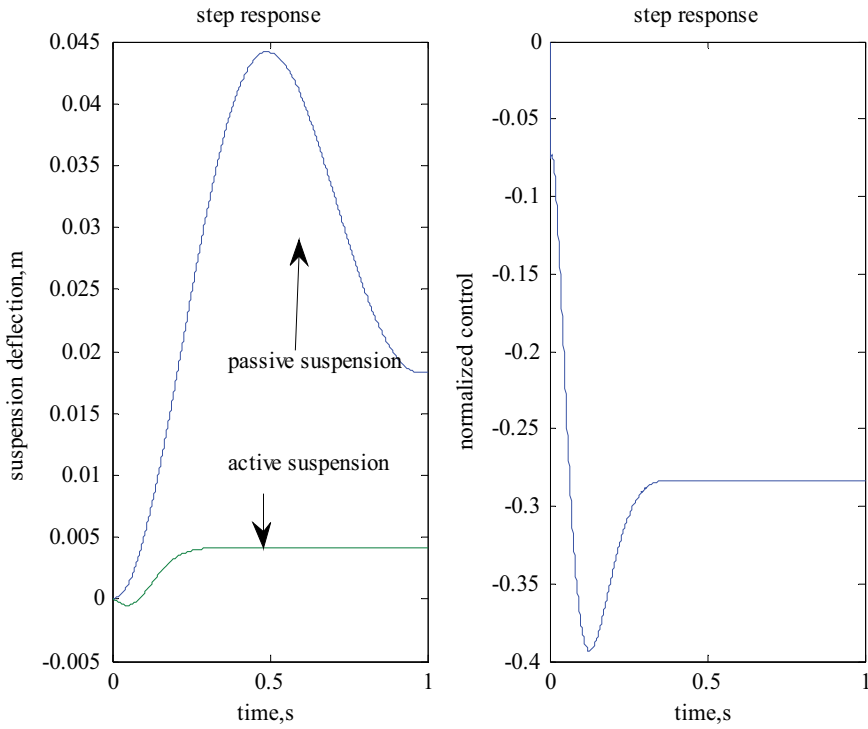


Figure 7. Step response at heavy load.

$$x_0 = \begin{cases} \frac{A}{2} \left[ 1 - \cos \left( \frac{2\pi V}{L} t \right) \right], & 0 \leq t \leq \frac{L}{V} \\ 0, & t > \frac{L}{V} \end{cases} \quad (43)$$

where  $A$  and  $L$  are the height and the length of the bump and  $V$  is the vehicle forward velocity. These values are chosen as  $A = 0.1$  m,  $L = 5$  m, and  $V = 27$  km/h. The bump response, namely, the suspension stroke (m) and the normalized control, is shown for two loads: light and heavy (Figures 8 and 9). In comparison with the passive suspension case, the proposed robust saturated control gives a better dynamic performance in terms of less overshoot and faster damping of the suspension stroke. Moreover, the normalized control signal is bounded between  $\pm 1$  as shown in Figures 8 and 9.

#### 4.1. Passenger comfort

The ride comfort is usually measured by the body acceleration as given in (6). This acceleration is shown in Figure 10.

It is evident from Figures 6–10 that the active suspension outperforms the passive one since it satisfies the control objectives (damps out the oscillations in  $<1$  s and damping ratio  $> 0.25$ ) as



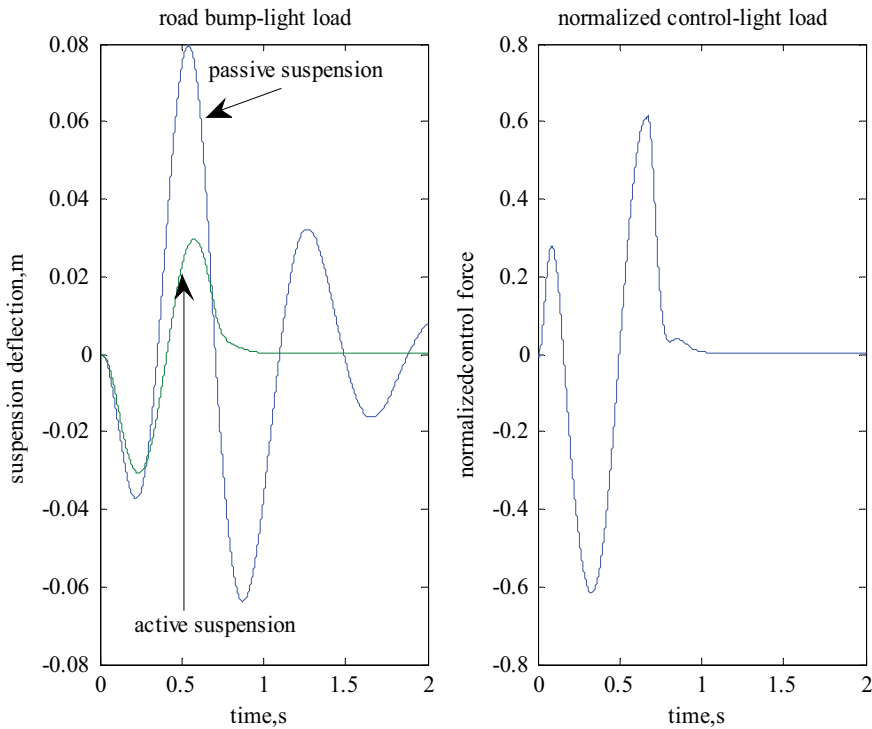


**Figure 8.** Road bump response at light load.

well as it does not violate the constraints of suspension stroke (8 cm) and hydraulic actuator force limit of 1.5 KN. Active suspension also provides better passenger comfort than the passive one as it has a lower body acceleration.

### Case 3: frequency response

It is well known that ride comfort is frequency sensitive. From the ISO2361, the human body is much sensitive to vertical vibrations in the frequency range of 4–8 Hz. Hence, further research work is needed to evaluate the designed constrained suspension in the frequency domain. In the analysis and design of linear systems, the relationship between the time domain and frequency domain characteristics plays an especially important role. However, in system design the state space in the time domain is more convenient as done in the proposed controller. In system analysis, conditions for the robust stability and robust performance are described as specifications on the frequency response in most cases. Therefore, it is indispensable to transform frequency domain conditions into equivalent time domain conditions in order to establish an effective design theory. Parseval's theorem gives the relationship between the squared integral of a time function and that of its Fourier transform, namely, the energy in the time domain is equal to the energy in the frequency domain. As a powerful tool bridging the time domain and frequency domain properties of systems, Kalman-Yakubovich-Popov (KYP) lemma plays a fundamental role in robust control.

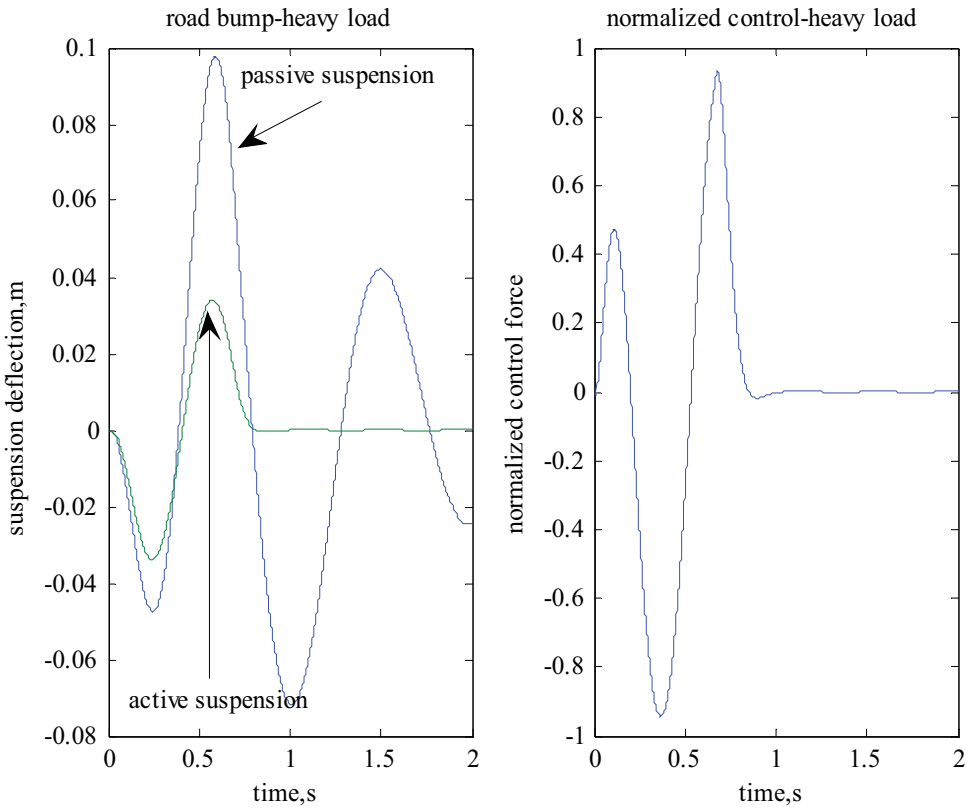


Figure 9. Road bump response at heavy load.

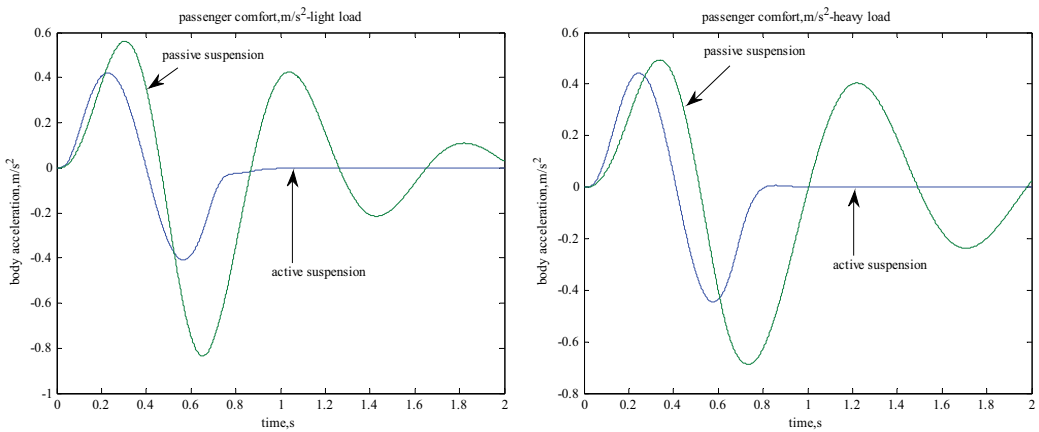


Figure 10. Passenger comfort due to road bump: light load (left) and heavy load (right).

## 5. Conclusion

This chapter considers placing the poles in a desired region of uncertain linear digital systems in the presence of input saturation. The new scheme is developed to design robust controllers, taking into consideration the effect of saturation nonlinearity. The proposed controller is based on LMI optimization and requires the uncertainty of model parameters to be cast in the norm-bounded form. The designed controller is applied to an active suspension of a quarter-vehicle model. Analysis and simulation results have confirmed the potential benefit of the proposed constrained active suspension in achieving the best possible ride comfort while keeping suspension strokes and control inputs within bounds.

In the future, it will be interesting to consider the actuator dynamic behavior in the controller design phase and also to develop robust control based on the relation between time domain and frequency domain properties.

## Author details

Hisham M. Soliman<sup>1,2\*</sup>, Rashid Al-Abri<sup>1</sup> and Mohammed Albadi<sup>1</sup>

\*Address all correspondence to: [hsoliman1@yahoo.com](mailto:hsoliman1@yahoo.com)

1 Department of Electrical and Computer Engineering, Sultan Qaboos University, Muscat, Oman

2 Electrical Engineering Department, Cairo University, Cairo, Egypt

## References

- [1] Cao D, Song X, Ahmadian M. Editors's perspectives: Road vehicle suspension design, dynamics, and control. *Vehicle System Dynamics*. 2011;**49**(1–2):3-28
- [2] Tseng HE, Hrovat D. State of the art survey: Active and semi-active suspension control. *Vehicle System Dynamics*. 2015;**53**(7):1034-1062
- [3] Fallah M, Bhat RB, Xie WF. Optimized control of semiactive suspension systems using H robust control theory and current signal estimation. *IEEE/ASME Transactions on Mechatronics*. 2012;**17**(4):767-778
- [4] Yagiz N, Hacioglu Y. Backstepping control of a vehicle with active suspensions. *Control Engineering Practice*. 2008;**16**(12):1457-1467
- [5] Soliman HM, Awadallah MA, Nadim Emira M. Robust controller design for active suspensions using particle swarm optimization. *The International Journal of Modeling, Identification and Control*. 2008;**5**:66-76

- [6] Readman MC, Corless M, Villegas C, Shorten R. Adaptive Williams filters for active vehicle suspensions. *Transactions of the Institute of Measurement and Control*. 2010;**32**(6):660-676
- [7] Zuo L, Slotine JJ, Nayfeh SA. Model reaching adaptive control for vibration isolation. *IEEE Transactions on Control Systems*. 2005;**13**(4):611-617
- [8] Onat C, Kucukdemiral T, Sivrioglu S, Cansever YG. LPV gain scheduling controller design for a non-linear quarter-vehicle active suspension system. *Transactions of the Institute of Measurement and Control*. 2009;**31**(1):71-95
- [9] Chen H, Guo K. Constrained  $H^\infty$  control of active suspensions: An LMI approach. *IEEE Transactions on Control Systems Technology*. May 2005;**13**(3):412-421
- [10] Suzuki T, Takahashi M. Robust Active Suspension Control for Vibration Reduction of Passenger's Body. Chapter 5; *Challenges and Paradigms in Applied Robust Control* Edited by Andrzej Bartoszewicz. InTech; 2011. ISBN 978-953-307-338-5 472 p
- [11] Li H, Jing X, Karimi HR. Output-feedback-based  $H^\infty$  control for vehicle suspension systems with control delay. *IEEE Transactions on Industrial Electronics*. 2014;**61**(1):436-446
- [12] Li H, Jing X, Lam HK, Shi P. Fuzzy sampled-data control for uncertain vehicle suspension systems. *IEEE Transactions on Cybernetics*. 2014;**44**(7):1111-1126
- [13] Li H, Yu J, Hilton C, Liu H. Adaptive sliding-mode control for nonlinear active suspension vehicle systems using T-S fuzzy approach. *IEEE Transactions on Industrial Electronics*. August 2013;**60**(8)
- [14] Akbari A, Lohmann B. Output feedback HN/GH2 preview control of active vehicle suspensions: A comparison study of LQG preview. *Vehicle System Dynamics*. 2010;**48**(12):1475-1494
- [15] Mahmoud MS. *Decentralized Systems with Design Constraints*. London: Springer; 2011
- [16] Dorf R, Bishop RH. *Modern Control Systems*. 11th ed. New Jersey: Prentice Hall; 2008
- [17] Haddad WM, Bernstein DS. Controller design with regional pole constraints. *IEEE Transactions on Automatic Control*. 1992;**37**(1):54-69
- [18] Rao PS, Sen I. Robust pole placement stabilizer design using linear matrix inequalities. *IEEE Transactions on Power Systems*. Feb 2000;**15**:313-319
- [19] Mahmoud MS, Soliman HM. Design of robust power system stabilizer based on particle swarm optimization. *Circuits and Systems*. 2012;**3**:82-89
- [20] Soliman HM, Bajabaa N. Robust guaranteed-cost control with regional pole placement of active suspensions. *Journal of Vibration and Control*. June 2013;**19**(8):1170-1186
- [21] Benzaouia A. *Saturated Switching Systems*. Springer; 2012
- [22] Soliman HM, Benzaouia A, Yousef H. Saturated robust control with regional pole placement and application to car active suspension. *Journal of Vibration and Control*. 2016;**22**(1):258-269

---

# Bifurcation Makes a Wave Resonant Solid-State Gyro Be Stable

---

Svetlana Pavlovna Nikitenkova and  
Dmitry Anatolyevich Kovriguine

Additional information is available at the end of the chapter

<http://dx.doi.org/10.5772/intechopen.71726>

---

## Abstract

A golf ball having special dimples flies better than an analogous smoothed one. A surprise is that there is a range of Reynolds numbers for which the turbulent drag is somewhat less than that in the laminar case. Analogies always meet together and are accomplished themselves in the physics. We have traced an effect similar to the above mentioned in the area of solid mechanics when the nonlinear system passes through a sequence of bifurcations. In mechanical engineering, the role of such a system can play a solid-state wave gyro entering the family of MEMS/NEMS. It is known that a circular Foucault pendulum can serve as an angular sensor. Standing waves in a thin-walled elastic axisymmetric resonator of a solid-state wave gyro, mounted on a rotating platform, can also detect a rotation rate. Because there are no typical mechanical parts there, such wave sensors have advantages for long-term space missions. However, to maintain the functionality and sensitivity of a wave gyro in practice, the driving of standing waves requires a sophisticated feedback control. Nonetheless, we have demonstrated that such a gyro can operate without any feedback at the expense of the natural non-linearity of the resonator in a postbifurcation regime.

**Keywords:** wave solid-state gyro, Foucault pendulum, spring pendulum, bifurcation, stability

---

## 1. Introduction

It is well known that the aerodynamic drag is proportional, first of all, to the kinetic energy of a flow. Moreover, the drag depends on a lot of other almost uncontrolled factors such as the shape, size, inclination of the object in the flow, etc. Implicitly, all these are accumulated all together in the following formula for the hydrodynamic resistance:  $c_d \rho F V^2 / 2$ , where  $\rho$  is the density of a fluid or gas,  $V$  is the velocity of a flow,  $F$  denotes an effective area of the object,  $c_d$

---

stands for the so-called drag coefficient being a dimensionless characteristic function versus the Reynolds number. Recall that the Reynolds number is usually defined as  $VI/\nu$ , where  $l$  is an effective length,  $\nu$  is the kinematic viscosity coefficient. The function  $c_d$  is respective for all the uncontrolled points accompanying the interaction between the body and the flow. This function can be recorded experimentally using a wind tube. Experimental results obtained are used to evaluate the drag on other similar objects. In particular, the similarity by the Reynolds number ensures a correct description of viscous motions. Notice that the drag coefficient is nearly a constant in a wide range of Reynolds numbers in most practical cases. As long as the flow velocity would increase, the Reynolds number also increases. It is well known that in a slow flow, the viscosity can be neglected in practice. In this case, one can observe almost an ideal flow with no boundary layer near the surface. Therefore, there is almost no resistance to the motion in accordance with well-known d'Alembert paradox. As the velocity increases further, the drag becomes non-zero as a result of vortex generation. Then, these vortices oscillate to produce the so-called Kármán vortex street, while the drag increases gradually together with the flow speed. At even higher velocity, the boundary layer turns into a chaotic turbulent flow. It is natural to expect that the turbulent drag would be higher than that in the laminar flow case. Nonetheless, a surprise is that there is a range of Reynolds numbers for which the turbulent drag is somewhat less than that in the laminar case. It is observed experimentally that a roughened cylinder or a ball will pass the turbulent flow at a lower Reynolds number than a smooth cylinder or a ball. At first sight, this results in a rather paradoxical result: there is a small range of Reynolds numbers for which the drag of a roughened body is less than the drag of a smooth body of the same size. For a good example, we can recall a golf ball having special dimples. Indeed, the golf with those dimples flies better than an analogous smoothed one [1].

Physical analogies meet together and are accomplished themselves in most applications. Can we find out an effect similar to the abovementioned dimpled ball that flies better in the area of solid mechanics? We know that the hydrodynamic drag evolves throughout the sequence of bifurcations. But any bifurcation is inherent in nonlinear systems. Therefore, our study should deal with nonlinear mechanical systems. In mechanical engineering, the machines, sensors, and other useful devices are of interest. One of them is a solid-state wave gyro from the family of microelectromechanical system/nanoelectromechanical system (MEMS/NEMS) devices. Let us briefly touch some key points of this topic.

In the nineteenth century, people held no doubt that the Earth is turning about its axis. However, there were no direct proofs. For this reason, Léon Foucault had managed in 1851 his famous experiment with the giant pendulum. The heart of his experiment is the inertia of the pendulum or the resistance to change the motion. This means that the swing plane remains to be fixed in Newton's absolute frame of references; moreover, this evidence can be traced with the naked eye due to the slow clockwise veering since the Earth rotates anti-clockwise. However, Foucault's pendulum has one essential flaw, namely the dependence on the latitude and its giant size suppressing the energy dissipation for a while. That is why, in 1852, though an idea, we should note, was not new, Foucault produced a compact and convenient gyroscopic setup based on the immobility of the axis of a rotating mass. It was a prototype of a

conventional gyro providing needed horizons at sea and then in the air. The irony of fate, when the twentieth century was ending, the old idea came back to use a Foucault-pendulum-based device as a high precision gyroscope, although, in the other role of a thin axisymmetric solid-state resonator, associated with satellite guidance systems intended for long-term missions extending up to 15 years [6].

In 1890, Bryan demonstrated that the revolving of the standing wave nodes records effectively the rotation of the elastic resonator, as equally as a material point tends to conserve the spatial position in Newton's space. This evidence was not so new. Yet before Bryan's experiments, it was well known that the plane of transverse vibration of a straight wire will remain fixed in space instead of turning, though the wire rotates slowly about its axis during oscillations. Bryan noticed that when the vibrating body is such as a bell, rotation about its axis will produce an intermediate effect: the nodal meridians revolve with angular velocity less than that of the resonator that exhibits a new finding which yet nothing is easier than to be verified experimentally. He selected a champagne glass, then struck it to get a pure tone and when the glass turns around, Bryan heard sound beats demonstrating that the nodal meridians do not remain fixed in Newton's absolute space. He evaluated that the nodal angular velocity is about 3/5 of this almost hemispherical resonator [7]. Although, only in the second half of the twentieth century, Bryan's effect gets a wide extent turning into a concept of a prototype of an angle sensor that possesses a lot of advantages compared with a conventional gyro because its core is a monolith [8–10]. Moreover, if the power of the wave gyro is lost for a short time, the resonator conserves the angular rate, so that when the power returns, the gyro need not be reinstalled, etc., unlike, for instance, optical gyroscopes.

Let us now recall some mathematical aspects of the problem along the natural evolution of ideas. The role of the most simple mechanical system, appearing as an abstract oscillatory gyro *in vitro*, can play a circular Foucault pendulum. The corresponding mathematical model can be given by the following two differential equations:

$$\begin{aligned} \ddot{x} - 2\Omega \sin \varphi \dot{x} + \omega^2 x &= 0; \\ \ddot{y} + 2\Omega \sin \varphi \dot{y} + \omega^2 y &= -r\Omega^2 \sin \varphi \cos \varphi, \end{aligned} \quad (1)$$

where  $\varphi$  defines the latitude of geographical place;  $\Omega$  is the Earth's angular velocity in absolute value;  $r$  is the Earth's radius plus a distance from the point where the pendulum is suspended. It is supposed that Earth rotates about the axis  $z$ . Here,  $x(t)$  and  $y(t)$  denote the pair of projections of infinitesimal oscillations of the bob, weight  $mg$ , in the rotating Cartesian frame of references  $(O, x, y, z)$ . The origin  $O$  belongs to the Earth's center while the plane  $(O, x, z)$  passes through both poles. For operating such a gyro *in vita*, the pendulum should be excited to vibrate. Moreover, the amplitude of oscillations has to be maintained on some sensitive level because of energy dissipation. The presence of damping requires permanently pumping the energy into these oscillations by external forces for a permanent operating.

Almost a half century later, Bryan has derived his equation describing two similar vibration forms which, traveling toward a thin rotating ring, produce phenomena of beats, and which, in the case of high-frequency oscillations like those of sound, can detect effects of slow rotation about the sensitivity axis:

$$\begin{aligned}
v_{t,t} - v_{\theta,\theta,t,t} - 4\omega v_{\theta,t} + (\omega^2 - \mu)v_{\theta,\theta} + \frac{T(2v_{\theta,\theta} + v_{\theta,\theta,\theta,\theta})}{\sigma a^2} \\
= \frac{\beta(v_{\theta,\theta,\theta,\theta,\theta,\theta} + 2v_{\theta,\theta,t,t} + v_{\theta,\theta})}{\sigma a^4}.
\end{aligned} \tag{2}$$

Here,  $v = v(\theta, t)$  and  $w(\theta, t)$  are the tangential and radial components of displacements measured in the rotating polar frame of references;  $(a + w, \theta)$ , at time  $t$ . The symbol  $\omega$  denotes the angular rate;  $a$  is the radius of the ring;  $\sigma$  is mass density;  $T = \sigma a^2(\omega^2 - \mu)$  stands for an attractive force  $\mu$ , times the distance, directed toward the axis. We can consider this model of the circular ring as a prototype of a solid-state wave gyro to trace the precession of the flexural standing wave *in vacuo*, that is, in the absence of damping. However, the energy dissipation always presents in nature. Therefore, this system requires some external feedback control to supply the wave motion. The principal parametric resonance is a good way to excite such a gyro by driving the axisymmetric tension  $T$ . Nonetheless, some feedback is in need since the parametrically excited oscillations are always unstable either in the presence or in the absence of damping [8]. To maintain the functionality as well as the sensitivity of a conventional wave gyro in practice, the driving of standing waves requires a sophisticated feedback control to eliminate the unstable oscillations caused by their parametric excitation. Therefore, such a kind of wave excitation looks as not quite satisfactory from the viewpoint of actuation, driving or stability properties. Since the linear theory is not able to achieve the desired goal, it is necessary to look for other theoretical tools within the nonlinear wave dynamics. Our thought is to use the exclusive property of the axisymmetric mode of the ring to control the amplitude of flexural waves in the gyro in the presence of energy dissipation, just to use this one as a sort of catalysator in the dynamical process. This chapter demonstrates that when both the primary resonant pumping over the axisymmetric mode and the principal parametric resonant excitation are combined, such a gyro can operate without any feedback, just at the expense of the natural nonlinearity of the resonator in a post-bifurcation regime.

## 2. Spring pendulum

Before all the theoretical approaches related to a wave resonant solid-state gyro, it may be of place to consider a most simple mechanical system which behaves analogously and contains no excess detail, in order to explain from first principles why the nonlinearity stabilizes unstable parametric oscillations, at the expense of resonance experienced in the mechanical system. The best candidate seems to be a spring pendulum.

Therefore, let us consider a pendulum swinging in a plane and consisting of a bob of mass  $m$  attached to a spring with the stiffness  $k$  and of the natural length  $l$ . Under the Earth gravity, the equilibrium length of the pendulum becomes  $l + \Delta$ , where  $\Delta = mg/k$  denotes the spring elongation. After introducing the time-dependent radial coordinate  $r(t)$ , perpendicularly to the pivot of the spring, and the angle  $\theta(t)$  between the spring and the vertical, the equations governing the motion can be derived easily by using the following Lagrangian function:

$$\mathcal{L} = m \left[ \dot{r}^2 + (l + r)^2 \dot{\theta}^2 - \left( \dot{r}^2 + (l + r)^2 \dot{\theta}^2 \right) / 2 \right] + kr^2 / 2 + mg[(l + r)1 - \cos \theta - r]. \tag{3}$$



Alternatively, we may follow the Hamiltonian approach:

$$\mathcal{H} = \frac{p_1^2}{m} + \frac{p_2^2}{m(l+q_1)^2} - \frac{1}{2m} \left( \frac{p_1^2}{m^2} + \frac{p_2^2}{(l+q_1)^2 m^2} \right) + \frac{kq_1^2}{2} + mg((l+q_1)(1 - \cos q_2) - q_1), \quad (4)$$

and then writing the following set of Hamiltonian equations:

$$\begin{aligned} \dot{q}_1 &= \frac{p_1}{m}; & \dot{q}_2 &= \frac{p_2}{m} (l + \Delta + q_1)^{-2}; \\ \dot{p}_1 &= \frac{p_2^2}{m} (l + \Delta + q_1)^{-3} - kq_1 + mg(\cos q_2 - 1); \\ \dot{p}_2 &= -mg(l + \Delta + q_1) \sin q_2, \end{aligned} \quad (5)$$

where  $q_1 = r, q_2 = \theta, p_1 = m\dot{r}, p_2 = m(l+r)^2\dot{\theta}$  are the canonical coordinates. For further preparations, it is convenient to pass from the physical coordinates to dimensionless variables:  $t = \tau/\Omega_1; p_1 = lm\Omega_1 z_3; p_2 = l^2 m(\Omega_1^2 + \Omega_2^2)^2 z_4/\Omega_1^3; q_1 = lz_1; q_2 = z_2$ , where  $\Omega_1 = \sqrt{k/m}$  and  $\Omega_2 = \sqrt{g/l}$  denote the natural radial and angular frequencies of the pendulum with an inextensible thread at small oscillations. Notice that the angular frequency would be somewhat lower in the case of extensible thread, namely  $\nu = \Omega_2/\sqrt{\Omega_1^2 + \Omega_2^2}$ . In the new dimensionless variables, equations of infinitesimal oscillations would read

$$\begin{aligned} \frac{dz_1}{d\tau} &= z_3; & \frac{dz_2}{d\tau} &= z_4; \\ \frac{dz_3}{d\tau} &= -z_1; & \frac{dz_4}{d\tau} &= -\nu^2 z_2. \end{aligned} \quad (6)$$

Let us now consider small-but-finite oscillations of the pendulum. In this case, the general solution to the set (6) can be represented as follows:

$$\begin{cases} z_1(\tau) = -\mu A_1(T) \cos(\varphi_1(T) + \tau); \\ z_2(\tau) = -\mu A_2(T) \cos(\nu\tau + \varphi_2(T))/\nu; \\ z_3(\tau) = \mu A_1(T) \sin(\varphi_1(T) + \tau); \\ z_4(\tau) = \mu A_2(T) \sin(\nu\tau + \varphi_2(T)) \end{cases} \quad (7)$$

to look for solutions to Eq. (5) with unknown amplitudes  $A_i$  and phases  $\varphi_i$  slowly evolving in the new slow time  $T = \mu\tau$ , where  $\mu$  is arbitrary small-scaling parameter. The substitution from Eq. (7) into Eq. (5), and ordering in  $\mu$ , yields the following set of first-order approximation evolution equations:

$$\begin{aligned} \frac{dA_1}{dT} &= -\frac{A_2^2}{2} \sin \Phi; \\ \frac{dA_2}{dT} &= \frac{9A_2 A_1}{32} \sin \Phi; \\ \frac{d\Phi}{dT} &= \left( \frac{9A_1}{16} - \frac{2A_2^2}{A_1} \right) \cos \Phi, \end{aligned} \quad (8)$$

under the one assumption that the following integer-valued ratio between the frequencies, manifesting the primary parametric resonance, that is,  $1 : \nu = 1 : 2$ , takes place. Notice that the set (8) contains the so-called generalized phase  $\Phi(T) = \varphi_1(T) - 2\varphi_2(T)$ , as the unknown variable. The set (8) is of Hamiltonian structure. So, the related average Hamiltonian function reads

$$A_2^2(T)A_1(T) \cos \Phi(T) = A_2^2(0)A_1(0). \quad (9)$$

Moreover, Eq. (8) possesses one more additional integral of motion:

$$\mathcal{E} = \frac{9A_1^2}{32} + \frac{A_2^2}{2}, \quad (10)$$

where  $\mathcal{E} = 9A_1^2(0)/32 + A_2^2(0)/2$  is the average kinetic energy of the pendulum defined at the initial instant of time. These two integrals, Eqs. (9) and (10), allow us to integrate the set (8) analytically in terms of Jacobi elliptic functions [3].

Let us now refer to the damped forced motion of the pendulum. In this case, equations governing the motion (5) can be easily modified to the following form:

$$\begin{aligned} \dot{q}_1 &= \frac{p_1}{m}; & \dot{q}_2 &= \frac{p_2}{m}(l + \Delta + q_1)^{-2}; \\ \dot{p}_1 &= \frac{p_2^2}{m}(l + \Delta + q_1)^{-3} - kq_1 + mg(\cos q_2 - 1) - 2\mu\delta p_1 - \mu F \cos(\Omega_1 t + \psi_1); \\ \dot{p}_2 &= -mg(l + \Delta + q_1) \sin q_2 - 2\mu\delta p_2, \end{aligned} \quad (11)$$

where  $\delta$  is the viscous drag coefficient;  $F$  is the amplitude of an external harmonic force acting at the resonant frequency of free radial oscillations of the pendulum. We can utilize the same ansatz (7) to derive the truncated set of modulation equation for slowly varying amplitudes and phases. Small parameter  $\mu$  emphasizes that both the damping and forcing are small but finite. After the substitution from Eq. (7) into Eq. (11), and ordering in  $\mu$ , the first-order approximation evolution equations describing the resonant excitation of the pendulum over the radial mode can be written as

$$\begin{aligned} \frac{dA_1}{dT} &= -A_2^2 \sin \Phi/2 + G - \Lambda A_1; \\ \frac{dA_2}{dT} &= \frac{9A_2 A_1 \sin \Phi}{32} - \Lambda A_2; \\ \frac{d\Phi}{dT} &= -\left(\frac{A_2^2}{2A_1} + \frac{9A_1}{16}\right) \cos \Phi. \end{aligned} \quad (12)$$

These equations take in a natural manner into account the so-called triad-angle locking phenomenon described in [2], when both the phase of external force and the phase of radial oscillations have to be coupled, that is,  $-\varphi_1(T) + \psi_1 = \pi/2$ , accordingly the phase matching conditions. Notice that the parameter  $G = F/6mg$ , entering Eq. (12), is interpreted as the dimensionless force, while  $\Lambda = \delta/\Omega_1$  stands for the dimensionless drag coefficient.

In the case of stationary motion, when the amplitudes are constants, Eq. (12) produces the following algebraic set of equations:

$$-A_2^2/2 + G - \Lambda A_1 = 0; \quad \frac{9A_2A_1}{32} - \Lambda A_2 = 0; \quad \Phi(T) = \pi/2, \quad (13)$$

having the following solutions:

$$A_1 = \frac{G}{\Lambda}, A_2 = 0, \quad \text{when } K \leq \frac{32\Lambda^2}{9}; \quad (14)$$

and

$$A_1 = \frac{32\Lambda}{9}, A_2 = \sqrt{18G - 64\Lambda^2}/3, \quad \text{as } K > \frac{32\Lambda^2}{9}. \quad (15)$$

These solutions, Eqs. (14) and (15), are plotted in **Figure 1**. As we can see, the dimensionless parameter  $K$  plays the role of control parameter governing the bifurcation of the system. The stationary solution (14) near the bifurcation point  $\bar{K} = 32\Lambda^2/9$  becomes unstable and gives way to the new stationary steady state (15).

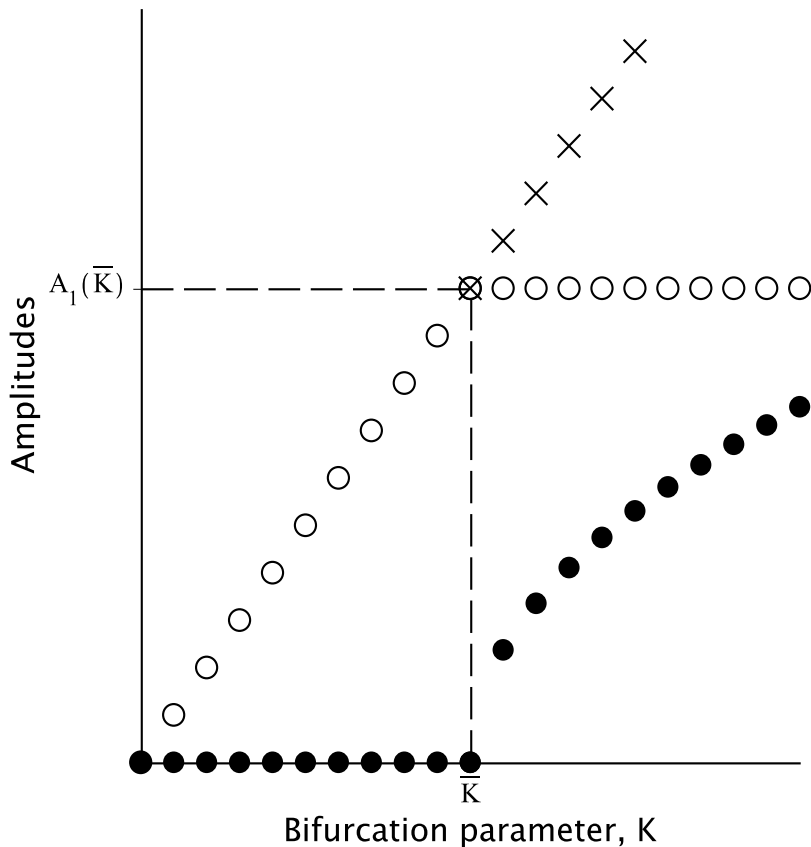


**Figure 1.** Bifurcation diagram—Amplitudes of radial and angular modes versus control parameter  $K$ . Solid circles refer to stable angular oscillations, circles mark stable radial oscillations. Crosses denote unstable radial mode. Change in the stability takes place near the bifurcation point  $\bar{K}$  (parameter  $\Lambda = 3/8\sqrt{2}$  has been scaled arbitrary for the best view).

To examine the stability properties without any excess mathematical preparations, let us analyze the power of drag forces using the energy balance resulted from the set (12):

$$\frac{d}{dT} \left( \frac{9A_1^2}{16} + A_2^2 \right) = -\Lambda \left( \frac{9A_1^2}{16} + A_2^2 \right) + \frac{9GA_1}{16}. \tag{16}$$

For the stationary orbits, the left-hand term of this equation is zero. Since the right-hand term, representing changes of the average kinetic energy in time, is also zero, then the power of drag forces should be, in turn, proportional to the kinetic energy with a negative sign. The diagram of the average kinetic energy as the function of control parameter  $K$  is shown in **Figure 2**. As we can see, the power of drag forces reduces after the bifurcation under the same external harmonic excitation. This means stability.

Let us now refer to the original Eq. (11) to verify results yielded by the modulation theory. To plot the numerical results, we have used the following transform:  $t = \tau\sqrt{m/k}$ ;  $p_1(t) = lm\sqrt{k/m}z_3(\tau)$ ;  $p_2(t) = m\sqrt{k/m}(mg + lk)^2z_4(\tau)/k^2$ ;  $q_1(t) = lz_1(\tau)$ ;  $q_2(t) = z_2(\tau)$ , from the physical to dimensionless variables. The numerical parameters of the system are chosen by us as

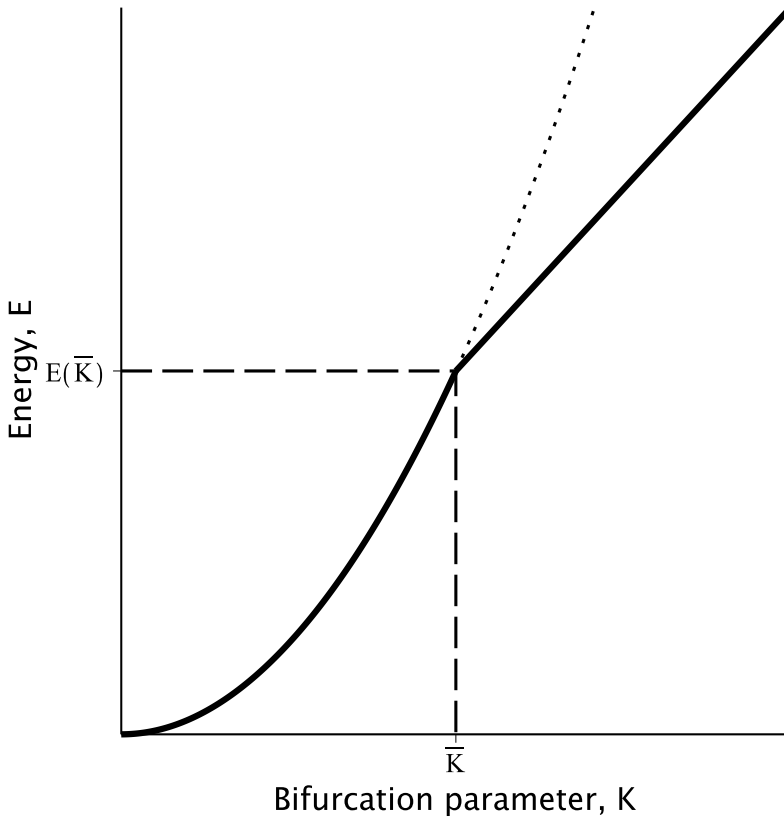


**Figure 2.** Bifurcation diagram—Average kinetic energy versus control parameter  $K$ . Solid lines refer to stable oscillations while dotted line marks unstable regime of oscillations. Parameter  $\Lambda$  is the same as in **Figure 1**.

follows:  $F = 1.0 \text{ N}$ ;  $\beta = 0.01 \text{ kg/s}$ ;  $\delta = 0.01 \text{ s}^{-1}$ ;  $g = 9.8 \text{ m/s}^2$ ;  $k = 29.40 \text{ kg/s}^2$ ;  $l = 1.0 \text{ m}$ ;  $m = 1.0 \text{ kg}$ .

Since we are studying a damped forced motion, the initial conditions to the governing equations rewritten in terms of either the physical or the dimensionless variables  $z_i(\tau)$  cannot play any role at large times, though we have decided to start in our calculations from the static equilibrium point. **Figure 3(a)** displays the time history of the radial coordinate of the system governed by Eq. (11), rewritten in new dimensionless variables  $z_i(\tau)$ , while the evolution of the angular oscillations is shown in **Figure 3(b)**. **Figure 4** displays a typical Lissajous curve that appears on  $(z_1, z_2)$  cross section of the four-dimensional phase space for the fully developed stationary state. **Figure 5** shows individual cross sections related to the radial and angular vibrations in the developed stationary regime of oscillations. Finally, **Figure 6** exhibits the evolution of the Hamiltonian function (4) or the energy of the system (11) in comparison with that one where the angular coordinate is fixed to zero but the force excitation remains the same. Notice that if the angular coordinate is fixed, then the pendulum just performs linear oscillations in the radial direction.

In new dimensionless variables  $z_i(\tau)$ , the energy of the oscillating pendulum is given by the following explicit expression:

$$E(\tau) = \frac{1}{18(z_1 + 1)^2} \left( -54(z_1 + 1)^3 \cos z_2 + 81z_1^4 + 162z_1^3 + (81z_3^2 + 135)z_1^2 + (162z_3^2 + 108)z_1 + 81z_3^2 + 256z_4^2 + 54 \right). \quad (17)$$

Mathematically, the above results represent direct proofs that in our case the modulation theory has more advantages in comparison with numerical investigations. At small and even moderate oscillations, this asymptotic approach allows us to make up a complete parametric analysis of the system under the study. Pragmatically, stability properties demonstrated using the above example of a spring oscillator in post-bifurcation regime can be used when designing an idea of a high-precision angular sensor which can appear in the form of a circular Foucault pendulum, in most simple case, or as a solid-state wave gyro with axisymmetric resonator in more general case (for instance, see [4, 5] and references therein).

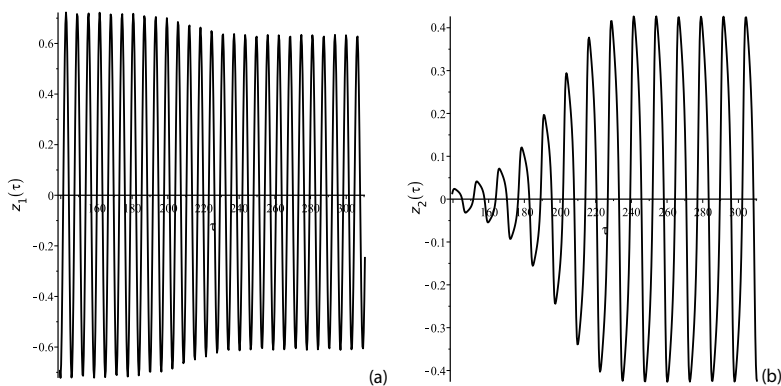


**Figure 3.** The evolution of the damped forced radial coordinate of the pendulum in time  $\tau$  (a) and the time history of the resonantly excited angular coordinate of the pendulum in time  $\tau$  (b).

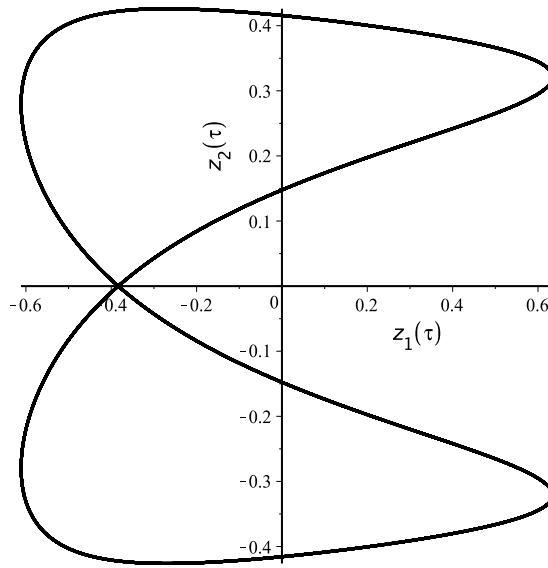


**Figure 4.** The evolution of the damped forced radial coordinate of the pendulum in time  $\tau$ .

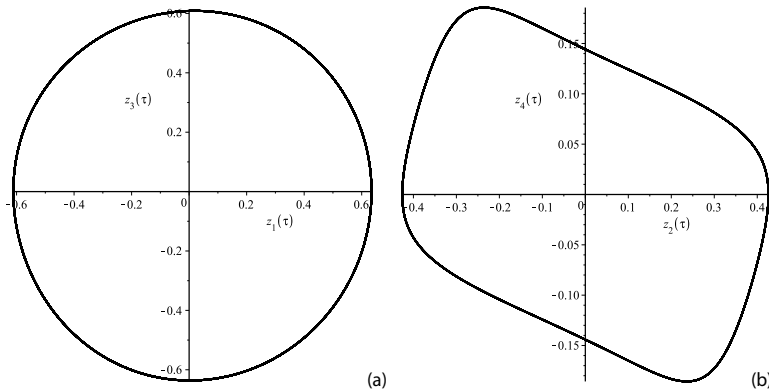


**Figure 5.** Cross sections of the phase space demonstrating individual dynamical behavior over the radial (a) and angular coordinates (b) at the damped forced oscillations in a spring pendulum in time  $\tau$ .

Gradually, one may always construct an appropriate theory by further developing the model given by Eq. (1). Nonetheless, here we decided to invoke more general case in our consideration, namely a thin-ring resonator of which is described in detail in [11].

### 3. Thin-ring resonator

In order to define the in-plane position in a thin-ring resonator, thickness  $h$  and radius  $R$ , rotating with angular velocity  $\Theta$  about its sensitive axis, we introduce the two frames of polar

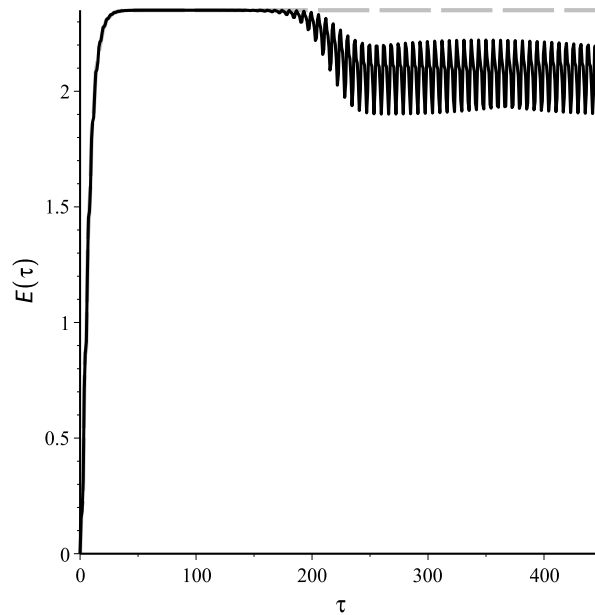


**Figure 6.** Energy of the pendulum becomes some lower in comparison with the same system with fixed angular coordinate. Dashed line refers to a spring pendulum with constrained to zero angular coordinate.

coordinates in the absolute Newton's space  $(R + w, \phi + v/R)$  and in the rotating plane  $(R + w, \varphi + v/R)$  where both have the same center as pole. Here,  $w$  and  $v$  are radial and tangential displacements of the ring, respectively. Therefore, we shall have

$$\phi = \varphi + \Theta t,$$

if the ring rotates uniformly in time  $t$ . Also, we may suppose that the angular rate as a slowly varying function of time. In this case, the latter expression is slightly modified by the following integral:

$$\phi = \varphi + \int_{t_0}^t \Theta(\tau) d\tau.$$

Equations of motion are derived from the theory of thin-walled shells that uses Kirchhoff-Love hypotheses. So, the field of displacements in the ring is expressed as  $u_{(s)} = v - \zeta(w_s - v/R)$  and  $u_{(\zeta)} = w$ , where  $v = v(s, t)$  and  $w = w(s, t)$  are the components of displacements, rewritten as functions of the circumferential coordinate  $s$ ;  $\zeta$  is the distance from the mid-line along the radius.

In the rotating frame of references, the Lagrangian density of the system reads

$$\mathcal{L} = \frac{\rho F}{2} \left[ (v_t + \Theta w + R\Theta)^2 + (w_t - \Theta v)^2 \right] - \frac{EF\kappa^2}{2R^2} v^2 - \frac{1}{2} \int_{-h/2}^{h/2} E\epsilon_{ss}^2 d\zeta,$$

where  $E$  is Young's modulus;  $F$  denotes cross-section square;  $\rho$  is mass density;  $\kappa$  characterizes the stiffness of the rotating platform of the ring;  $\epsilon_{ss} = v_s + w/R + \xi(w_{s,s} - v_s/R) + w_s^2/2$  is the circumferential component of the deformation tensor. According to paradigms of the variational analysis, equations governing the motion in the ring have the following form:

$$\begin{aligned} (\mathcal{L}_{\dot{v}})_t + (\mathcal{L}_{v_s})_s - \mathcal{L}_v &= Q_{(v)} - \mathcal{R}\dot{v}; \\ (\mathcal{L}_{\dot{w}})_t + (\mathcal{L}_{w_s})_s - (\mathcal{L}_{w_{s,s}})_{s,s} - \mathcal{L}_w &= Q_{(w)} - \mathcal{R}\dot{w}, \end{aligned} \quad (18)$$

where  $Q_{(v)}$  and  $Q_{(w)}$  are introduced as generalized forces; the function  $\mathcal{R} = \eta K$ , expressed through the kinetic energy  $K$ , is respective for the energy dissipation model linearly scaled by the coefficient  $\eta$ . For further preparations, it seems to be continent to rearrange these equations to dimensionless notation:

$$\begin{aligned} \ddot{v} + 2\mu\Omega\dot{w} + \mu\dot{\Omega}w + \dot{\Omega}/\epsilon - \mu^2\Omega^2v - V_\varphi + \epsilon^2W_{\varphi,\varphi} + \kappa^2v &= \frac{\epsilon\mu}{2}(w_\varphi^2)_\varphi + Q_{\dot{v}}; \\ \ddot{w} - 2\mu\Omega\dot{v} - \mu\dot{\Omega}v - \mu^2\Omega^2w - \mu\Omega^2/\epsilon + V + \epsilon^2W_{\varphi,\varphi,\varphi} & \\ = \epsilon\mu \left[ (Vw_\varphi)_\varphi + \frac{w_\varphi^2}{2} \right] + \frac{\epsilon^2\mu^2}{2}(w_\varphi^3)_\varphi + Q_{\dot{w}}, & \end{aligned} \quad (19)$$

where  $\epsilon = h/\sqrt{12}R \ll 1$  is the relative thickness of the ring; small parameter  $\mu = a/R \ll 1$  is intended for making up further procedures of the perturbation analysis; the functions  $V = v_\varphi + w$  and  $W = w_\varphi - v$  are written for brevity. The transform to these dimensionless variables reads:  $v(\tau, \varphi) \rightarrow v(s, t)/\mu a$ ;  $w(\tau, \varphi) \rightarrow w(s, t)/\mu a$ ;  $\varphi = s/R$ ;  $\tau = tc/R$ ;  $\Omega(\tau) = \Theta(t)R/\mu c$ . Here,  $c = \sqrt{E/\rho}$  denotes the wave propagation velocity;  $a = h/\sqrt{12}$ .

Finally, we should provide the set (19) by the periodicity conditions

$$v(\varphi, \tau) = v(\varphi + 2\pi, \tau); \quad w(\varphi, \tau) = w(\varphi + 2\pi, \tau). \quad (20)$$

### 3.1. Dispersion relation

For studying the wave propagation in the rotating frame of references, it is convenient to define linear modes of oscillations in the ring on the fixed platform. If the rotation is absent, then the normal modes of vibrations represent standing waves being a superposition of two waves traveling toward identical wave numbers, frequencies as well as amplitudes. First of all, we should understand how the spectrum of these oscillatory modes would change in the uniformly rotating ring. Are there the standing modes taking place? And if these cannot be detected, then, what thing should we invoke instead into our study? We know that the precession of waves appears as a reaction on the rotation. Therefore, there will be expected some asymmetry in the polarization vectors of traveling waves. One more finding is we know that the precession rate of waves has to be proportional to the difference between the frequencies in the wave pair as if those compose a standing wave in the ring being at rest. Let the angular rate in the ring be constant and then the wave precession should appear as some sort of kinematic reactions on the rotation of the ring platform. But if the platform rotates with acceleration, then we can expect a kind of some dynamical response that may appear as



essentially differ from kinematic one. Fortunately, experiments with revolving axisymmetric bodies tell us that the expression for the uniformly rotating ring, which will be done subsequently, is equally valid in both cases of the uniformly rotating ring and in the motion with arbitrary, but moderate, angular acceleration [8].

In the case of uniform rotating, a simple solution of the linearized set (19) is given by

$$v(\tau, \varphi) = -\frac{\mu\Omega^2}{\epsilon(\mu^2\Omega^2 - 1)} + B \exp i(n\varphi + \omega\tau); \quad w(\tau, \varphi) = A \exp i(n\varphi + \omega\tau),$$

Here, we can trace the appearance of the constant extension in radial direction caused by the centrifuge force. Notice that the amplitudes,  $A$  and  $B$ , entering therein, are linearly interrelated, that is,  $B = pA$ , through the interrelation coefficients,  $p$ , defined for both the high- and low-frequency sets of normal modes:

$$p_{k,n} = -\frac{i(2\mu\Omega\omega_{k,n} + n(1 + \epsilon^2n^2))}{n^2(1 + \epsilon^2) + \kappa^2 - (\omega_{k,n}^2 + \mu^2\Omega^2)}. \quad (21)$$

The high- and low-frequency branches are indexed by  $k = 1$  and  $k = 2$ , correspondingly. Recall from the linear algebra that these coefficients should satisfy the orthogonality condition, that is,  $p_{1,n}p_{2,n} = -1$ , for arbitrary wave number  $n$ , excluding the one case of linearly decoupled oscillations, taking place at  $n = 0$ , that is, at axisymmetric radial oscillations. The natural frequencies of waves,  $\omega_{k,n}$ , are defined by the dispersion relation

$$(n^2(1 + \epsilon^2) + \kappa^2 - (\omega^2 + \mu^2\Omega^2))(1 + \epsilon^2n^4 - (\omega^2 + \mu^2\Omega^2)) - (2\mu\Omega\omega - n(1 + \epsilon^2n^2))^2 = 0. \quad (22)$$

Let the angular velocity be zero and then the dispersion relation turns into the simple algebraic equation

$$-n^6\epsilon^2 - \epsilon^2(-\omega^2 - 2 + \kappa^2)n^4 + ((\omega^2 - 1)\epsilon^2 + \omega^2)n^2 - \omega^4 + (1 + \kappa^2)\omega^2 - \kappa^2 = 0, \quad (23)$$

Two identical ones of all the four roots of Eq. (23) are shown in **Figure 7**. The low-frequency branch refers in general to the bending modes while the high-frequency ones reply mainly to the circumferential modes of extension.

In the case of a small angular rate, that is,  $\Omega \ll \omega_{k,n}$ , the roots of the dispersion relation (22) are approximately represented as follows:

$$\omega_{k,n}(\Omega) \approx \omega_{k,n}(0) + \frac{2\mu\Omega n(1 + \epsilon^2n^2)}{1 + \epsilon^2n^4 + (1 + \epsilon^2)n^2 + \kappa^2 - 2(\omega_{k,n}(0))^2}. \quad (24)$$

It may not, perhaps, be out of place to note that these roots possess by asymmetry because of the angular rate. Nonetheless, each frequency,  $\omega_{k,n}$ , can be decomposed on the antisymmetric term as well as on the symmetric part. The antisymmetric term is respective for the wave precession caused by the ring rotation while the symmetric one describes a small inessential correction.

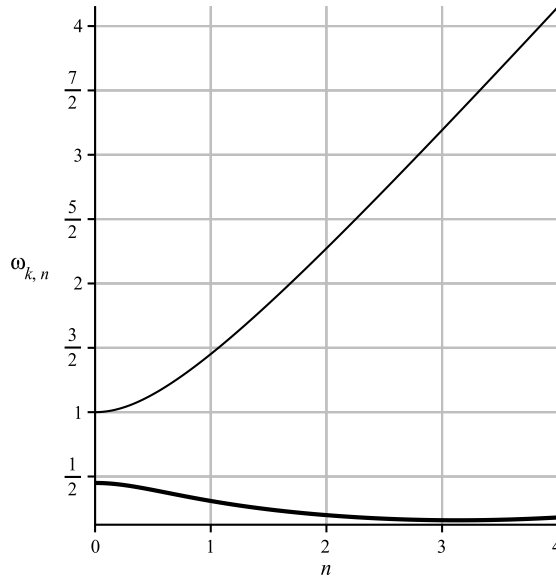


Figure 7. The high- and low-frequency dispersion branches for waves on the fixed platform ( $\epsilon = 0.01, \kappa = 0.45, \Omega = 0$ ).

#### 4. Nonlinear resonant coupling between the axisymmetric radial oscillation and two similar bending wave forms being in phase

This section invokes briefly some general points from the common theory of waves, including understanding phenomena of resonance experienced in nonlinear mechanical systems and some mathematical preparations which are necessary to investigate the given problem from the viewpoint of the perturbation analysis, using methods of slowly varying amplitudes and phases. Then, we generalize the problem by considering the case of damped forced oscillations in a thin circular ring. This generalization of the problem leads to a thought on how to excite stable wave precession regimes which need no feedback to repair unwanted motions in the solid-state wave gyro.

##### 4.1. Triple-mode resonant coupling between waves in the ring

Truncated equations or evolution equations describing the modulation phenomena of amplitudes and phases can be directly obtained using the following anzats [12–15]:

$$v(\tau, \varphi) = \sum_{k=1}^3 p_k A_k(T) \exp i\phi_k; \quad w(\tau, \varphi) = \sum_{k=1}^3 A_k(T) \exp i\phi_k, \quad (25)$$

which represent an approximated solution to Eq. (19). Here,  $A_k(T)$  ( $k = 1..3$ ) are the slowly varying complex wave amplitudes, evolving at slow time  $T = \mu\tau$ ;  $\phi_1 = n\varphi + \omega_1\tau$ ,  $\phi_2 = -n\varphi + \omega_1\tau$ ,  $\phi_3 = \omega_3\tau$  are the fast rotating phases; (\*) denote the complex conjugation. Notice that the amplitude and phase number three refer to the axisymmetric radial oscillation of the ring.

We assume that the angular rate and acceleration of the ring are small enough, that is,  $\Theta(\tau) \sim \mu$  and  $d\Theta/d\tau \sim \mu^2$ . Also, we should suppose that spectral parameters of waves in the solution (25) are matched by the following phase synchronicity conditions:

$$\omega_3 = \omega_1 + \omega_2 + \mu\Delta\omega, \tag{26}$$

where  $\Delta\omega$  denotes a small discrepancy between the phases of the high-frequency axisymmetric radial oscillation and two low-frequency quasi-harmonic waves with amplitudes, numbers one and two. Certainly, all the frequencies  $\omega_1, \omega_2, \omega_3$  and the wave numbers  $\pm n$  should satisfy the dispersion relation (23). In the theory of nonlinear waves, such a trio is used to name a *resonant triplet* while the synchronicity (26) is associated with the so-called *phase-matching conditions*.

One more convenient way of obtaining the evolution equation is walking down along the Hamiltonian formalism. Let us consider the average Lagrangian of the system

$$\langle \mathcal{L} \rangle = \left( \frac{1}{2\pi} \right)^3 \int_0^{2\pi} \left( \int_0^{2\pi} \left( \int_0^{2\pi} \mathcal{L} d\phi_1 \right) d\phi_2 \right) d\phi_3, \tag{27}$$

in order than to expand this one in a formal series in small parameter  $\mu$  as follows:

$$\langle \mathcal{L} \rangle = \mathcal{L}_0 + \mu\mathcal{L}_1 + \mu^2\mathcal{L}_2 + \dots,$$

Here, zero-order approximation term, that is,  $\mathcal{L}_0 = 0$ , would coincide exactly with the dispersion relation, accordingly to findings of Whitham [16]. The second term  $\mathcal{L}_1$ , entering this expansion, describes effects arising in the first-order nonlinear approximation analysis which we need to study here. Then, the nontrivial average Hamiltonian of the system would read

$$\mathcal{H} = \sum_{k=1}^3 \left( A_{k,T} \frac{\partial \mathcal{L}_1}{\partial A_{k,T}} + \bar{A}_{k,T} \frac{\partial \mathcal{L}_1}{\partial \bar{A}_{k,T}} \right) - \mathcal{L}_1,$$

In this case of resonant coupling between the axisymmetric radial oscillation and two low-frequency bending waves, being in phase (26), this average Hamiltonian is rearranged in more pragmatic form

$$\mathcal{H} = 2i\Omega \sum_{j=1}^2 \omega_j \left( \bar{p}_j - p_j \right) |A_j|^2 + \epsilon n^2 \left[ \bar{A}_1 \bar{A}_2 A_3 \exp(i\Delta\omega T) + A_1 A_2 \bar{A}_3 \exp(-i\Delta\omega T) \right]. \tag{28}$$

Recall that the bending wave frequency  $\omega = \omega_1 = \omega_2$  should be close to the frequency  $\omega_3/2$  that denotes the frequency of the axisymmetric radial oscillation, that is,  $\omega_3 = 1$ . Note that the case under consideration is associated with the *principal parametric resonance*. His Hamiltonian produces a set of following evolution equations:

$$\begin{aligned} \frac{dA_1}{dT} &= \frac{2\Omega(\bar{p}_1 - p_1)}{1 + p^2} A_1 - \frac{i\epsilon n^2}{\omega(1 + p^2)} \bar{A}_2 A_3 e^{i\Delta\omega T} \\ \frac{dA_2}{dT} &= \frac{2\Omega(\bar{p}_2 - p_2)}{1 + p^2} A_1 - \frac{i\epsilon n^2}{\omega(1 + p^2)} \bar{A}_1 A_3 e^{i\Delta\omega T}, \\ \frac{dA_3}{dT} &= -i\epsilon n^2 A_1 A_2 e^{-i\Delta\omega T}, \end{aligned} \tag{29}$$

where  $p_k = (-1)^k i n (1 + \epsilon^2 n^2) / ((1 + \epsilon^2) n^2 - \omega^2)$  are the wave polarization coefficients which satisfy the equality  $p = |p_1| = |p_2|$ , due to the symmetry of the problem.

Now, we use the following transform of variables:

$$\begin{aligned} A_1 &= a_1 \exp \left( \frac{2(\bar{p}_1 - p_1)}{1 + p^2} \int_0^T \Omega(\zeta) d\zeta \right); \\ A_2 &= a_2 \exp \left( \frac{2(\bar{p}_2 - p_2)}{1 + p^2} \int_0^T \Omega(\zeta) d\zeta \right); \\ A_3 &= a_3, \end{aligned} \quad (30)$$

that allows us to rewrite the set (29) by getting rid of Coriolis terms:

$$\begin{aligned} \frac{da_1}{dT} &= -\frac{i\epsilon n^2}{\omega(1 + p^2)} \bar{a}_2 a_3 e^{i\Delta\omega T}; \\ \frac{da_2}{dT} &= -\frac{i\epsilon n^2}{\omega(1 + p^2)} \bar{a}_1 a_3 e^{i\Delta\omega T}; \\ \frac{da_3}{dT} &= -i\epsilon n^2 a_1 a_2 e^{-i\Delta\omega T}, \end{aligned} \quad (31)$$

Eq. (32) have now obtained a standard form similar to Euler's kinematic equations describing rotation of a rigid body with a fixed point. This set can be integrated exactly in terms of the Jacobi elliptic functions [17]. Also, here is a place to note that in the theory of nonlinear waves similar equations describe *break-up instability* phenomena when the high-frequency mode becomes unstable triad with respect to small low-frequency perturbations [12].

#### 4.2. Resonant excitation of the gyro

Let us invite in our consideration the generalized forces describing the damping and forcing of the ring resonator over the axisymmetric form of oscillation. By substituting the terms  $Q_v = -2\mu\eta\dot{v}$ ; and  $Q_w = -2\mu(\eta\dot{w} - Q \cos \varpi \tau)$  into Eq. (19), we can obtain, after the exchange of variables (30), the following set of evolution equations:

$$\begin{aligned} \frac{da_1}{dT} &= -\eta a_1 - \frac{i\epsilon n^2}{\omega(1 + p^2)} \bar{a}_2 a_3 e^{i\Delta\omega T}; \\ \frac{da_2}{dT} &= -\eta a_2 - \frac{i\epsilon n^2}{\omega(1 + p^2)} \bar{a}_1 a_3 e^{i\Delta\omega T}; \\ \frac{da_3}{dT} &= -\eta a_3 + iQ e^{i\delta T} / 2 - i\epsilon n^2 a_1 a_2 e^{-i\Delta\omega T}, \end{aligned} \quad (32)$$

that can be rewritten, after one more exchange of variables;  $a_j(T) = b_j(T) e^{i\varphi_j(T)}$ , in terms of real-valued amplitudes and phases:

$$\begin{aligned}
 \frac{db_1}{dT} &= -\eta b_1 + \frac{\epsilon n^2 b_2 b_3 \sin \psi}{\omega(1+p^2)}; \\
 \frac{db_2}{dT} &= -\eta b_2 + \frac{\epsilon n^2 b_1 b_3 \sin \psi}{\omega(1+p^2)}; \\
 \frac{db_3}{dT} &= -\eta b_3 - \epsilon n^2 b_1 b_2 \sin \psi + Q \sin(\delta T - \varphi_3)/2; \\
 \frac{d\psi}{dT} &= -\Delta\omega + \frac{-2n^2\epsilon(b_1^2(\omega(1+p^2)b_2^2 - b_3^2) - b_2^2 b_3^2) \cos \psi + \omega b_1 b_2 Q \cos(\delta T - \varphi_3)(1+p^2)}{2\omega(1+p^2)b_1 b_2 b_3}; \\
 \frac{d\varphi_3}{dT} &= -\epsilon n^2 b_1 b_2 \cos \psi / b_3 + Q \cos(\delta T - \varphi_3) / 2b_3,
 \end{aligned}
 \tag{33}$$

where  $\psi(T) = \varphi_3(T) - \varphi_2(T) - \varphi_1(T) + \Delta\omega T$ . These equations are convenient in the study of stationary damped forced motions performed in the system (32). There are two subsets of such motions; the first can be written as

$$b_1 = b_2 = 0; \quad b_3 = \frac{K(1+p^2)\eta\omega}{\epsilon n^2}, \tag{34}$$

while the second would be

$$b_1 = b_2 = \frac{\sqrt{2}\eta\omega\sqrt{1+p^2}\sqrt{K-1}}{\epsilon n^2}; \quad b_3 = \frac{\eta\omega(1+p^2)}{\epsilon n^2}. \tag{35}$$

Here, we have introduced a new notation:  $K = Qn^2\epsilon/(4(1+p^2)\eta^2\omega^2)$  for the characteristic number by analogy with Reynolds numbers in the hydrodynamics [18, 19].

Now, we may return to our preliminary study over the spring pendulum to be acquainted in similarities and analogies. Indeed, the first stationary solution (34) appears as stable only within the range  $0 \leq K \leq K^*$ . Here,  $K^* = 1$  denotes the critical value of the control parameter governing the bifurcations. This stationary solution coincides exactly with the solution if neglecting all the nonlinear terms in the system (19). Although near the point  $K^*$  this stationary solution loses its stability to give its place for the new stationary state (35). The new stationary state would be stable at  $K > 1$ . It is not now surprising that as if the bifurcation parameter  $K$  grows even further, then the energy would be pumped only into the low-frequency bending modes while the amplitude of the high-frequency axisymmetric radial mode remains to be fixed, that is,  $b_3 = \eta\omega(1+p^2)/(\epsilon n^2)$ . Probably, this mechanism represents an effective way in the problem of installation of the solid-state wave gyro.

When returning to the old notation, the solution of our problem can be expressed as it follows:

$$\begin{aligned}
 v(\tau, \varphi) &= -4pb_1 \cos(\psi(\tau) - n\varphi) \cos\left(\omega + \mu\left(\frac{\delta + \Delta\omega}{2}\right)\right)\tau + O(\mu^2\tau); \\
 w(\tau, \varphi) &= -4b_1 \sin(\psi(\tau) - n\varphi) \cos\left(\omega + \mu\left(\frac{\delta + \Delta\omega}{2}\right)\right)\tau - 2b_3 \sin(\varpi\tau) + O(\mu^2\tau),
 \end{aligned}
 \tag{36}$$

where

$$\psi(\tau) = \frac{4p}{1+p^2} \int_0^\tau \Omega(\zeta) d\zeta$$

is the precession rate. Typical patterns of the wave precession are shown in **Figure 8**.

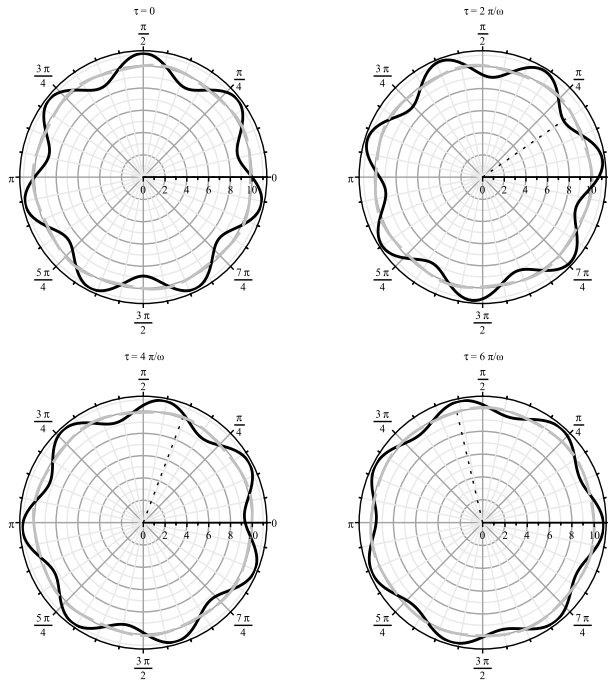


**Figure 8.** The wave precession. Modal number  $n = 7$ . Solid lines refer to flexural mode, while the dashes to the circumferential one ( $\eta = 0.1, \mu = \epsilon \approx 0.01, \kappa = 0.45, \Omega = 0.085, Q = 0.1$ ). The dotted radius indicates the rotation angle  $\Omega\tau$ . The stiffness of the gyro platform  $\kappa$  is tuned to the seventh bending modes.

### 5. Conclusion

Léon Foucault has made a sensation with his famous giant pendulum experiment in the Panthéon in Paris in 1851. That time, people could perceive the inertia of the pendulum with his naked eye to have the first direct proof that the Earth is turning anti-clockwise. Moreover, this experiment has demonstrated that a pendulum could be used as a vibratory gyro. However, a flaw of the Foucault pendulum is the dependence on the latitude. A device was needed that was unaffected by the latitude. In 1852, Foucault proposed an angular sensor based on the immobility of the axis of a rotating mass. Unlike the pendulum, this sensor could detect a fixed direction in Newton’s absolute space. Recall that a torque directing the axis of rotation of the rotor of the gyro is known as the precession. For the precision, however, this gyro required an exquisite construction, since the gyro’s rotor should be balanced as well as possible.

In 1890, Bryan investigated the nature of the beats which may be heard when a vibrating cylinder or other axisymmetric thin-walled shell of revolution has been involved in a rotatory motion about its axis [7]. Perhaps, this study had been inspired as a reply to A. E. H. Love, famous for his work on the mathematical theory of elasticity. In the paper [20], Love supposed that unless a body was revolving with the angular velocity comparable with the frequencies of the vibrations, the latter would not be almost affected. The only important effect of rotation would be an extension because of the centrifugal force. Bryan has corrected that in the axisymmetric shells at high-frequency vibrations phenomena of beats may be observed, which appears as the most noticeable effects of the rotation. It is probable that Bryan had no idea how to utilize his finding. Though those times people were in controversy on how far theory of thin-walled shells elaborated by Lord Rayleigh is capable of practice, is this perhaps just a sort of one more abstract theory? Lo and behold, initially conceived in 1890 through the observation of beats from a ringing wine glass, the concept was lost until uncovered in 1965. Due to technologies of the second half of the twentieth century, perhaps in times of Vietnam War, this physical effect has inspired a concept of a solid-state wave gyro [6]. Because there are no typical mechanical parts, these wave sensors have a lot of advantages for long-term space missions. However, to maintain the functionality as well as the sensitivity of a conventional wave gyro in practice, the driving of standing waves requires somewhat sophisticated feedback control. This chapter demonstrates that when both the primary resonant pumping over the axisymmetric mode of oscillations and advantages of the principal parametric resonance are combined, such a gyro can operate without any feedback at the expense of the natural nonlinearity of the resonator in a post-bifurcation regime.

## Author details

Svetlana Pavlovna Nikitenkova<sup>1\*</sup> and Dmitry Anatolyevich Kovrigin<sup>2</sup>

\*Address all correspondence to: [spnikitenkova@gmail.com](mailto:spnikitenkova@gmail.com)

1 Radiophysics Faculty, Nizhny Novgorod State University n.a. N.I. Lobachevsky, Nizhny Novgorod, Russia

2 Applied Mathematics Chair, Nizhny Novgorod Technical State University n.a. R.E. Alekseev, Nizhny Novgorod, Russia

## References

- [1] <https://www.grc.nasa.gov/www/K-12/airplane/dragosphere.html> (Drag of a Sphere - NASA)
- [2] Lee J. Triad-angle locking in low-order models of the 2D Navier-Stokes equations. *Physica D: Nonlinear Phenomena*. 1987;24(1-3):54-70
- [3] Sukhorukov AP. *Nonlinear Wave Interactions in Optics and Radio Physics*. Moscow: Nauka; 1988

- [4] Zhuravlev VF. Global evolution of state of the generalized Foucault pendulum. *Mechanics of Solids*. 1998;**33**(6):1-6
- [5] Stanovnik A, Jurčič-Zlobec B. Numerical study of the elastic pendulum on the rotating earth. *ISRN Mathematical Physics*. 2012, Article ID 806231;**2012**:1-7
- [6] Lynch DD. HRG Development at Delco, Litton, and Northrop Grumman. Proc. of Anniversary Workshop on Solid-State Gyroscopy (19–21 May 2008. Yalta, Ukraine). Kyiv-Kharkiv. ATS of Ukraine, ISBN 978–976–0–25248-5; 2009
- [7] Bryan GH. On the beats in the vibrations of a revolving cylinder or bell. *Proceedings of Cambridge Philosophical Society of Mathematics and Physical Sciences*. 1890;**VII**(III):101-111
- [8] Zhuravlev VF, Klimov DM. *Wave Solid-State Gyro*. Moscow: Nauka Publisher; 1985 (in Russian)
- [9] Bose A, Puri S, Banerjee P. *Modern Inertial Sensors and Systems*. Prentice-Hall of India: New Delhi, II; 2008
- [10] Osiander R, Ann Garrison Darrin M, Champion JL. *MEMS and Microstructures in Aerospace Applications*. Taylor & Francis Publisher. ISBN 0824726375; 2005
- [11] Kovriguine DA. Geometrical nonlinearity stabilizes a wave solid-state gyro. *Archive of Applied Mechanics*. 2014;**84**(2):159-172
- [12] Phillips OM. *The dynamics of the upper ocean*. Cambridge Univ. Press; 1977
- [13] Kovriguine DA, Potapov AI. Nonlinear oscillations in a thin ring - I, II. *Acta Mechanica*. 1998;**126**:189-212
- [14] Kovriguine DA. On non-linear resonant excitation of a wave solid-state gyro. Proc. of Int. Cong. MV2 New advances in modal synthesis of large structures, non-linear, damped and non-deterministic cases, Jezequel Ed., École Centrale de Lyon. 1995;**2**:575-586
- [15] Kovriguine DA. Geometrical nonlinearity stabilizes a wave solid-state gyro. *Archive of Applied Mechanics*. 2014;**84**(2):159-172
- [16] Whitham GB. *Linear and Nonlinear Waves*. New-York: Wiley-Interscience; 1995
- [17] Janke-Emde-Lösch: *Tafeln Höherer Funktionen*. Sechste auflage. Neubearbeitet von F. Lösch, B.G.Teubner, Verlagsgesellschaft. Stuttgart. 1960
- [18] Gledzer EB, Dolzhansky FW, Obukhov AM. *Systems of hydrodynamic type and their applications*. Moscow: Nauka Publisher; 1981 (in Russian)
- [19] Nayfeh A, Balachandran B. *Applied Nonlinear Dynamics: Analytical, Computational and Experimental Methods*. Wiley; 1995
- [20] Love AEH. The free and forced vibrations of an elastic spherical shell containing a given mass of liquid. *Proceedings of the London Mathematical Society*. 1887;**1**(1):170-207



---

# Wind-Induced Vibrations to Tall Buildings and Wind Turbines

---

Abdel Rahman Elbakheit

Additional information is available at the end of the chapter

<http://dx.doi.org/10.5772/intechopen.72094>

---

## Abstract

While wind generated noise maybe limited in magnitude and effect, wind-induced structures' vibrations could be a devastation (i.e., Tacoma Bridge Collapse 1940). This occurs with just above moderate wind speed increase, if it can excite a structure with its natural frequencies. When this occur, structures enter a phase of oscillations until collapse. However, with proper understanding of vibrations in structures these vibrations can be eliminated. Studying vibrations can be experimental through wind-tunnel and or by simulations. Wind in buildings can induce two types of motions: static or sustained; as building drift and oscillatory or resonant vibration. Motion is composed of three contributions: sway in two horizontal or perpendicular directions and torsion. This vibration would considerably affect the habitability and stability of building spaces gauged through a life cycle assessment study, habitability perception and determination or acceleration measurements and estimation. The novelty of aerodynamic design and optimization in providing vibration free tall buildings and wind turbines with added savings that otherwise be incurred by adoption of costly structural and/or supplementary damping technologies highlighted. Better habitability, safety and comfort without added costs. State of the art in wind vibrations reviewed, together with factors influencing control vibration in tall buildings and wind turbines.

**Keywords:** wind vibrations in tall buildings, vertex shedding in tall buildings, aerodynamic optimization of tall buildings, habitability and vibration conception in buildings, wind turbine integration in tall buildings, wind vibrations in turbines

---

# 1. Introduction

## 1.1. Building’s aerodynamic performance to control wind induced vibrations

Generally speaking Wind affects buildings with two distinct effects, Buffeting and vortex shedding [1, 2] (i.e., Drift and oscillation as mentioned above). The first happens in the along wind direction force producing drag or overturning. If we consider a wind boundary layer acting on a tall square plan buildings with an angle  $\alpha$  to the horizontal axis X, **Figure 1**. Wind velocity would be gradient along the Z-axis that is to say the highest wind speed would occur in the upper most position of the boundary layer and the lowest wind speed would be close to the ground. The building would experience a drag along all major axes X, Y, that are measured using local mean force coefficient  $C_{fD}$ , and overturning or torsional moments over the X-axis  $C_{ML}$ , over the Y-axis  $C_{MD}$ , and over the Z-axis  $C_{MT}$ , such as Shown in **Figure 1**. The second wind induced effect (i.e., Oscillations) is rather more complex in its cause, but usually happens perpendicular to the direction of wind flow and can be measured using fluctuating moments coefficient  $C_{FL}$  presented in **Figure 1**.

As an aerodynamic reaction, wind induced vibrations or oscillations always triggered by the shape and form of the object subjected to wind flow [3]. The more uniform and symmetrical the form is, the more likely for it to oscillate in wind flows. Therefore, considering these factors first would lead to permanent passive solutions to vibrations in structures due to wind. There has been growing evidence from research of wind-induced vibration that symmetrical cross sections of structures may produce vibrations to structures at one of their natural frequencies.

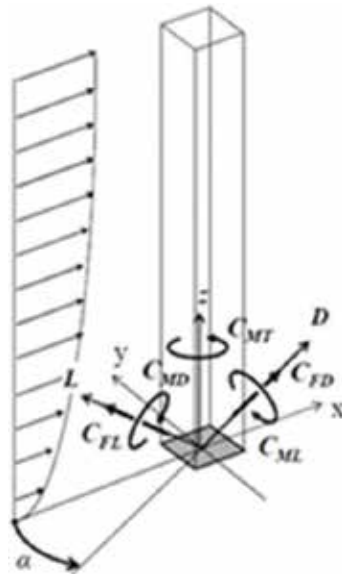


**Figure 1.** Aerodynamic forces acting on a basic square tall building.

As the expression of Strouhal gives the natural frequency  $N$  as a function of wind speed and width of the building as follows:

$$N = S \frac{u}{b} \quad (1)$$

where  $S$  = Strouhal number,  $U$  = wind speed,  $b$  = building width.

Having established that, this is generally have little effects on low-rise buildings. But the effect is highly pronounced in tall Buildings. With the new advancement in tall building structures, where high strength material coupled with reduced weight, it is made possible to design even more slender, more taller buildings quite easily and the trend is on the rise. These conditions makes high-rise buildings more prone to be excited by winds in the upper layers of the atmosphere that are usually with higher wind speed magnitudes.

On the other hand, only very specific wind speeds would cause the vertex shedding effect for any given tall structure by virtue of its three dimensional form and/or cross sectional plans. As mentioned above uniform plans of square **Figure 2**, rectangular **Figure 3**, circular **Figure 4** and similar shapes are more susceptible to trigger vertex shedding. This happens as wind approaches a high-rise structure it separated into two streams along the sides of the building by the plan shape creating equal vertices along each side faces of the building that are identical in shape and size **Figure 2**.

However, only at certain wind speeds the vertices would be greater in size and stronger in velocity magnitude to force its way on one side of the tube. Thus forcing the structure to

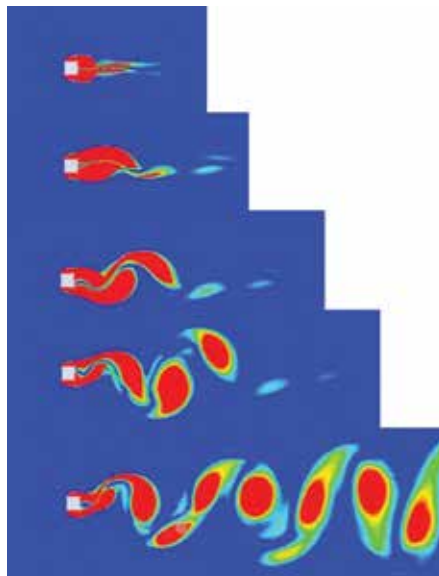


**Figure 2.** Computational fluid dynamics image for air flow around a square tube under vertex shedding effect, with stages of vertex formation.

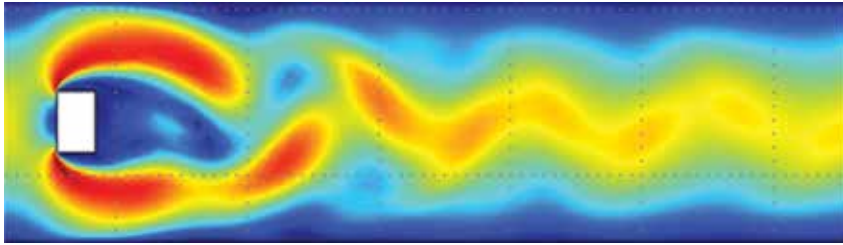


**Figure 3.** Computational fluid dynamics image for air flow around a rectangular tube under vertex shedding effect.

sway to the other side. The structure would sway back to position and beyond by virtue of its elasticity. Then comes the succeeding vertex to push the structure further to the opposite side. This is where the Oscillation process would typically start. The oscillations would be sustained by the differences in wind pressures along the opposite sides of the building swept across that eventually cause the tall structure to continue to sway in the direction perpendicular to the wind's main stream. This phenomena has been experienced widely in some industries such as factory's Chimney stacks, undersea cables, bridges, tall buildings and so forth and whenever a main stream fluid passes across a uniform geometrical object.

These oscillations of structures/objects caused by vertex shedding because of wind speed produce air pressures similar in behavior to the sinusoidal waves of sound. However, opposite in its process to the normal process of sound generation. Sound is generated whenever an object moves in air causing a succession of higher and lower pressure regions, which can be presented (i.e., heard) as a sound wave. Therefore, we can expect noise produced accompanying vertex shedding of structures or objects.

Nevertheless, with the right building three-dimensional design configuration and cross sections of it plan, it would be possible to totally control any possible wind induced vibrations in tall buildings. Thus providing great savings that otherwise needed to increase the mass (concrete), stiffness (reinforcement) and damping (restraint) needed to stabilizing structures against excessive wind vibrations.

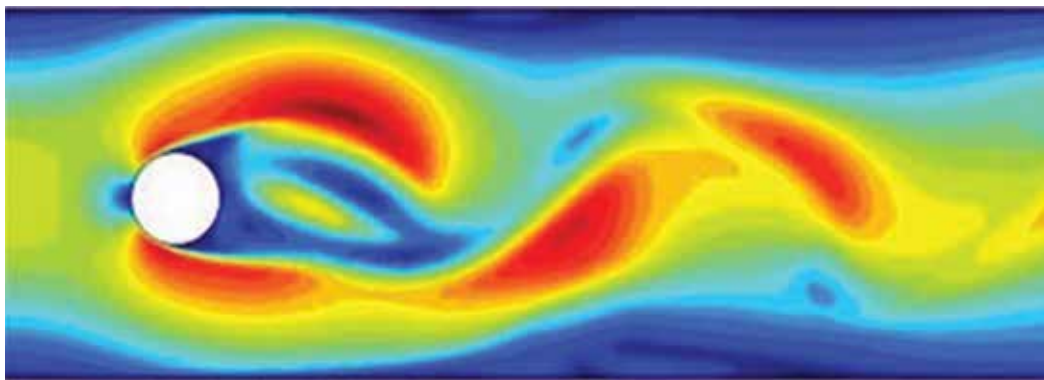


**Figure 4.** Computational fluid dynamics image for air flow around a circular tube under vertex shedding effect.

To arrive at a building form or shape that is vertex shedding free can involve computational Simulations and or wind tunnel experimentation trying to break the symmetry of the buildings plans and forms. Mooneghi and Kargarmoakhar [4], proposed minimal intervention to any proposed buildings forms by the additions of small fins and corner modifications that help considerably reduce the shedding effect. Several studies have been conducted on this subject in the past (e.g., Gu and Quan [5], Irwin [6], Irwin et al. [7]) but each case study should be carefully evaluated to avoid unfavorable effects in building behavior. This is identical to what would typically be applied in manufacturing industries exhaust or stack chimneys, undersea cables previously mentioned examples of industries. However, these solutions may not always be practically or technically feasible to integrate into building's facade systems, **Figure 5**.

A more efficient approach for dealing with this issue in buildings is to Further modify forms three dimensionally in what is known as aerodynamic design modification of building forms based on combinations of the cross sections and their combinations three dimensionally compared to basic square tall buildings. A good example for this point is Burj Khlifa Tall building in Dubai, where the building have tapering plans being reduced with height, as well as breaking the uniformity of form plans 2-dimensionally and 3-dimensionally, **Figure 6**.

Tamura et al. [8], presented a systematic study of building forms subjected to wind influence ranging from simple forms to more complex combinations under direct wind and cross winds using wind tunnel's scaled models as well as computational fluid dynamics. Among the figures tested are basic forms include Square, rectangle, Circle and ellipse, Tilted and snaked or winded three dimensional tubes. Corner modifications, tapered, bulged, helical, top-openings all in different modifications and finally composite forms of several basic shapes, **Table 1**. Totalling 31 models in 7-categories.

The study compared values of overturning moments co-efficient CMD, CML, fluctuating overturning moments co-efficient CFL, Local mean wind force co-efficient CfD, in the along

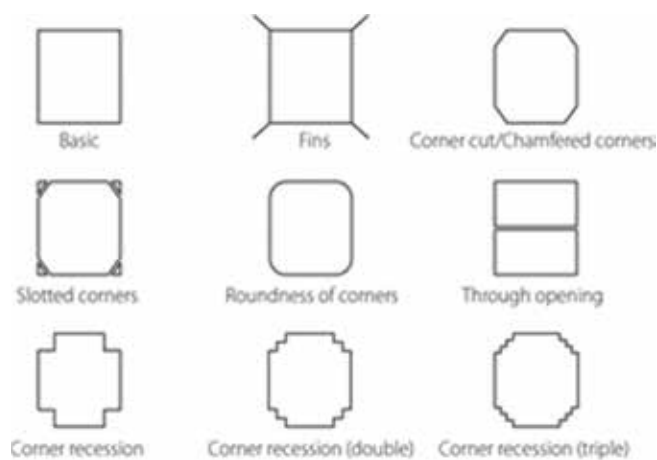


**Figure 5.** Minor aerodynamic modifications [4].

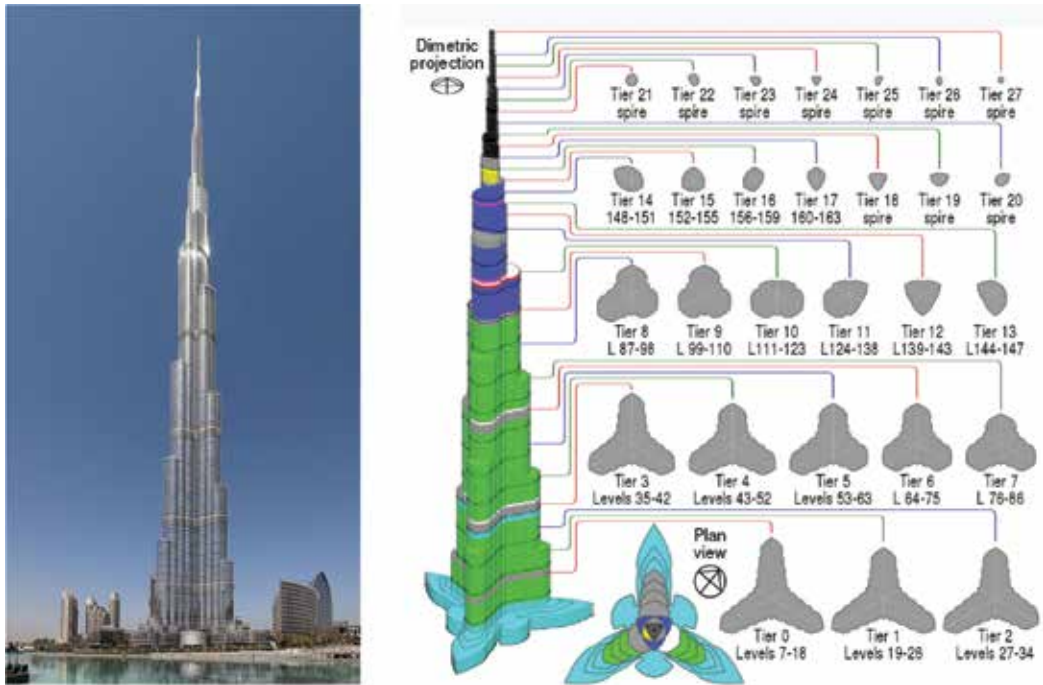


Figure 6. Burj Khalifa tower in Dubai. Modifications in plans shape and sizes with height.

wind, cross wind and torsional directions CMT, **Figure 1**. Distribution of wind pressure coefficient  $C_p$  and response analysis is also evaluated for these models. In order to determine the habitability of the studied models eigenvalue analysis and response analysis were conducted.

Corner cut and helical square models were the lowest in design values for spectral wind speed for one-year return period, which is far better than the response of the basic square model.








Basic	Corner Modified	Tilted	Tapered	Helical	Opening	Composite
Square	Chamfered	Tilted	Setback	Helical square 90°	Cross void	Helical +Setback
						

Table 1. Possible modifications in three-dimensional tubes to reduce vertex shedding effect.

Meaning that they are the safest in terms of habitability and design safety. This was echoed with even better results for the models with extra-helical angles. Setbacks produced the minimal wind pressures because of reduced surface area with height; however, they experienced larger excitations of spectral wind speed than the original basic square form. Rendering it with worst expected habitability. This means that aerodynamic modifications can generally improve or eliminate vertex-shedding excitations.

## 1.2. Occupant's perception to wind induced vibrations

Undoubtedly that vibrations to structures would produce uncomfortable sensations to occupants especially in the highest floor due to more excessive vibrations. However, people perceive motion quiet comfortably, but it is the rate of motion (i.e., accelerations) that causes uneasy or discomfort. Therefore, vibrations are normally expressed as fractions of acceleration due to gravity in the form of (milli-g). Human perception to vibration is a complex sensation that encompass subjective and objective factors. The former is dealing with issues that may be subject to individual's age, culture, experience and so forth, while the latter is well-established physical phenomena that is measured, determined and occur with consensus among humans.

To give some indication what certain levels of "milli-g" actually mean for a human being (i.e., Objectively), the following extract from a monograph on wind-induced motion of tall buildings, published by the American Society of Civil Engineers [9], is provided:

5 milli-g: perceptible to some occupants but, provided that such building motion does not occur frequently or continuously for an extended period of time, unlikely to cause significant adverse occupant response or alarm;

10 milli-g: perceptible to the vast majority of occupants;

35–40 milli-g: a fear and safety threshold, sufficiently severe enough to cause some occupants to lose balance;

Occupant's response (i.e., subjectively) to wind vibrations come in different symptoms grading according to the severity of the motion – from concern, anxiety, fear, vertigo, dizziness, headaches and nausea. Some of these symptoms are often enhanced by the presence of audio stimulus, such as, wind noises, creaking noises due to building sway and/or visual stimulus, which is particularly relevant in the case of a tall building exhibiting highly three-dimensional modes of vibration.

It should also be noted that perceptibility of wind-induced motion is inversely proportional to the square root of the product of mass, stiffness and damping; this means that, in order to halve the perceptibility, the "mass × stiffness × damping" quantity needs to be increased by a factor of 4.

$$\text{perceptibility} = \frac{1}{\sqrt{(\text{mass}) \times (\text{stiffness}) \times (\text{dampness})}} \quad (2)$$

## 1.3. Habitability in some international building codes

In 2004 the Architectural Institute of Japan (AIJ), produced a guideline to the levels of wind-induced accelerations that is relating to the natural frequencies of buildings. Focusing on 1 year

return period (i.e., the maximum acceleration for a structure that can happen in a single year). The process involves determining buildings spectral response for a year and plotting it into a graph of a relationship between building's natural frequencies and acceleration. The position of the building's plotted response will determine the percentage of people who would be affected by the ensued acceleration. **Figure 7**, depicts the graph from the AIJ.

The graph lines in **Figure 7** denotes 5-levels of percentages of people perceiving the acceleration effect. (i.e., AIJ H-10, H-30, H-50, H-70, H-90) were the number denotes the percentage of people perceived the effect. The higher the plotted position of a building's response on **Figure 7**, the worse is peoples experience inside it.

Following the AIJ recommendations, back in 2007, the International Organization for Standardization (ISO) published a set of guidelines, which have now become the most widely adopted criteria for habitability design internationally [ISO 10137, 2007] also in **Figure 7**. The acceleration limits (again set against a 1-year return period) vary with the natural period of the structure and they are more stringent for residential developments than for office buildings, **Figure 7**.

#### 1.4. Intrinsic damping

Intrinsic damping is the natural properties of building materials and construction processes of withstanding wind effects without extra-means or supplementary damping. It is normally required for a yearly return period (the highest wind occurring within a year), however, longer periods would be favorable but very rear. The exact estimation of intrinsic damping can only be determined through actual measurements due to the many factors contributing to it. According to [8] main sources of intrinsic damping are:

- Material damping;
- Friction between members and connections;
- Structural system and joint types;
- Foundation and soil types (soil-structure interaction);
- Interior partitions;
- Exterior cladding;
- Other nonstructural members;
- Vibration amplitude.

Many completed buildings are been monitored globally trying to establish intrinsic damping magnitudes under wind service periods (yearly, 10-year, 50-year...).

##### 1.4.1. Wind deflection criteria

Wind deflection in buildings is due to both the drag and oscillations wind forces. Is it very limited to negligible in low-buildings. However, in tall buildings, it is dependent on the type



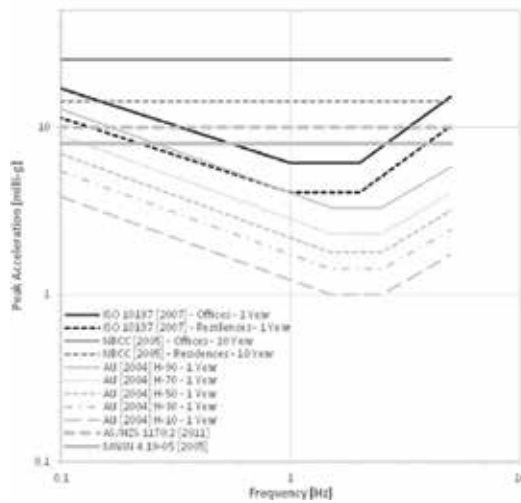


**Figure 7.** Comparison of average perception thresholds (where not indicated the return period is not specified by the relative code).

of building’s structures and the wind forces applied to it. With outrigger systems, diagrid, bundle tubes having the most stable and least deflection while, framed systems having the highest deflections due to wind.(details of these systems is outside the scope of this publication).

We can generally measure two types of deflections due to wind in buildings. Overall deflection over the whole height of the building, which recommended being in the region of H/500 to H/300, Smith [9]. This normally perceived in the acceleration and habitability of buildings. The second is in plane or story deflection to individual units like doors, windows, cladding and similar systems from normal vertical and often affects the services, operations as well as soundness within buildings. With greater deflection of this type, building components like doors windows, etc. may lose operation and stick in frames.

For example, if we consider a 200 m residential tall building with a natural frequency of 0.25 Hz exhibiting a total building drift of 0.35 m under 50-year return period winds, this would meet the widely used H / 500 limit. If the corresponding total drift under 10-year return period winds is, say, 0.25 m and assuming that 50% of this is governed by dynamic behavior (i.e., vertex shedding) - which, in the across-wind direction, is not untypical – then the resulting wind-induced peak acceleration would move toward a rather undesirable 30 milli-g ( $50\% \times 0.25 \text{ m} \times [2 \times \pi \times 0.25 \text{ Hz}]^2$ ).

## 2. Wind induced vibrations in wind turbines

Wind turbines come in different shapes and sizes, but they all convert wind power into electricity by converting wind motion into a mechanical movement and eventually into electricity. The conversion into mechanical movement can be partly converted into vibrations that

reduces the efficiency of conversion to electricity. Besides, generating noise as well as faults due to vibrations.

With modeling of vibrations the failure of key components such as tower post, drive train, gear and blades can be greatly reduced if not eliminated. The main causes to vibrations can be varied according to each particular part of the turbine, however, almost all causes are due to aerodynamic behavior. Yet till different components have different types of vibrations and vibration causes. Tower's vibration, for instance, has a low frequency magnitude from 0 to 200 Hz, while the gear and drive train have high frequency (3–20 kHz). We can distinguish between these cases for the different components as follows:

**Tower Post:** the main support of the turbine, which is normally towering high to capture more wind speed. Its geometrical uniform cross section can cause considerable aerodynamic vibrations in the same manner discussed in point 1.1 and subsection above. It worth mentioning here that tall buildings can function as supports to wind turbines in the same manner.

**Turbine blade:** Turbine blades can cause vibrations in the turbine, associated gear and tower post if they or anyone of them has different pitch angles. This will cause unsteady rotational angular speed. Vibrations may be sever in above rated wind speeds (normally 12 m/s and above). According to Peng Guo and David Infield [10], "increasing the blade pitch angle beyond stall point may lead to aerodynamic lift coefficient decreases and the drag coefficient increases leading to increased thrust causing tower to deflect and vibrations to increase."

Because of the strong connectivity of the different parts together it may be difficult from start to distinguish the source of vibration in wind turbines. Not even with close monitoring, therefore, Peng Guo and David Infield [10] proposed a simulation depending on nonlinear state estimation technique NSET whereby it would be easily to compare turbine vibrations, wind speed, angle of blade, power generated and torque at normal and specific time steps. This will relate the positions of the blade pitch of the turbine, the conditions of the wind speed with the ensued aerodynamic response of power generation, stalling or vibrations. Therefore, potentially identifying the cause of vibration. NSET would also predict the magnitude of these vectors in a given timeframe, when comparing the prediction to the normally monitored data, any discrepancies may indicate a possible cause of failure including vibrations. However, NEST involves a mathematical modeling of the parameters simulated (i.e., turbine vibrations, wind speed, angle of blade, power generated and torque) and establish its validity to the actually recorded values from active monitoring beforehand. Only when the validity of the simulation is established the comparison process may take place. This process has not been used on many cases so its validity at large is not that solid. In addition to having, to distinguish between different operational modes (i.e., below rated wind speeds or above rated wind speeds); would mean making a simulation for each mode separately to be able to compare the results.

### 3. Wind turbines integration in tall buildings

The integration of wind turbine technologies in tall buildings poses great potential to harness the resources, which is abundant around tall buildings. This can be either on the top or



**Figure 8.** Wind turbines integration in tall buildings.

along the sides of buildings. Buildings can in fact provide the structural support as well as the continuous and sustained flow of wind needed to generate the required power, Elbakheit [11]. The acceptable process involves further optimization to tall buildings aerodynamic form as well as buildings structural loadings. Adding wind turbines to buildings (especially tall buildings) or existing buildings after construction may render the structure under vortex shedding effect, as it will change totally the aerodynamic response of the building as well as the resulting wind speeds around buildings.

Nevertheless, there are many models of wind turbines that are more quiet with less vibration such as Vertical axis wind turbines that can be integrated with tall buildings with little drawbacks. In addition, using a number of small capacity wind turbines of less than 100 kW would break wind aerodynamic forces into small manageable portions compared with the option of using large turbines of over 100 kW. This also reduce the burden of maintenance and provide backup should any single turbine fails. **Figure 8.**

#### **4. Conclusions**

A high level of vibration control is achievable with the right aerodynamic design solutions in buildings, wind turbines and any industry establishments.

Vertex shedding is an aerodynamic phenomenon that triggers oscillations and vibrations in various fields of construction as well as industries. Symmetrical plans' cross-sectional configurations are the most susceptible to wind induced vibrations.

Introducing transformations in plans, horizontally and vertically is the key to control wind-induced vibrations in both buildings and various industry establishments. Corner modification, fins, torsional or spiral additions are among the favorable solutions in chimneystacks, undersea cables and similar structures.

Three-dimensional form modifications are the more efficient solutions for tall building structures.

Corner cut and helical and spiral plan modifications in various angles and configurations can considerably reduce or eliminate the vertex shedding effect in tall buildings. Setbacks, although it is a form of three-dimensional plan modification, yet due to the reduced mass at the top of tall buildings might trigger vibrations more severe than the standard uniform plans.

The recommended limit for wind vibrations or oscillations for a structure is in the range of  $H/300$  to  $H/500$  were,  $H$  is the height of the buildings.

Human perception to vibration varies and depends on acceleration (rate of motion) related to gravity acceleration  $g$ . Alarming vibrations occurs above 30 milli- $g$ .

Tall buildings provide a promising building type for wind energy integration. Furthermore, the addition of wind turbines into building either new or retrofitting can render the building under vertex shedding. Exercise extreme caution to optimize wind flows around buildings to enhance power generation as well as to avoid vertex shedding.

Wind Vibrations in wind turbine caused either by turbine tower cross-sectional symmetry and/or by, the unbalanced pitch angles of turbine blades. Therefore, checking turbine blade angles first would assures of turbine's stability, if vibration still exists, then it will be the symmetrical cross section of the supporting post.

Further aerodynamic optimizations research in tall buildings' 3-dimensional configuration and/or aerofoils for integration of sizable small-scale wind-harnessing technologies can add to the safety, habitability of tall buildings with renewable energy at hand.

## **Acknowledgements**

The author would like to express his appreciation to the Deanship of Scientific Research at King Saud University for the provision of funding through the College of Architecture and Planning Research Center.

## **Author details**

Abdel Rahman Elbakheit

Address all correspondence to: [abdel.elbakheit@hotmail.com](mailto:abdel.elbakheit@hotmail.com)

Department of Architecture and Building Science, King Saud University, Riyadh, Saudi Arabia

## References

- [1] Kawada T, Scott R. History of the Modern Suspension Bridge : Solving the Dilemma between Economy and Stiffness. 2010
- [2] Gurley KR, Tognarelli MA, Kareem A. Analysis and simulation tools for wind engineering. *Probabilist Eng Mech.* 1997;**12**(1):9-31
- [3] Li T, Zhang JY, Zhang WH, Zhu MH. Vortex-induced vibration characteristics of an elastic circular cylinder. *World Academy of Science, Engineering and Technology.* 2009
- [4] Mooneghi MA, Kargarmoakhar R. Aerodynamic mitigation and shape optimization of buildings: Review. *J Build Eng.* 2016;**6**:225-235
- [5] Quan Ga. Study on wind loads and responses of tall buildings and structures. The Seventh Asia-Pacific Conference on Wind Engineering; November 8-12, 2009; Taipei, Taiwan; 2004
- [6] Irwin PA. Bluff body aerodynamics in wind engineering. *Journal of Wind Engineering and Industrial Aerodynamics.* 2008;**96**(6-7):701-712
- [7] Irwin P, Kilpatrick J, Robinson J, Frisque A. Wind and tall buildings: Negatives and positives. *Structural Design of Tall and Special Buildings.* 2008;**17**(5):915-928
- [8] Aerodynamic and flow characteristics of tall buildings with various unconventional configurations. *International High-Rise Building Journal.* 2013;**2**(3)
- [9] Smith MA, Caracoglia L. A Monte Carlo based method for the dynamic “fragility analysis” of tall buildings under turbulent wind loading. *Engineering Structures.* 2011;**33**(2): 410-420
- [10] Infield PGD. Wind turbine tower vibration modelling and monitoring by the nonlinear state estimation technique (NSET). *Energies.* 2012:5279-5293
- [11] Elbakheit AR. Factors enhancing aerofoil wings for wind energy harnessing in buildings. *Building Services Engineering Research & Technology.* 2014;**35**(4):417-437



---

# State Feedback Nonlinear Control Strategy for Wind Turbine System Driven by Permanent Magnet Synchronous Generator for Maximum Power Extraction and Power Factor Correction

---

Yasser Boussairi, Abdelmajid Abouloifa,  
Ibtissam Lachkar, Chaouqi Aouadi and  
Abdelatif Hamdoun

Additional information is available at the end of the chapter

<http://dx.doi.org/10.5772/intechopen.72366>

---

## Abstract

This chapter addresses the problem of controlling the Complete chain of the wind turbine system using the permanent magnet synchronous generator (PMSG) connected with the Distribution network via an AC/DC/AC converters through LCL filter, the control to be applied in different parts of the system, whose objectives are three: (1) adjust the generator speed to track a varying reference signal; (2) the control of the network-side converter must be maintained the current injected into the network in a unit power factor correction (PFC); (3) regulating the DC Link voltage at a constant value. Firstly, the mathematical modeling for all system components studied in d-q frame and its state space equation are established to simplify the proposed control, thereafter a nonlinear backstepping approach is used in this work to achieve the objectives indicated above. The performance of the proposed approach is evaluated based on the various simulations results carried out under Matlab/Simulink/Simpower software.

**Keywords:** wind energy, PMSG, AC/DC/AC converter, LCL filter, nonlinear control, backstepping approach, PFC

---

## 1. General introduction

Nowadays, the demand for electrical energy continues to increase, as the intense industrialization of the last decades and the multiplication of electric household appliances has led to considerable electrical energy needs. The various traditional power stations use fossil fuels (coal, oil, natural gas, etc.) and, consequently, development, fissile sources (nuclear energy) such as uranium, hydrocarbons and Water, thermal power plants are responsible for releases of atmospheric gases. Nuclear energy has an undeniable advantage of not causing pollution, but the risk of a nuclear accident remains, and which increases over the years like the storage of non-repeatable nuclear waste. The treatment and burial of waste are real problems that make this energy unattractive for future generations [1].

All these disadvantages have prompted researchers to reduce their exploitation to solve their problems, using the so-called “renewable” energies (wind and solar). The latter are perfectly in line with the overall effort to reduce CO<sub>2</sub> emissions. Wind power is clearly in the forefront. This energy is transformed into mechanical energy by wind turbines and then converted to electrical energy by generators [2]. Therefore, there are different wind turbine configurations installed in large scale; The major distinction among them is made between generator synchronous or asynchronous [3].

After having transformed wind energy into electrical energy, it is necessary to adapt it to the load it is feeding or the network to which our production system is connected, since the wind turbines considered as generator of variable power. Where the voltage supplied by the generator undergoes variations due to fluctuations in the speed of rotation thereof as a function of the wind speed. This results in a variation in the electrical power supplied to the load supplied. Moreover, the shape and frequency of the supplied voltage are not necessarily adapted to the load. To solve these problems, it is necessary to use power electronics via a generator-side rectifier and a network-side inverter, new control approaches are learned to optimize this generation of energy.

In this chapter, we use the permanent magnet synchronous generator (PMSG) a variable speed, which found a particular interest in applications of wind energy, because have many advantages such are considered stable, their small size and high energy efficiency, ability of operation at slow speed and they do not need a gearbox [4, 5]. The last years have seen rapid progress in the control of nonlinear systems related to renewable energies. This system has been treated using several control strategies ranging from simple techniques, for example so-called oriented flow control (FOC) [6], to more sophisticated nonlinear approaches, which poses a major problem which is the need to use a mechanical sensor (speed, load torque). This imposes an additional cost and increases the complexity of the assemblies, for example, feedback linearization [7], hybrid mode/slip/neuro fuzzy control [8], the direct control of the couple (DTC) [9].

In nonlinear control or having non-constant parameters systems, conventional control laws may be inadequate because they are not strong especially when the demands on accuracy and other dynamic characteristics of systems. We must appeal to non-sensitive control laws to changes in parameters, to disturbance and nonlinearities, On the other hand.



In this chapter, we present a technique to control two power converters which is based on the backstepping approach, it Draws the attention of many researchers in the field of control of electrical machines [10–13]. The importance of backstepping controllers lies in: the high accuracy, fast dynamic response, stability, simplicity of design and implementation, and vis-à-vis robustness changes in internal or external parameters [14]. The rest of this paper is organized as follows. In Section 2 the mathematical model detailed and the state space of the system studies are presented, and the control proposed based on the technical backstepping for the whole system are presented in Section 3. Section 4 present the simulation example in the platform MATLAB/Simulink/Simpowers, we end this chapter with a conclusion.

## 2. Modeling of the wind system based on a synchronous generator

In the second part of this chapter we have proposed the concept of a complete wind chain. In this part, we establish a mathematical model of the whole wind chain by insisting in particular on the Multiphysics character (taking into account the mechanical, magnetic, electrical phenomena)

The modeling of the wind turbine requires the modeling of the electric generator, the power converter and the filter of the control system [15]. This section divided into two parts:

- The first part is devoted to the modeling of the permanent magnet synchronous machine associated with the rectifier
- In the second part, we present the modeling of the converter on the network side (inverter); connected to the grid via an LCL filter show by **Figure 1**.

### 2.1. AC/DC rectifier-generator modeling

The control of an electric motor is a difficult task and requires, above all, a good knowledge of its dynamic model.

This part will consist in describing the machine mathematically with its nonlinear model by putting some working hypotheses in evidence [16, 17], which allowed the study of behavior of the latter. The model adopted is based on the transformation of PARK.

Expressed in the d-q coordinates, are given the following state space form:

$$\frac{d\omega}{dt} = \left( \frac{(L_d - L_q)}{j} i_d + \frac{p\phi_f}{j} \right) i_q - \frac{f}{j} \omega - \frac{1}{J} T_l \quad (1)$$

$$\frac{di_q}{dt} = -\frac{R_s}{L_q} i_q - p \frac{L_d}{L_q} \omega i_d - p \frac{1}{L_q} \phi_f \omega + \frac{1}{L_q} v_q \quad (2)$$

$$\frac{di_d}{dt} = -\frac{R_s}{L_d} i_d + p \frac{L_d}{L_q} \omega i_q + \frac{1}{L_d} v_d \quad (3)$$

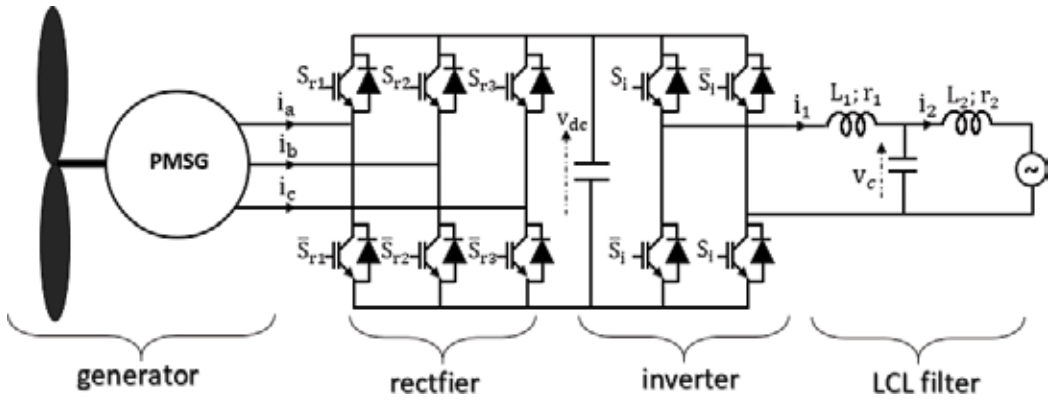


Figure 1. Architecture of AC/DC/AC power converter in wind power system.

where  $R_s$  is the resistance of the stator windings,  $(L_d, L_q)$  are d and q axis inductances,  $(i_d, i_q)$  are the dq components of the stator current,  $\varphi_f$  amplitude of the flux induced by the permanent magnets of the rotor in the stator phases,  $p$  number of pole pairs,  $j$  combined inertia of rotor and load,  $T_l$  shaft mechanical torque,  $f$  combined viscous friction of rotor and load,  $\omega$  angular velocity of the rotor  $(v_d, v_q)$  denote the averaged stator voltage in dq- coordinate (Parks transformation of the triphase stator voltages) these voltages are expressed in function of the corresponding control action:

$$v_q = v_{dc}u_1; \quad v_d = v_{dc}u_2 \quad (4)$$

## 2.2. DC/AC inverter-grid modeling

The supply network is connected to a single-phase inverter consisting of four semiconductors (IGBT with antiparallel diodes for bidirectional current mode) displayed in two branches. A single switch on the same leg can be conductive at the same time, this converter connecting with the network through an LCL filter, the latter they minimize the amount of current distortion injected into the utility grid [18, 19]. Applying Kirchoff's laws, this subsystem is described by the following set of differential equations:

$$\frac{di_2}{dt} = \frac{1}{L_2}(-r_2i_2 + v_c - v_r) \quad (5)$$

$$\frac{dv_c}{dt} = \frac{1}{C}(i_1 - i_2) \quad (6)$$

$$\frac{di_1}{dt} = \frac{1}{L_1}(-r_1i_1 + v_{dc} - v_c) \quad (7)$$

where  $L_1$  and  $L_2$  are the self-inductances,  $r_1$  and  $r_2$  are its parasitic resistances,  $(i_1, i_2)$  are the components of the current flowing the inductors  $L_1$  and  $L_2$  respectively.  $(v_c, v_r, v_o)$  are the

voltages across the capacitor, in the grid side and in the output of inverter respectively. The inverter undergoes the equations:

$$v_o = v_{dc}u \tag{8}$$

Elaborate partial model uses binary control signals, to develop the control laws, and it will be based on the average model in which each variable is replaced by its average value over a switching period.

Now, let us introduce the following notation:

$$\omega = x_1; i_q = x_2; i_d = x_3; i_2 = x_4; v_c = x_5; i_1 = x_6$$

where  $x$  represents an averaging value over a cutting period of a real signal.

The state space equations obtained up to now are put together to get a state space model of the whole system including the AC/DC/AC converters combined with the synchronous generator. The whole model is rewritten here by:

$$\dot{x}_1 = \left( \frac{(L_d - L_q)}{j} x_3 + \frac{p\phi_f}{j} \right) x_2 - \frac{f}{j} x_1 - \frac{1}{J} T_l \tag{9}$$

$$\dot{x}_2 = -\frac{R_s}{L_q} x_2 - p \frac{L_d}{L_q} x_1 x_3 - p \frac{1}{L_q} \phi_f x_1 + \frac{1}{L_q} v_{dc} u_1 \tag{10}$$

$$\dot{x}_3 = -\frac{R_s}{L_d} x_3 + p \frac{L_d}{L_q} x_1 x_2 + \frac{1}{L_d} v_{dc} u_2 \tag{11}$$

$$\dot{x}_4 = \frac{1}{L_2} (-r_2 x_4 + x_5 - v_r) \tag{12}$$

$$\dot{x}_5 = \frac{1}{C} (x_6 - x_4) \tag{13}$$

$$\dot{x}_6 = \frac{1}{L_1} (-r_2 x_6 + v_{dc} u - x_6) \tag{14}$$

### 3. Nonlinear controller design

The main challenge of our research work is to design a control law for the permanent magnet synchronous generator, which is more powerful for monitoring control, disturbance rejection, stability, parametric uncertainties of robustness, compliance with constraints Physics and computation time, while maintaining the nonlinear aspect [20].

Since a few years, many evolutions have been made within the framework of the control of the nonlinear systems whose backstepping technique forms part. The backstepping approach is a systematic and recursive methodology for the synthesis of nonlinear control laws, the basic idea of backstepping control is to make the system looped, equivalent to cascaded order one subsystems Stable in the Lyapunov sense, which gives it robust qualities and an asymptotic

global stability of the tracking error. For each subsystem, a so-called virtual control law is calculated, in order to ensure the convergence of the first-order subsystems characterizing the continuation of trajectories toward their equilibrium states (tracking errors are zero). The determination of the control laws that flows from this approach is based on the use of Lyapunov functions [14]

From the point of view of control, this is expressed in the following three objectives:

- i. Speed control: forces the speed of the generator to follow a reference signal varies.
- ii. PFC: the current injected into the network must be sinusoidal and in phase with the AC supply voltage.
- iii. Check the voltage of the DC bus at a given reference. This is usually set to a constant value equal to the nominal input voltage of the drive.

The control to be applied in different parts of the system. The generator-side converter is mainly used to control the speed of the generator to extract the maximum output power at different wind speeds [16, 18], the mains-side converter is mainly used to control reactive power on the one hand and Maintain the voltage In the DC bus capacitor of the constant value and make the current output of the inverter in phase with the gate voltage.

A nonlinear recoil control design scheme is developed for PMSG speed tracking control.

### 3.1. Generator speed control

The system includes a fast mode (electrical currents) and a slow (mechanical) mode. The adopted control strategy uses cascaded loops, two internal loops to control the currents of the d and q axes, and an external loop to control the speed of the generator, in order to guarantee satisfactory speed reference tracking quality despite [21]. The uncertainties of the generator parameters. In this sense, we go through three steps, as shown in **Figure 2**. In each step, we calculate the associated error and we ensure the stability of the system by choosing the good function of Lyapunov in order to find the commands.

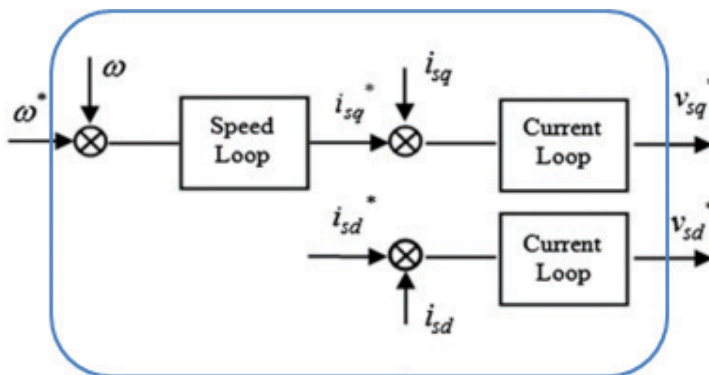


**Figure 2.** Rotor-side converter control system.

Usually the current of the d-axis must be set to zero in order to keep the flow constant in the air gap of the machine [22]. The current of the q-axis must follow a reference signal of the external speed loop [23].

In order, the PMSG speed is used as a reference value for a controller to capture the maximum power of the incident energy of the wind turbine.

### 3.1.1. Step 1: calculation of the virtual control law $i_{qref}$

To solve the speed monitoring problem, the velocity control error and its path designated by the reference value are defined:

$$e_1 = x_1 - x_1^{ref} \tag{15}$$

Let a virtual input  $x$  used to ensure the stability of the speed loop, the dynamics of the speed control error is given by:

$$\dot{e}_1 = \dot{x} - \dot{x}_1^{ref} \qquad \dot{e}_1 = \left( \frac{(L_d - L_q)}{j} x_3 + \frac{p\phi_f}{j} \right) x_2 - \frac{f}{j} \Omega - \frac{1}{j} T_l - \dot{x}_1^{ref} \tag{16}$$

The asymptotic stability of the resulting closed loop system is guaranteed according to Lyapunov stability theorem. To the speed of tracking error goes to zero, the Lyapunov function is constructed for the subsystem is given by:

$$V_1 = \frac{1}{2} e_1^2 \tag{17}$$

If this function is always positive (it is the case now) and its derivative is always negative, the error will be stable and tends to zero.

The derivative of the function is written as follows:

$$\dot{V}_1 = e_1 \dot{e}_1 \tag{18}$$

For the derivative of the test to be still negative, it must take the derivative of the form:

$$\dot{V}_1 = -k_1 e_1 \tag{19}$$

Where  $k_1 > 0$  is a positive control parameter introduced by the backstepping method, which must always be positive and non-zero in order to satisfy the stability criteria of the Lyapunov function. In addition, this parameter influences the dynamics of the control. By following the backstepping method, a virtual command  $x_2$  used to ensure the stability of the velocity loop is given by the following equation:

$$x_2 = \frac{j}{p(L_d - L_q) x_3 + p\phi_f} \left( +\frac{f}{j} x_1 + \frac{1}{j} T_l + x_1^{ref} - k_1 e_1 \right) \tag{20}$$

Once the virtual input  $x_1$  defined in the first loop to stabilize the dynamics of (13), we define the second error on the current as follows:

$$e_2 = x_2 - x_2^{ref} \quad (21)$$

### 3.1.2. Step 2: calculation of the final control law $u_1$

This step makes it possible to determine the control law  $u_1$  of the global system

Using Eq. (21), the temporal derivatives given by:

$$\dot{e}_2 = \dot{x}_2 - \dot{x}_2^{ref} \quad \dot{e}_2 = -\frac{R_s}{L_q}x_2 - p\frac{L_d}{L_q}x_1x_3 - p\frac{1}{L_q}\phi_f x_1 + \frac{1}{L_q}v_{dc}u_1 - \dot{x}_2^{ref} \quad (22)$$

In order to ensure the convergence of the tracking error to zero, also requires that the current be regulated and limited, we use the extension of the following Lyapunov function:

$$V_2 = V_1 + \frac{1}{2}e_2^2 \quad (23)$$

Its temporal derivative is given by the following equation:

$$\dot{V}_2 = \dot{V}_1 + e_2\dot{e}_2 \quad (24)$$

Finally, in order to make  $\dot{V}_2$  negative, the voltage control input of the q-axis can be found by choosing  $\dot{V}_2$  by the following equation:

$$\dot{V}_2 = -k_2e_2^2 \quad (25)$$

Where  $k_2$  0 is a design constant.

We deduce the law of final control:

$$u_1 = \frac{L_q}{v_{dc}} \left[ \begin{array}{l} -k_2e_2 - \frac{p}{j} \left( (L_d - L_q)x_3 + \phi_f \right) e_1 + \\ \frac{R_s}{L_q}x_2 + p\frac{L_d}{L_q}x_1x_3 - p\frac{1}{L_q}\phi_f x_1 + \dot{x}_2^{ref} \end{array} \right] \quad (26)$$

### 3.1.3. Step 3: calculating the control law $u_2$

This stage interests us to stabilize the subsystem (11) which aims to force the current  $i_d$  is equal to 0.

The current tracking error:

$$e_3 = x_3 - x_3^{ref} \quad (27)$$

Its temporal derivative is given by the following equation:

$$\dot{e}_3 = -\frac{R_s}{L_d}x_3 + p\frac{L_d}{L_q}x_1x_2 + \frac{1}{L_d}v_{dc}u_2 - \dot{x}_3^{ref} \quad (28)$$

The third function of Lyapunov is selected so that:

$$V_3 = \frac{1}{2}e_3^2 \quad (29)$$

So that the derivative of the criterion is always negative, the derivative of V1 must take the form  $\dot{V}_3 = -k_3e_3^2$  introduced by the backstepping method,

$$\dot{V}_3 = e_3 \left( -\frac{R_s}{L_d}x_3 + p\frac{L_d}{L_q}x_1x_2 + \frac{1}{L_d}v_{dc}u_2 - \dot{x}_3^{ref} \right) = -k_3e_3^2 \quad (30)$$

Using (28)–(30), the control law is given by:

$$u_2 = \frac{L_d}{v_{dc}} \left[ \frac{R_s}{L_d}x_3 - p\frac{L_d}{L_q}x_1x_2 + \dot{x}_3^{ref} - k_3e_3 \right] \quad (31)$$

### 3.2. DC/AC inverter-grid control design

Our goal is to inject active energy into the network while maintaining a very good power factor (PFC). This means that the three-phase system absorbed by the converter should be sinusoidal and in phase with the supply mains voltage [18]. We are therefore looking for a regulator that forces the current to follow a reference signal of the form. For the moment, the quantity is any real positive. The controller will now be designed by applying the backstepping control technique to the system of Eqs. (12)–(14); The synthesis ends in three stages since the relative degree of the system is equal to three when the output considered is the current.

#### 3.2.1. Step 4: stabilization of subsystem (12)

Let us introduce the following error on the current:

$$e_4 = L_2(x_4 - x_4^{ref}) \quad (32)$$

With  $x_4^{ref} = i_{2ref}$  the reference of the signal

Given the Eq. (12) of the whole model, the dynamics of the error can be written as follows:

$$\dot{e}_4 = -r_2x_4 + x_5 - v_r - L_2\dot{x}_4^{ref} \quad (33)$$

Suppose that  $x_5$  is the virtual control input used to ensure the overall asymptotic stability of the current loop, taking Lyapunov’s candidate function as:

$$V_4 = \frac{1}{2}e_4^2 \quad (34)$$

The derivative of this equation gives:

$$\dot{V}_4 = e_4\dot{e}_4 \quad (35)$$

A judicious choice of  $x_5$  and rendering  $V_4$  negative definitive and providing stability for the dynamics of  $e_4$  is  $x_5 = x_5^{ref}$  such that:

$$V_4 = -k_4e_4^2 \quad (36)$$

By following the backstepping method and to ensure a continuous stability voltage, the virtual control  $x_5$  is given by the following equation:

$$x_5 = r_2x_4 + v_r + L_2\dot{x}_4^{ref} - k_4e_4 \quad (37)$$

Since  $x_5$  is not the actual control input, we define a second tracking error between the stabilization function  $x_5^{ref}$  and the virtual control input  $x_5$ .

$$e_5 = C(x_5 - x_5^{ref}) \quad (38)$$

### 3.2.2. Step 5: stabilization of subsystem (13)

The temporal derivative of  $e_5$  is given by:

$$\dot{e}_5 = x_6 - x_4 - C\dot{x}_5^{ref} \quad (39)$$

The virtual input  $x_5^{ref}$  is used to ensure the stability of the voltage loop. Then, considering the candidate for the Lyapunov function:

$$V_5 = V_4 + \frac{1}{2}e_5^2 \quad (40)$$

We obtain the derivative of (40)

$$\dot{V}_5 = -k_4e_4^2 + e_4\left(\frac{e_4}{C} + \dot{e}_5\right) \quad (41)$$

It can easily be verified that the time derivative  $\dot{V}_5$  is a negative defined function if the control input is chosen such that:

$$x_6 = x_4 + k_4e_4 + e_5\left(k_5e_5 + \frac{1}{C}e_4\right) \quad (42)$$

where  $k_5 > 0$  is a positive synthetic constant. Indeed, this choice would imply that  $e_5 = -k_5e_5$  what clearly establishes the exponential stability of the system (13)



Since  $x_6$  is not the actual control inputs, we define a third tracking error between the stabilization functions and the virtual control input the  $x_6$ .

$$e_6 = L_1(x_6 - x_6^{ref}) \tag{43}$$

### 3.2.3. Step 6: stabilization of subsystem (14)

The third design step consists in choosing the actual control signal  $u$ , so that all errors ( $e_4, e_5, e_6$ ) converge to zero. To this end, we should ensure that these errors depend on the actual control signal. We begin to focus on; It follows from (43) that:

$$\dot{e}_6 = -r_1 x_6 - x_5 + \frac{1}{v_{dc}} u - L_1 \dot{x}_6^{ref} \tag{44}$$

To analyze the error system, composed of Eqs. (43), (44), consider the candidate of the augmented Lyapunov function:

$$V_6 = V_5 + \frac{1}{2} e_6^2 \tag{45}$$

The derivative is given by:

$$\dot{V}_5 = -k_5 e_5^2 + e_5 \left( \frac{e_5}{C} + \dot{e}_6 \right) \tag{46}$$

Using (44)–(46), the control law of the system is given by:

$$u = \frac{1}{v_{dc}} \left( r_1 x_1 + x_5 + L_1 \dot{x}_6^{ref} - \frac{1}{L_1} e_5 - k_6 e_6 \right) \tag{47}$$

## 4. Simulation results and discussion

Simulation of the wind energy conversion (WEC) system the global control system described by **Figure 3** is simulated using the Matlab/Simulink (V. R2015a), operating under Windows 8. The controlled part is a wind system including the synchronous generator and the associated AC DC/AC power converters via LCL filter with the numerical values (**Figures 4** and **5**):

PMSG:  $R_s = 0.425 \Omega$ ,  $L_d = L_q = 0.0084 H$ ,  $\varphi_f = 0.433 Wb$ ,  $j = 0.02 Kg.m.m$ ,  $p = 4$

Network and filter:  $v_g = 220V$ ,  $50 Hz$ ,  $L_1 = L_2 = 5e^{-3}H$ ,  $r_1 = r_2 = 50e^{-3}\Omega$

Controller parameters:

Speed and id regulator:  $k_1 = 2e^{-2}$ ,  $k_2 = 7.2e^{-3}$ ,  $k_3 = 2e^{-2}$

PFC regulator:  $k_4 = 3e^{-4}$ ,  $k_5 = 8e^{-3}$ ,  $k_6 = 3e^{-2}$

Vdc regulator:  $k_p = 18e^{-4}$ ,  $k_i = 9e^{-5}$

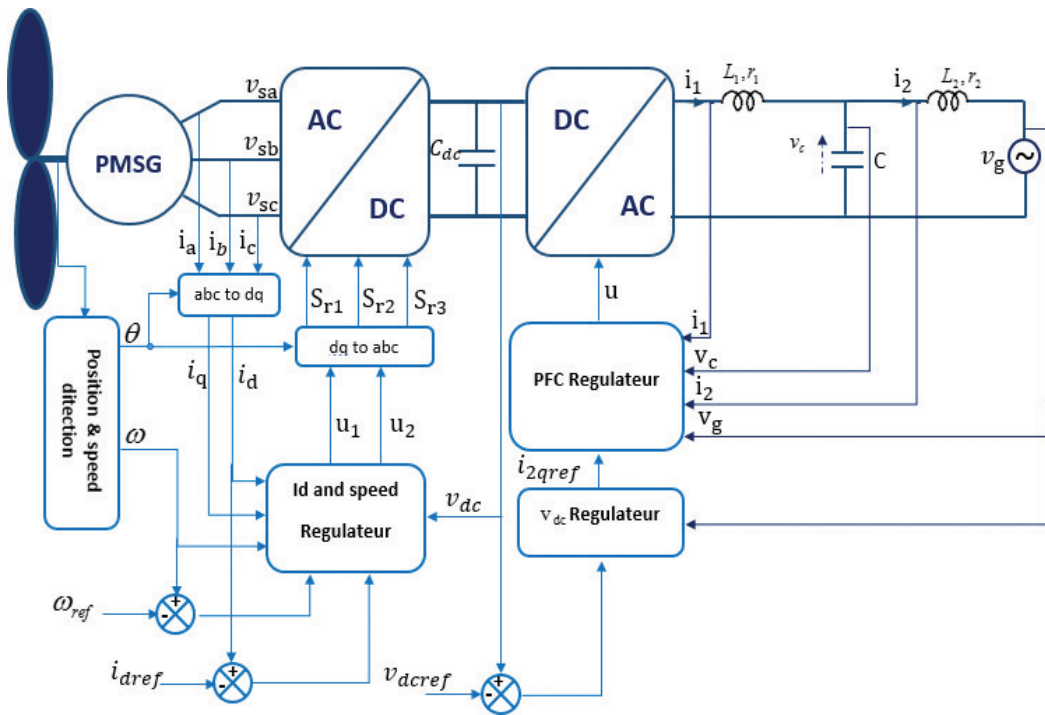


Figure 3. Block diagram of control system including the synchronous generator associated AC/DC/AC power converters.

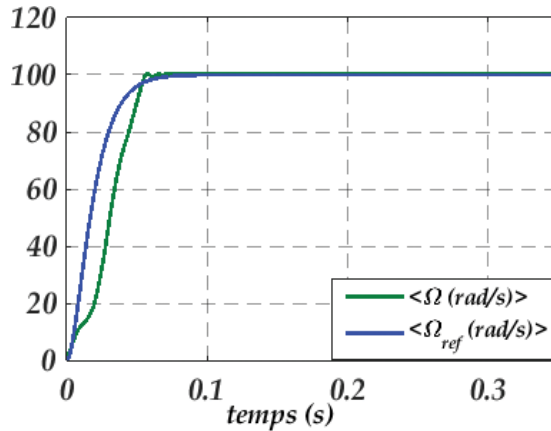
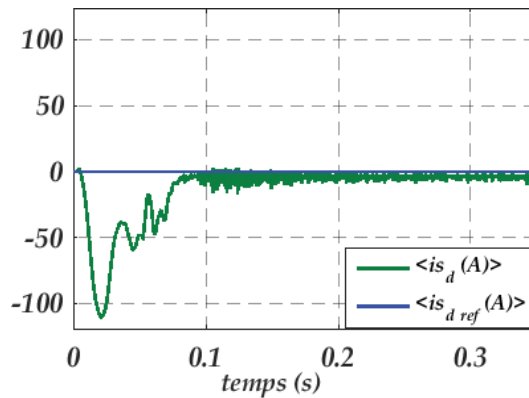
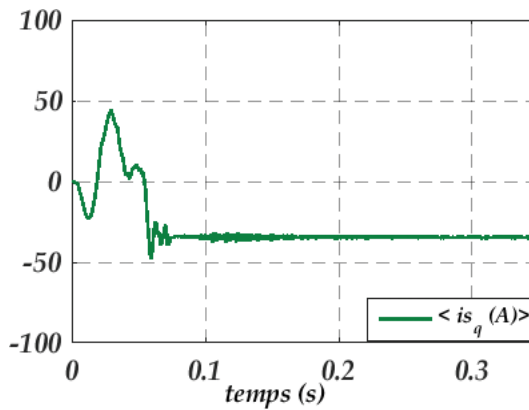


Figure 4. Figure of the rotor speed for a reference 100 (rad/s).

The speed rotation  $\omega$  of the generator does not change much value, it remains practically equal to the reference value  $\Omega_{ref}$  as shown by the appearance of the error between these two signals which is zero, the current path  $i_{sd}$  takes the value 0 set at the start, and also notice clearly in the transitional regime the speed of the system with the regulator



**Figure 5.** Figure of current  $i_{sd}$  for a reference 0.



**Figure 6.** The current along the axis  $q$ .

The rate of the current  $i_{sq}$  tends to a constant value and has the same shape as that of the torque; We deduce that the electromagnetic torque is directly proportional to the current  $i_{sq}$  shown in **Figures 6** and **7** respectively.

**Figures 8** and **9** respectively show the current  $i_2$  injected in the network and its reference obtained from the DC bus controller and the error between these two signals

**Figures 10** and **11**, respectively, show the shape of the DC bus voltage  $v_{dc}$  for a reference  $v_{dcref}$  (400 V) and the current  $i_2$  inject into the network with the supply voltage.

For this second simulation part, a random wind profile was applied in order to test the degree of continuity and efficiency of the control used in this chapter.

The above figures show the results of the command by Backstepping applied to the GSAP. The objective is to control the operation of the closed loop system by varying the first reference rotational speed of 0 rad/s at 80 rad/s and then at a final value equal to the nominal speed: 157 rad/s. **Figures 12–15**, show the simulation results obtained using the nominal parameters

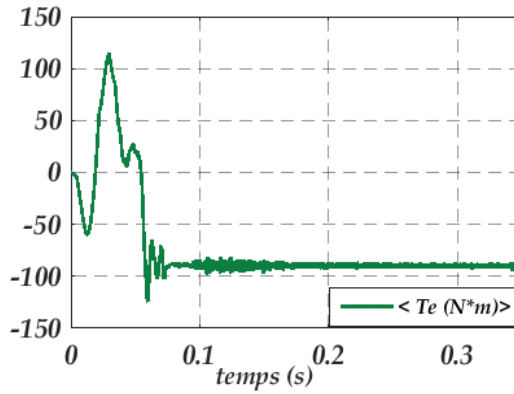


Figure 7. The electromagnetic force  $T_e$ .

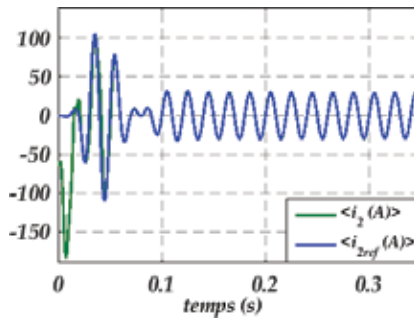


Figure 8. Flow of  $i_2$  injected into the grid.

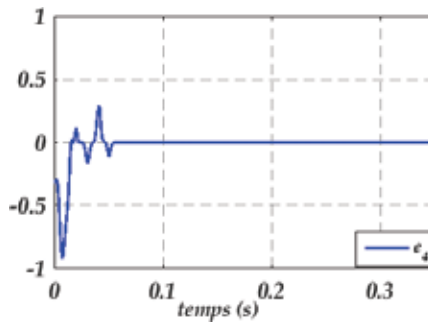


Figure 9. Error behavior between current  $i_2$  and its reference.

of the generator. These figures describe the good system performance in a closed loop in terms of trajectory tracking and disturbance rejection on multiple speeds: low and high speed. In addition, the current d-axis of good follows its reference. **Figures 16, 17,** show that the output current in phase with the power supply voltage and the DC link is stable at a constant value which is check the control objectives.

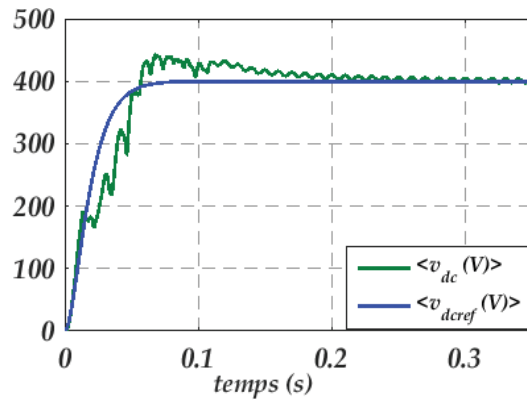


Figure 10. DC bus voltage regulation.

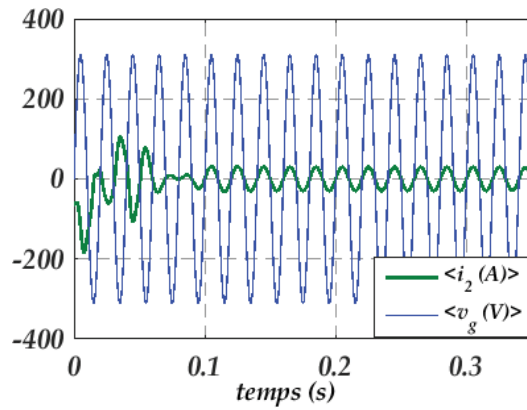


Figure 11. Current  $i_2$  and  $v_g$ .

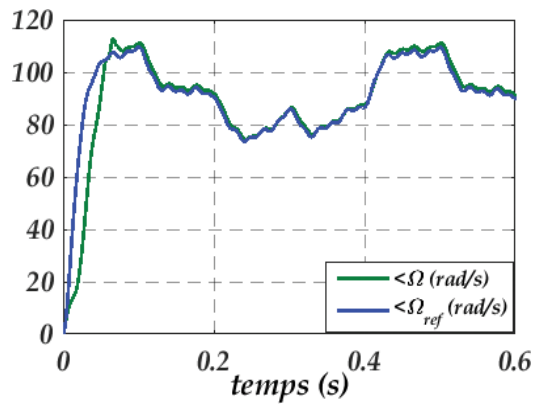


Figure 12. Figure of the rotor speed for a various reference.

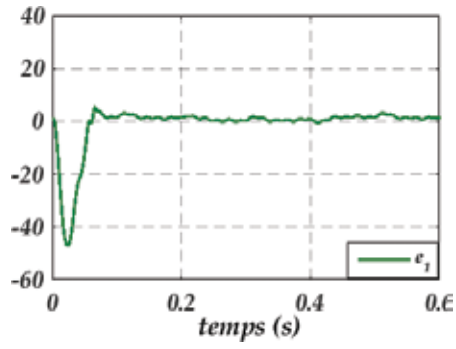


Figure 13. Error behavior between rotor speed and its reference.

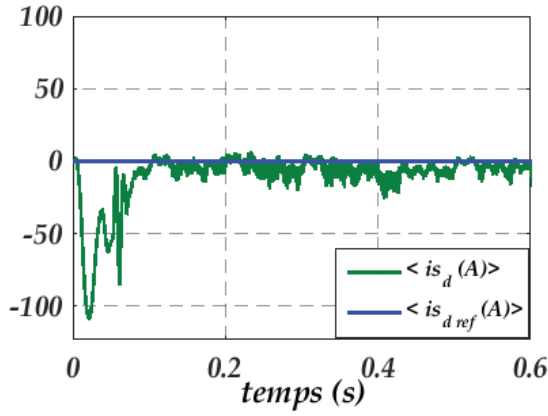


Figure 14. Current  $i_d$  and its reference.

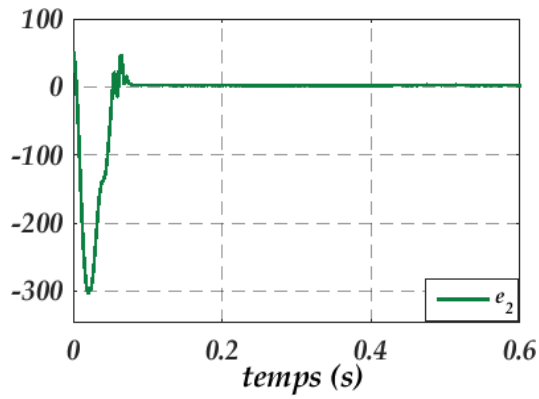


Figure 15. Error behavior between current  $i_d$  and its reference.

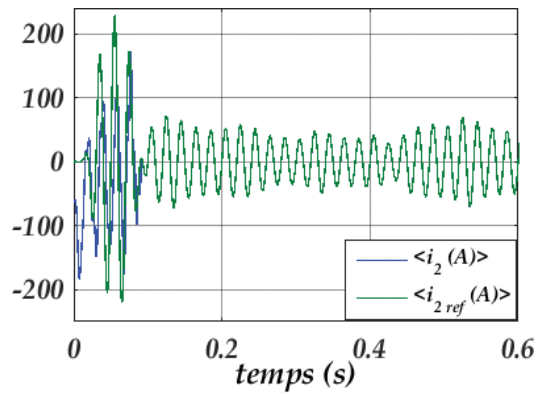


Figure 16. Current  $i_2$  injected into the grid.

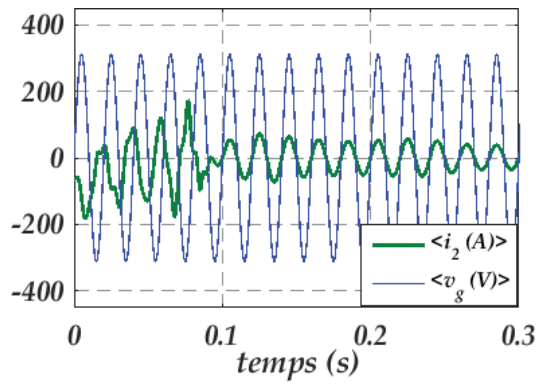


Figure 17. Current  $i_2$  and  $v_g$ .

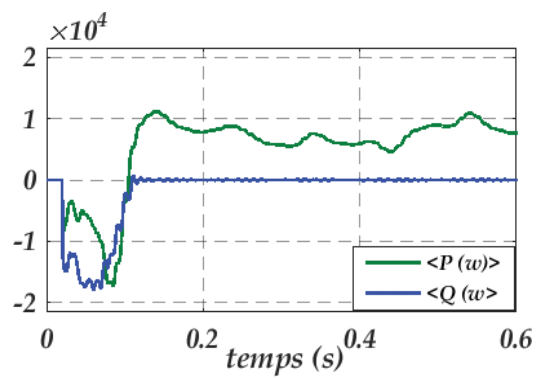


Figure 18. Active and reactive power.

The active and inverted power injected into the grid are presented at the **Figure 18**, the reactive power tends toward its reference value  $Q_{ref} = 0$ , for the active power it is observed that the variation in the speed of the machine influences the variation in power, When the speed of the generator very large the value of the active power becomes greater

#### 4.1. Interpretation of results

From the simulation results obtained, it can be noted from the first view that the regulator based on the backstepping approach has practically slightly better performances than those of the conventional regulator, especially in dynamic conditions, Where it can be observed in all the figures presented in the simulations that the response time for is very short for the signals to restore to the maximum values, so this fast correction either of the velocity or the currents or voltages translates the continuation of our system And assured the performance of our regulator

In the injection part, the power to the network it is observed that our regulator respects the characteristics of our grid that it is the frequency or the phase on the one hand, and on the other hand the power injected to the network one notes that the power Reactive voltage tends to zero and the active power reacted with the variation of the speed of the generator when the speed reaches the maximum power is totally transmitted to the network.

## 5. Conclusion

In this chapter, the nonlinear control of the wind conversion chain based on a synchronous generator with permanent magnet controlled by the electronic converters with MLI control was presented. This electrical combination enabled us to execute the control strategy designed to this wind system studied which was the extraction of the maximum power called "MPPT", also the injection of the current to the network with a good power factor at the "Using a speed control controlled by a backstepping approach. The simulation results obtained in this chapter clearly show an acceptable degree of efficiency of the chosen regulation which causes the system to return to its optimum point after a variation of the wind speed.

### Author details

Yasser Boussairi<sup>1\*</sup>, Abdelmajid Abouloifa<sup>1</sup>, Ibtissam Lachkar<sup>2</sup>, Chaouqi Aouadi<sup>1</sup> and Abdelatif Hamdoun<sup>1</sup>

\*Address all correspondence to: yasserboussairi@gmail.com

1 LTI Lab, Faculty des Sciences Ben M'sik, University Hasan II of Casablanca, Casablanca, Morocco

2 LISER Lab, ENSEM of Casablanca, University Hasan II of Casablanca, Casablanca, Morocco



## References

- [1] Bianchi FD, Mantz RJ, De Battista H. *The Wind and Wind Turbines*. London: Springer; 2007. pp. 7-28
- [2] Rolan A, Luna A, Vazquez G, Aguilar D, and Azevedo G. Modeling of a variable speed wind turbine with a permanent magnet synchronous generator. In *2009 IEEE International Symposium on Industrial Electronics*. IEEE; 2009. pp. 734-739
- [3] Yin M, Li G, Zhou M, Zhao C. Modeling of the wind turbine with a permanent magnet synchronous generator for integration. In *Power Engineering Society General Meeting, 2007*. IEEE; 2007. pp. 1-6
- [4] Belloni F, Chiumeo R, Gandolfi C, Villa A. Simulation model of a permanent magnet synchronous generator for grid studies. In *International Conference on Renewable Energies and Power Quality (ICREPQ14)*; 2014
- [5] Haque ME, Negnevitsky M, Muttaqi KM. A novel control strategy for a variable-speed wind turbine with a permanent-magnet synchronous generator. *IEEE Transactions on Industry Applications*. 2010;**46**(1):331-339
- [6] Saleh KI, Mohammed OA, Badr MA. Field oriented vector control of synchronous motors with additional field winding. *IEEE Transactions on Energy Conversion*. 2004;**19**:95-101
- [7] Yang ZP, Wang MH, Liu CL, Hou, Cai YB. Variable structure control with sliding mode for self-controlled synchronous motor drive speed regulation. *IEEE International Symposium on Industrial Electronics (ISIE)*, Vol. 2; 1992. pp. 620-624
- [8] Elmas C, Ustun O. A hybrid controller for the speed control of a permanent magnet synchronous motor drive. *Control Engineering Practice*. 2008;**16**(3):260-270
- [9] Pyrhonen O, Niemela M, Pyrhonen J, and Kaukonen J. Excitation control of DTC controlled salient pole synchronous motor in field weakening range. *International Workshop on Advanced Motion Control, AMC '98, Coimbra*; 1998. pp. 294-298
- [10] Camara MMS, Camara MB, et al. Modélisation et commande d'une génératrice synchrone à aimant permanent pour la production et l'injection des énergies offshores dans un réseau. In *Symposium de Génie Electrique 2014*; 2014
- [11] Kechich A, Mazari B. La commande par mode glissant: Application à la machine synchrone à aimants permanents (approche linéaire). *Afrique. Science*. 2008;**4**(1):21-37
- [12] Ding Z, Wei G, Ding X. Speed identification and control for permanent magnet synchronous motor via sliding mode approach. *Systems Science & Control Engineering: An Open Access Journal*. 2014;**2**(1):161-167
- [13] Aimene M, Payman A, Dakyo B. Commande par platitude d'un système de conversion d'énergie éolienne à vitesse variable connectée au réseau. In *Symposium de Génie Electrique 2014*; 2014

- [14] Krstic M, Kanellakopoulos I, Kokotovic PV. Adaptive nonlinear control without overparametrization. *Systems & Control Letters*. 1992;**19**(3):177-185
- [15] Boussairi Y, Abouloifa A, Hamdoun A, Aouadi C, Lachkar I, Giri F. Nonlinear control of permanent magnet synchronous generator grid-connected applied to wind energy conversion system. In *Industrial Technology (ICIT), 2017 IEEE International Conference on*. IEEE; 2017. pp. 452-457
- [16] El Magri A, Giri F, Abouloifa A, Chaoui FZ. Robust control of synchronous motor through ac/dc/ac converters. *Control Engineering Practice*. 2010;**18**(5):540-553
- [17] Ohyama K, Arinaga S, Yamashita Y. Modeling and simulation of variable speed wind generator system using boost converter of permanent magnet synchronous generator. *European Conference on Power Electronics and Applications*; 2007. pp. 1-9
- [18] Boussairi Y, Abouloifa A, Hamdoun A, Aouadi C. Backstepping controller of grid connected wind energy conversion system with power factor correction. *International Journal of Computer and Information Technology*. September 2014;**03**(05); (ISSN: 2279 0764)
- [19] Dannehl J, Wessels C, Fuchs FW. Limitations of voltage-oriented PI current control of grid-connected PWM rectifiers with LCL filters. *IEEE Transactions on Industrial Electronics*. February 2009;**56**(2)
- [20] Wang X, Yuvarajan S, Fan L. Mpppt control for a pmsg-based grid-tied wind generation system. In *North American Power Symposium (NAPS)*. IEEE; 2010. pp. 1-7
- [21] Trejos-Grisales L, Guarnizo-Lemus C, Serna S. Overall description of wind power systems. *Ingenier'ia y Ciencia*. 2014;**10**(19):99-126
- [22] Wallmark O. *On Control of Permanent-Magnet Synchronous Motors in Hybrid-Electric Vehicle Applications*; 2004
- [23] Pahlevaninezhad M, Eren S, Bakhshai A, Jain P. Maximum power point tracking of a wind energy conversion system using adaptive nonlinear approach control engineering practice. *Applied Power Electronics Conference and Exposition*. 2010;**18**:540553

---

# DC-Link Control Schemes in Multilevel Converters for WECS

---

Carlos A. Reusser

Additional information is available at the end of the chapter

<http://dx.doi.org/10.5772/intechopen.72360>

---

## Abstract

The introduction of renewable energy resources since the late 1990s as an alternative to fossil energies has impact the development of wind energy and its integration to the grid. From the early 2000s, the wind energy has positioned itself as the most grown-up energy market in the world. This fact has introduced the need to deal with increasing power demands with limited generation capabilities, in terms of generator power density, for low rotation speeds and medium voltage generation within a grid interconnection in high voltage, and other grid code demands, like THD, power factor regulation, and the requirement of continuous operation under faulty condition. Until today, this issue has been solved using classical power converter topologies, using three-level voltage source converters (3LVSC) or multilevel configurations, such as neutral point clamped and cascaded H-Bridge topologies. In this chapter, the main advantages and drawbacks of classical multilevel converter topologies are analyzed, in terms of their DC-link voltage stability capability and different approaches to DC-link control and to new converter topologies, derived from classical topologies, are presented and compared with simulation results.

**Keywords:** multilevel converter, neutral point clamped, cascaded H-Bridge, modulation strategy, control scheme, voltage drift, model predictive control

---

## 1. Introduction

In the past decade, renewable energies like wind and solar energies have increased their participation in the global energy matrix, increasing from a 10% of the global energy market in 1993 to an 11% in 2011 with an estimated 16% in 2020. This in despite of fossil energies, which are experimenting a decrease with the passing years [1]. Among these resources, wind energy conversion systems have emerged as the leader at the present time. According to the

---

Global Wind Energy Council (GWEC) annual report, over 27 [GW] of new wind power generation capacity came online worldwide in 2008 representing a 36% growth rate in the annual market, bringing the total global wind power capacity to over 383 [GW] through the end of 2013. According to the global energy status report presented by the Global Wind Energy Council (GWEC), during the period 2015–2016, the installed capacity of renewable energies has experienced an estimated growth of around 47 [GW] on its total installed capacity. In these orders, the total worldwide installed power is capable to supply about a 23.7% of the global energy demands, representing half of the global demand growth. These facts have positioned wind energy as the leading energy source with a growth of 63 [GW] for the same period (**Figure 1**).

This indicates that there is a growing global demand for emissions-free wind power, which can be installed quickly, virtually everywhere in the world, making wind energy conversion one of the fastest growing sources of new electric generation.

From a technology point of view, an estimated of 330 manufacturers for commercial WECS have been identified in at least 40 countries [2], and another 300 are technology suppliers for parts, consulting and sales services. This development and maturity reached by the industry have among other drivers, cost reduction, increased efficiency, reliability and proprietary technology development.

One of the key technologies in WECS that has experienced extensive innovation in the last decade is the generator and power converter interface to the grid. Configurations have moved

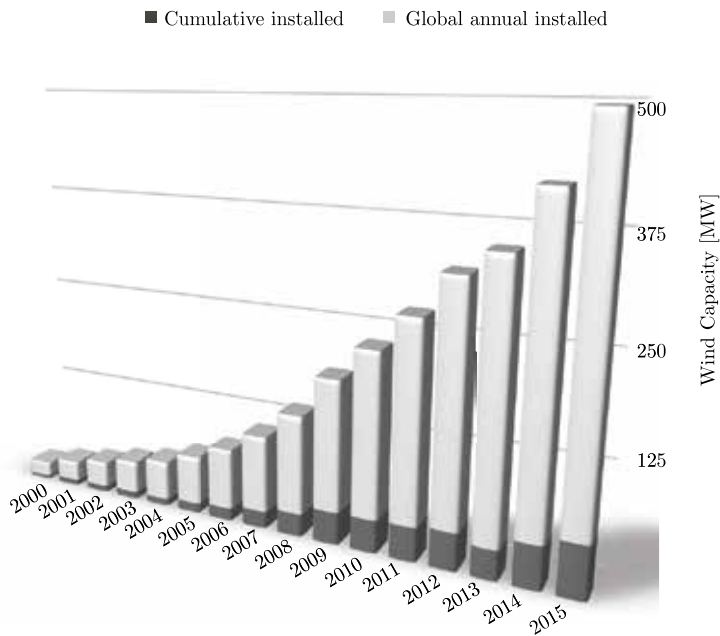


**Figure 1.** WECS penetration.

from fixed speed induction generators, going through partial capacity converter stage in doubly fed induction generators, to full-capacity converters used in synchronous generators (with wound rotor and permanent magnet rotor) [3]. They can be further divided depending if they feature a gearbox or not (gearless or direct-drive) or even a reduced gearbox (one stage). Combinations of different configuration types, generators, power converters and gear options have resulted in several commercial turbines and proprietary technology [3, 4]. In **Figure 2**, the possible configurations for a WECS solution are presented.

### 1.1. Fixed-speed WECS

Fixed-speed configurations were introduced in the 1980s, and they are equipped with squirrel cage induction generators (SCIG) or wound rotor induction generators (WRIG), connected directly to the grid. They are designed to obtain maximum efficiency at rated wind speed. In a fixed-speed WECS, the turbine speed is determined by the grid frequency, the generator pole pair number, the machine slip and the gearbox ratio. A change in the wind speed will not affect

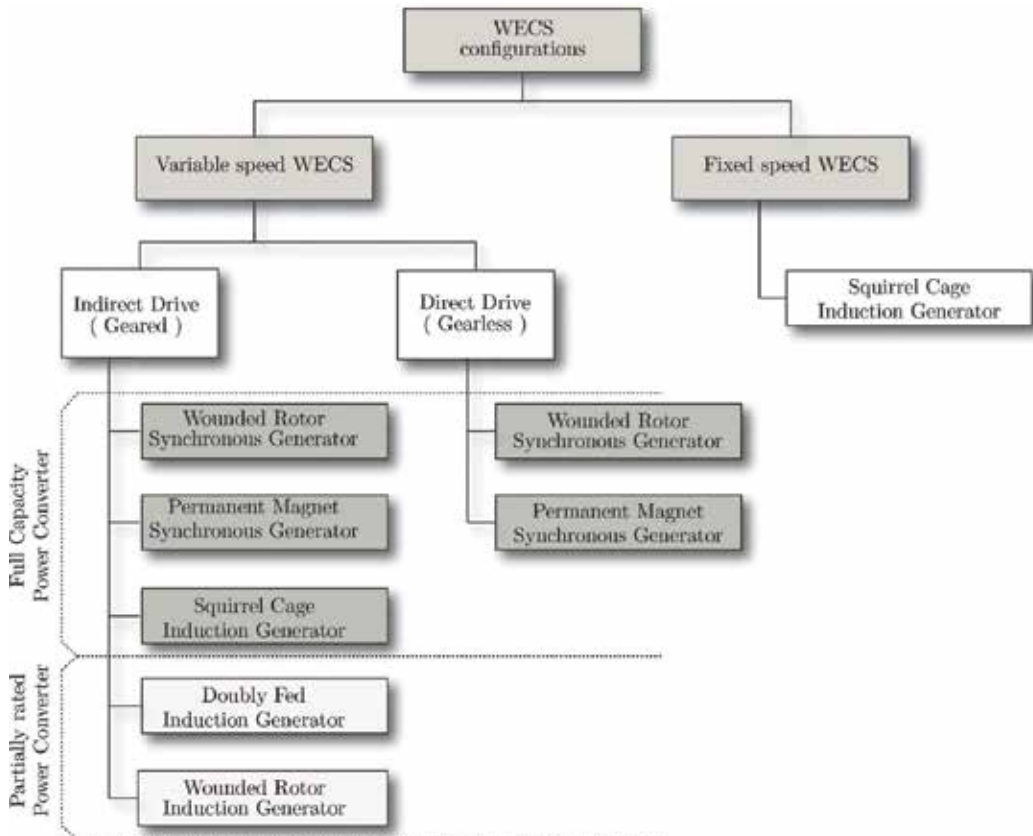


**Figure 2.** WECS configurations.

the turbine speed to a large extent but will increase the electrical output power. In order to increase the output power, some of these configurations use generators with two sets of windings: one is used for low wind speeds (typically eight pole pairs) and the other for medium and high wind speeds (typically four to six pole pairs).

Power control is achieved aerodynamically either by stall, active stall or pitch control. A soft starter is normally fitted in order to reduce the inrush current during start-ups. Also, a reactive power compensator is needed to reduce the generator reactive power demand as presented in **Figure 3**.

The advantages of this WECS configuration are its simplicity, robustness and reliability. Its drawbacks are the uncontrollable reactive power consumption, mechanical stress and no power quality control [5].

**1.2. Variable-speed WECS**

Variable-speed configurations were developed first in the 1990s with the introduction of the doubly fed induction generator (DFIG) and the wound rotor induction generator (WRIG). These WECS configurations are designed to achieve maximum electrical power output over a wide range of wind speeds, by using a maximum power point tracking (MPPT) control technique. In this way, the generator rotational speed  $\omega_r$  is adapted in such a proportion to the wind speed  $v_s$ , to keep the turbine tip speed ratio  $\lambda^1$  corresponding to the turbine maximum performance power.

In the early 2000s, variable speed WECS configuration was extended to the use of wound rotor synchronous generators (WRSG) and permanent magnet synchronous generators (PMSG) including the extended use of multipole and multiphase configurations and full-scale power electronics.

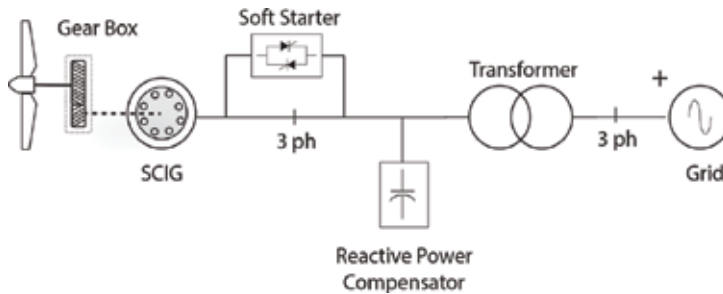


**Figure 3.** SCIG fixed-speed WECS configuration.

<sup>1</sup>The ratio between the tangential speed of the tip of a blade and the actual velocity of the wind.

Variable speed WECSs are generally divided into two categories, depending on the way of interconnecting the generator to the grid. This are:

1. Partially rated power electronics
2. Full-scale power electronics interfacing wind turbines

### 1.2.1. Partially rated power electronics

In partially rated power electronics configurations, the generator is connected directly to the grid via a power transformer. The first configuration uses a WRIG fitted with an external resistance, which is controlled by means of power electronics as presented in **Figure 4**. This controlled resistance acts as a dynamic slip controller, and it gives typically a speed range of 2–5%. The power converter has to be designed for handling low voltage but high currents. At the same time, an extra control freedom is obtained at higher wind speeds in order to keep the output power fixed. This solution still needs a soft starter and a reactive power compensator, which is in continuous operation.

The second solution is based on a DFIG generator fitted with back-to-back power converter in parallel as presented in **Figure 5**. This configuration allows full frequency control by controlling the rotor slip, by means of adjusting the rotor winding frequency.

In this case, the power goes from the stator to the grid, while the rotor current is controlled via a four-quadrant back-to-back converter. This configuration enables power flow from stator and rotor to the grid. If the generator is running sub-synchronously, then the electrical power is only delivered into the rotor from the grid. On the other hand, if the generator is running super-synchronously (above the synchronous speed), electrical power is delivered through both, the rotor and the stator, which represents a big improvement respect to the WRIG configuration.

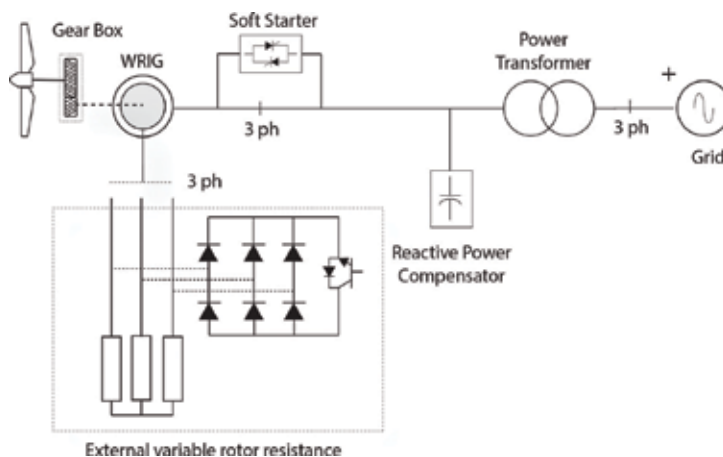


**Figure 4.** WRIG with external variable resistance configuration.

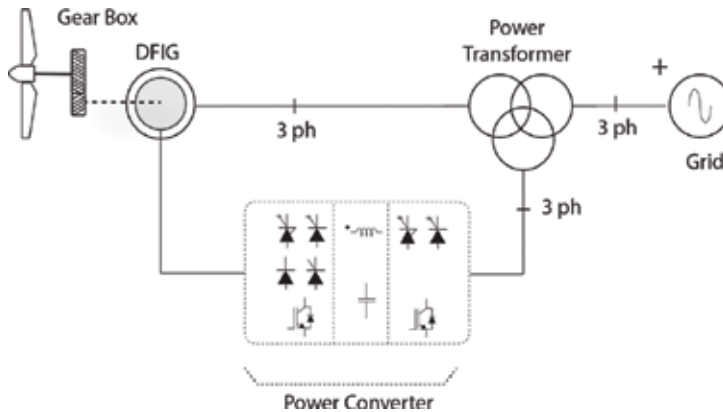


**Figure 5.** DFIG with partially rated power electronics configuration.

### 1.2.2. Full-scale power electronics

In the late 2000s, the concept of full-scale power electronics (FSPE) for WECS was introduced. It considers the generator connected to the grid via a power converter. This configuration allows a complete control of the active and reactive power transferred to the utility while operating the generator in its optimum TSR, hence maximum power output. It also has made possible the use of bigger generators, in terms of rated power. As a consequence, wind power conversion has been optimized over the entire speed range, and maintenance costs have been reduced dramatically. Traditional gearbox becomes optional because FSPE allows the wind turbine to work at low speeds. In addition FSPE enables full decoupling between the generator and the grid allowing the implementation of maximum TSR control scheme, for the generator, and voltage-oriented control (VOC) with full active and reactive power control for the inverter stage. These features introduced by FSPE have given WECS the capability to participate actively in grid voltage/frequency regulation, with capability to support the grid under faulty operation conditions (in the range of DC-link voltage stability) [6].

Full-scale power electronics WECS can be implemented in geared or gearless configurations, using squirrel cage induction generators (SCIG), permanent magnet synchronous generators (PMSG) or wound rotor synchronous generators (WRSG) in geared or gearless implementations as presented in **Figure 6**.

## 2. Control requirements for WECS converter topologies

WECS integration to the grid has also driven to new technological challenges, specifically in the field of wind generator maximum tolerable voltage levels and power converter topologies, for high power ratings. Today, the most accepted solutions for high power ratings are based in variable speed WECS with full-scale power electronics configurations, using multilevel power converters, where back-to-back topologies like neutral point clamped (NPC), active neutral point clamped (ANPC) and cascaded H-Bridge (CHB) converters, shown in **Figure 7**, have



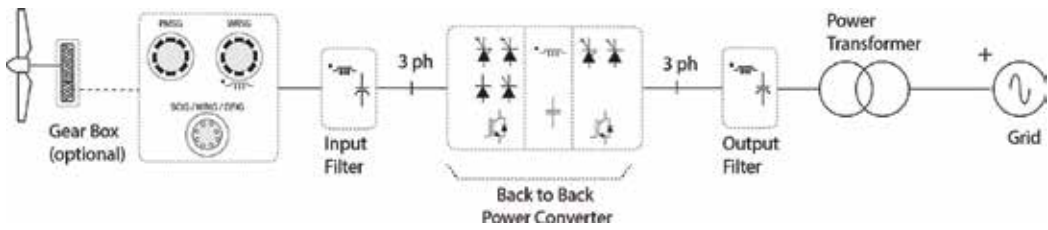


Figure 6. Full-scale power electronics configuration.

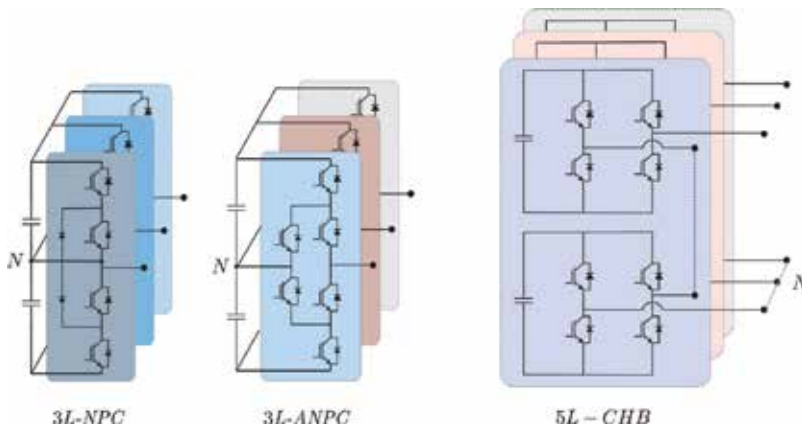


Figure 7. NPC, ANPC and CHB topologies.

become very popular solutions for most large-scale wind-farm projects, because these topologies have reached their technological maturity, proven during the past couple of decades as referred in [7, 8].

In order to serve as a proper generator-grid power flow interface, WECSs have to accomplish with the following control goals, which leave to two different control loops to be analysed:

1. Maximum generator power operation (maximum power tracking control MPPT)
2. DC-link voltage control and balance
3. Grid current control (active and reactive power)

### 2.1. Generator side control loop

The generator output power depends upon the accuracy to track the different TSR points for a given wind condition as presented in Eq. (1):

$$P_w = \frac{1}{2} C_p \rho A \left( \frac{\omega_r r}{\lambda_T} \right)^3 \quad (1)$$

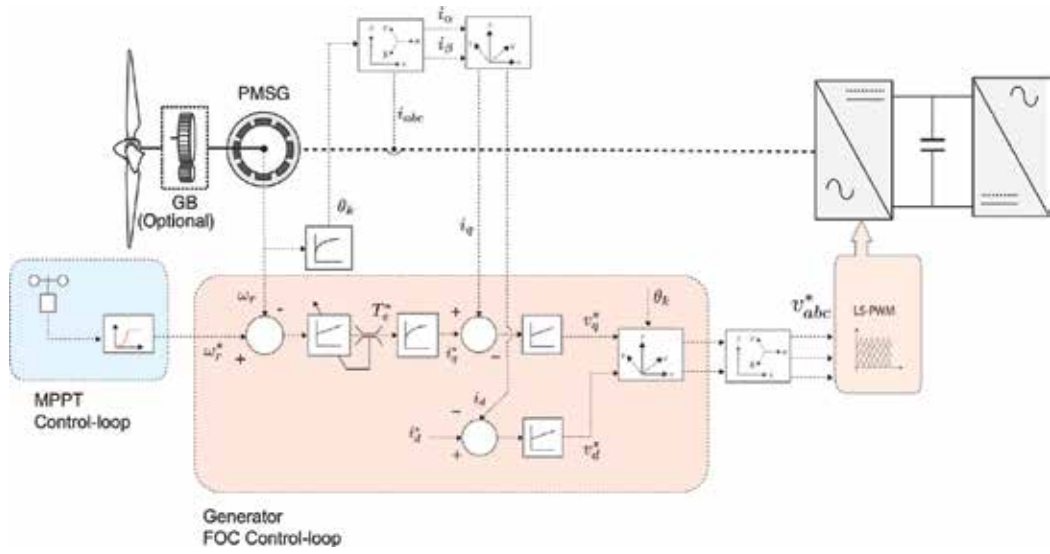


Figure 8. Generator side control scheme.

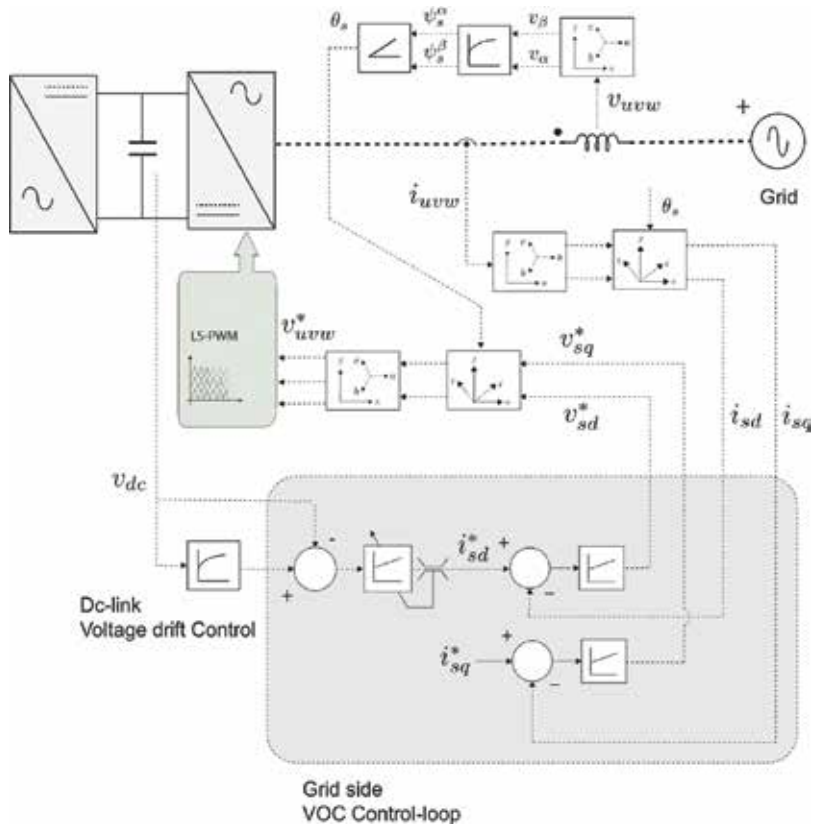


Figure 9. Grid side control scheme.

So as presented previously, the active power delivered by the generator is dependent on  $\lambda_T$ , so maximum active power is reached via a maximum power point tracking (MPPT) control scheme [6, 9, 10]. The control scheme implementation is shown in **Figure 8**.

## 2.2. Grid side control loop

Grid side control is achieved via active and reactive power control [11, 12]. Active and reactive power delivered to the grid is controlled by the means of power decoupling in the synchronous rotating reference frame  $dq$ , which is given by Eqs. (2)–(3). Decoupling is achieved using virtual flux voltage-oriented control (VF-VOC) strategy or via a PLL orientation:

$$P = \frac{3}{2} \Re\{v^d (i^d + ji^q)\} \quad (2)$$

$$Q = \frac{3}{2} \Im\{v^d (i^d + ji^q)\} \quad (3)$$

Thus, by setting  $i^q = 0$ , it is possible to maximize the active power flow into the grid. However, this control scheme requires of a synchronous reference frame orientation  $\theta_k$ , which is provided by a virtual-flux space vector  $\Psi_L$  (4), and its implementation is shown in **Figure 9**:

$$\psi_o^{(\alpha\beta)} = \int_0^t v^{(\alpha\beta)}(\tau) d\tau \quad (4)$$

$$\theta_k = \text{atan2}(\psi_o^\alpha, \psi_o^\beta) \quad (5)$$

## 3. Power converter DC-link stability

As presented in the previous section in Eqs. (2)–(3), active and reactive power stable power flow, from the generator to the grid, is highly dependent on the DC-link voltage  $v_d$  stability. Moreover, DC-link voltage level is directly dependent on the power harvested from the wind speed and stored in the DC-link capacitor and then converted and rejected to the grid and consumer centres. Both stages are controlled by the converter modulation strategy. Thus, the modulation strategy and the converter topology have a preponderant incidence, in the power flow stability and the DC-link voltage stability as a consequence.

In this matter, the main issue for multilevel power converters in FSPE configuration is referred to the fact that most of the time generators will be operating at a fraction of their rated power, so in order to deal with this fact, multilevel converters have to operate within their low modulation index region. This represents a major concern in the case of the NPC and ANPC topologies.

### 3.1. Modulation strategies

#### 3.1.1. Sinusoidal pulse width modulation (SPWM)

For multilevel topologies, level-shifted PWM (LS-PWM) strategy has become a standard as modulation strategy for these topologies, because it is suitable for any multilevel converter topology and presents low harmonic distortion [13, 14]. The switching pattern for a LS-PWM

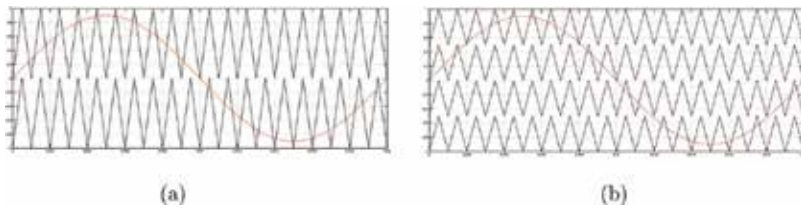


**Figure 10.** Level-shifted PWM. (a) 3 level converter LS-PWM scheme (b) 5 level converter LS-PWM scheme.

scheme consists of  $(\ell - 1)$  triangular carriers and  $\ell$  number of levels to be synthesized, as shown in **Figure 10**.

*3.1.1.1. Cascaded H-Bridge topology*

The cascaded H-Bridge (CHB) converter consists of an arrangement of series-connected unit cells (per leg), each one consisting an H-Bridge voltage source converter, with isolated DC-sources.

For the 5L-CHB converter basic cell in **Figure 11**, the corresponding switching states are presented in **Table 1** as follows.

The isolated cell structure of the CHB converter and its floating condition with respect to ground prevents the NP current flow; hence, no voltage unbalance on each cell DC-link appears. This is due to the fact that only a single current path is established on each switching cycle. So the energy flow direction is the same for each cell DC-link capacitor.

The main drawback of the CHB converter is the large number of isolated DC supplies and the high number of components.

*3.1.1.2. Neutral point clamped topology*

Considering the 3L-NPC converter basic cell shown in **Figure 12**, the generated switching states are summarized in **Table 2**.

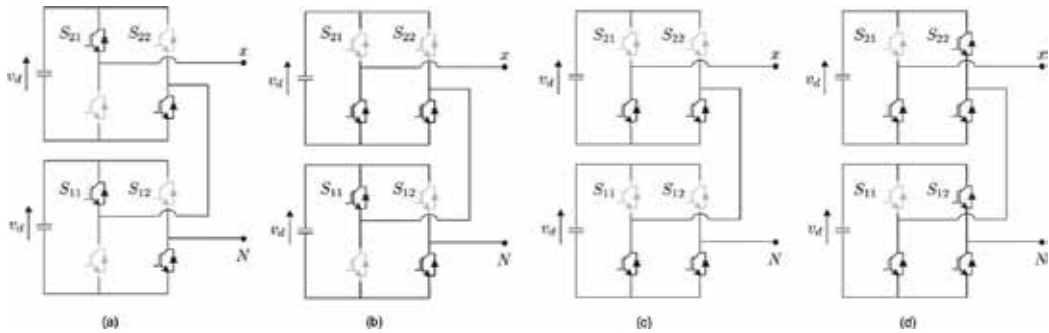


**Figure 11.** CHB LS-PWM switching states: (a)  $2E$  state, (b)  $E$  state, (c) zero state and (d)  $-2E$  state.

$S_{11}$	$\bar{S}_{11}$	$S_{21}$	$\bar{S}_{121}$	$v_{xN}$
1	0	1	0	$2v_d$
1	0	1	1	$v_d$
1	0	0	0	
1	1	1	0	
0	0	1	0	
0	0	0	0	0
1	0	1	1	
1	1	0	0	
1	1	1	1	
0	0	0	1	
0	1	1	0	
0	1	1	1	$-v_d$
0	1	0	0	
1	1	0	1	
0	0	0	1	
0	1	0	1	$-2v_d$

**Table 1.** 5L-CHB switching states per leg using LS-PWM (fundamental cell).

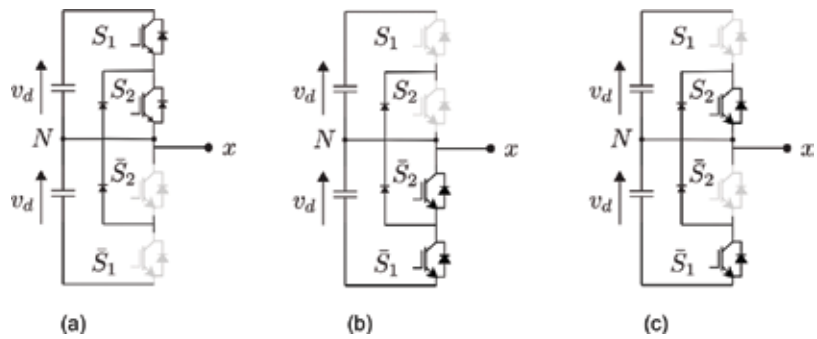


**Figure 12.** NPC LS-PWM switching states: (a) P state, (b) N state and (c) zero state.

	$S_1$	$\bar{S}_1$	$S_2$	$\bar{S}_2$	$v_{xN}$
P	1	0	1	0	$v_d$
0	0	1	1	0	0
N	0	1	0	1	$-v_d$

**Table 2.** 3L-NPC switching states per leg using LS-PWM (fundamental cell).

The main drawback of the neutral point clamped topologies is that depending on the switching state and modulation index, they develop neutral point (NP) circulating currents, which leads to unbalance in the DC-link capacitors, because of an uneven energy flow to and from the DC-link capacitors, driving to unsymmetrical voltages. The NP circulating current  $i_o$  can be expressed as in Eqs. (6) and (7):

$$i_o = S_{x0} i_x + S_{y0} i_y + S_{z0} i_z \quad (6)$$

$$S_{x0}, S_{y0}, S_{z0} \in [0, 1] \quad (7)$$

where  $S_{x0}$   $S_{y0}$   $S_{z0}$  are the corresponding zero switching states for each phase  $xyz$ , given the voltage references as in Eq. (8):

$$\begin{cases} v_x^*(t) = m \sin(\omega_s t) \\ v_y^*(t) = m \sin\left(\omega_s t - \frac{2\pi}{3}\right) \\ v_z^*(t) = m \sin\left(\omega_s t + \frac{2\pi}{3}\right) \end{cases} \quad (8)$$

where  $m$  stands for the modulation index and  $\omega_s$  the modulating reference frequency; then, the output currents can be expressed as in Eq. (9):

$$\begin{cases} i_x(t) = \hat{I} \sin(\omega_s t + \phi) \\ i_y(t) = \hat{I} \sin\left(\omega_s t - \frac{2\pi}{3} + \phi\right) \\ i_z(t) = \hat{I} \sin\left(\omega_s t + \frac{2\pi}{3} + \phi\right) \end{cases} \quad (9)$$

with  $\phi$  the power factor corresponding to the operating condition. The duty cycle for switches  $d_k$  and  $\bar{d}_x$  can be expressed as

$$d_x \begin{cases} m \sin(\omega t) & \omega t \in [0, \pi] \\ 0 & \omega t \in [\pi, 2\pi] \end{cases} \quad (10)$$

$$\bar{d}_k \begin{cases} 1 & \omega t \in [0, \pi] \\ 1 + m \sin(\omega t) & \omega t \in [\pi, 2\pi] \end{cases} \quad (11)$$

Expressing Eq. (7) in terms of their duty cycles can be expressed as in Eq. (12):

$$i_o = \sum_k (d_k - \hat{d}_k) i_k \quad \forall k = x, y, z \quad (12)$$

From Eqs. (8)–(12), the average NP circulating current can be found to be as in Eq. (13):

$$I_o = |d_x - \hat{d}_x| i_x + |d_y - \hat{d}_y| i_y + |d_z - \hat{d}_z| i_z \quad (13)$$

As presented in **Figure 13**, the zero switching state establishes a path for which NP current  $i_o$  can flow, leading to voltage unbalance in the DC-link capacitors.

A solution for the problem of NP circulating current can be achieved by means of the modulation scheme, in particular by choosing two modulating signals  $v_{kp}$  and  $v_{kn} \quad \forall k = x, y, z$ , such that:

$$\begin{cases} v_{kp} = \frac{v_k + \min\{v_x, v_y, v_z\}}{2} \\ v_{kn} = \frac{v_k - \max\{v_x, v_y, v_z\}}{2} \end{cases} \quad (14)$$

### 3.1.2. Space vector modulation (SVM)

#### 3.1.2.1. Neutral point clamped topology

Space vector modulation (SVM) strategy enables the possibility to use some redundant switching states, as presented in **Table 3**.

Due to the nature (type) of each vector, with respect to its corresponding switching state, different voltage space vectors will have different effects on the voltage drift of the DC-link capacitors. This effect can be summarized as follows:

- Zero voltage space vectors  $v_0$  have no effect on voltage deviation.
- Small vectors  $V_k \forall k \in [1, \dots, 6] \quad k \in \mathbb{Z}$  have a predominant effect on the voltage drift by raising or decreasing the neutral point voltage.
- In Medium vectors  $V_k \forall k \in [7, \dots, 12] \quad k \in \mathbb{Z}$  in this case, the effect of the switching state cannot be determined exactly, so NP voltage will raise or decrease depending on the system state.
- Large vectors  $V_k \forall k \in [12, \dots, 18] \quad k \in \mathbb{Z}$  have no influence on the voltage drift.

In order to deal with voltage drift, the dwell time of a small vector can be equally distributed within both redundant switching states, over a sampling period, depending on the sector of

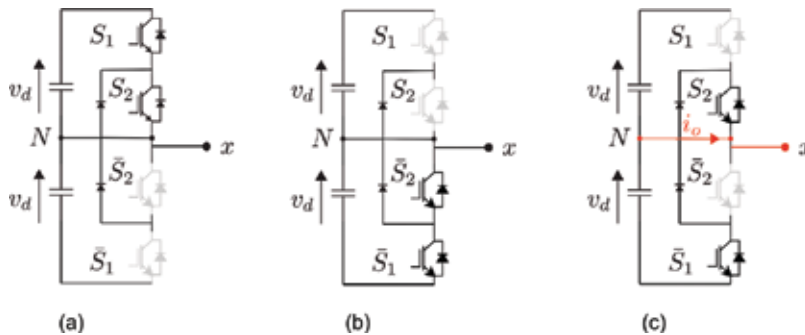


**Figure 13.** NPC LS-PWM switching states: (a) P state, (b) N state and (c) zero state.

Space vector	Switching state	Type	Magnitude
$V_0$	[0 0 0] [P P P] [N N N]	Zero vector	0
$V_1$	[P 0 0] [0 N N]	Small vector	$\frac{1}{3} v_d$
$V_2$	[P P 0] [0 0 N]		
$V_3$	[0 P 0] [N 0 N]		
$V_4$	[0 P P] [N 0 0]		
$V_5$	[0 0 P] [N N 0]		
$V_6$	[P 0 P] [0 N 0]		
$V_7$	[P 0 N]	Medium vector	$\frac{\sqrt{3}}{3} v_d$
$V_8$	[0 P N]		
$V_9$	[N P 0]		
$V_{10}$	[N 0 P]		
$V_{11}$	[0 N P]		
$V_{12}$	[P N 0]		
$V_{13}$	[P N N]	Large vector	$\frac{2}{3} v_d$
$V_{14}$	[P P N]		
$V_{15}$	[N P N]		
$V_{16}$	[N P P]		
$V_{17}$	[N N P]		
$V_{18}$	[P N P]		

**Table 3.** 3L-NPC switching states per leg using SVM (fundamental cell).

the reference space vector. In other words, redundant switching states can be used to minimize the voltage drift effect. However, depending on the reference space vector amplitude (in other words depending on the desired modulation index), the proposed scheme will be more or less effective; thus, when medium vectors are involved, the voltage drift will be a consequence of the load state.

### 3.1.3. Finite-set model predictive control (FSMPC)

As presented previously, SVM scheme introduces more degrees of freedom, compared to the SPWM method, and as a consequence, redundant switching states are obtained. By selecting



the appropriated space vector and switching sequence, the flow of a neutral point current can be mitigated. However, some switching states have an unknown effect on the NP current, so its effect on the DC-link voltage stability is not clearly defined.

Moreover, SVM leads to high computational cost and complexity, especially when the number of voltage levels increases. It has also to be clarified that due to the unknown behaviour of some switching states in the NP current and the dwell time limitation, the circulating neutral point current is not mitigated at all, as stated in [15, 16].

In order to deal with these constraints, which cannot be solved using classical linear modulation techniques, and to accomplish with the DC-link stability control requirements, finite-set model predictive control (FS-MPC) appears as an available and powerful control scheme, whose control action will select the most appropriated voltage space vector, to fulfil some control goals, via the minimization of a imposed cost function.

The FCS-MPC approach eliminates the need of linear controllers and modulation scheme. This approach is basically an optimization algorithm whose actuation depends on a discrete-time model of the converter switching pattern and its interaction with the load/grid and DC-link. In other words, it depends on how the energy flows from the DC-link to the load/grid and how the voltage on the DC-link is affected by these dynamics.

### 3.1.3.1. Load/grid model

Considering the converter-grid model presented in **Figure 14**, the following mathematical model given in Eq. (15) can be established:

$$v_{jN}(t) = R_s i_j(t) + L_s \frac{d}{dt} i_j(t) - e_j(t) \quad \forall j = \{a, b, c\} \quad (15)$$

By rotating the space vector state variables of (15) into a stationary reference frame  $\alpha\beta$  and expressing the mathematical model in the state space form, Eqs. (16) and (17) are obtained:

$$\frac{d}{dt} i_s^\alpha(t) = \frac{1}{L_s} [v_s^\alpha(t) - e_g^\alpha(t) - R i_s^\alpha(t)] \quad (16)$$

$$\frac{d}{dt} i_s^\beta(t) = \frac{1}{L_s} [v_s^\beta(t) - e_g^\beta(t) - R i_s^\beta(t)] \quad (17)$$

where  $v_s^\alpha(t)$  and  $v_s^\beta(t)$  can be expressed in terms of generated voltage space vector  $v_s^{\alpha\beta}$  as a function of the switching state  $S_i$  and the DC-link voltage  $v_{dc}$ , so

$$v_s^{(\alpha\beta)} = f(S_i, v_{dc}, t) \quad (18)$$

$$v_s^\alpha = \Re \left\{ v_s^{(\alpha\beta)} \right\} \quad (19)$$

$$v_s^\beta = \Im \left\{ v_s^{(\alpha\beta)} \right\} \quad (20)$$

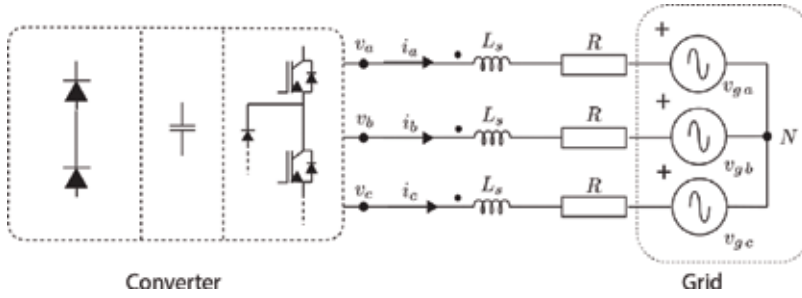


Figure 14. Grid converter model.

The model given in Eqs. (19) and (20) is converted into its discrete-time expression for a given sampling time  $T_s$ , approximating the derivative using the backward Euler approximation Eq. (21):

$$\frac{d}{dt} x(t) = \frac{x[k+1] - x[k]}{T_s} \quad (21)$$

So the discretised load/grid model in the  $\alpha\beta$  stationary reference frame is given in Eqs. (22) and (23):

$$i_s^\alpha[k+1] = \Lambda_1 \left( v_s^\alpha[k] - e_g^\alpha[k] \right) + \Lambda_2 i_s^\alpha[k] \quad (22)$$

$$i_s^\beta[k+1] = \Lambda_1 \left( v_s^\beta[k] - e_g^\beta[k] \right) + \Lambda_2 i_s^\beta[k] \quad (23)$$

with  $\Lambda_1 = \frac{T_s}{L_s}$ ,  $\Lambda_2 = \left(1 - \frac{L_s}{R} T_s\right)$ , and the grid voltage space vector  $e_g^{(\alpha\beta)}$  can be treated as the system internal perturbation  $d_i$ :

$$i_s^{(\alpha\beta)}[k+1] = \Lambda_1 (f(S_n, v_{dc}, k) - d_i[k]) + \Lambda_2 i_s^{(\alpha\beta)}[k] \quad (24)$$

### 3.1.3.2. DC-link model

The DC-link capacitor voltage dynamics are defined by Eq. (25):

$$i_{dc(\ell)}(t) = C \frac{d}{dt} v_{dc(\ell)}(t) \quad \forall \ell = \{Up, Low\} \quad (25)$$

The discrete-time model for Eq. (25) can be obtained as in Eq. (26):

$$v_{dc(\ell)}[k+1] = v_{dc(\ell)}[k] + \Gamma i_{dc(\ell)}[k] \quad (26)$$

with  $\Gamma = \frac{T_s}{C}$ ; it must be also noted that the capacitor current flow  $i_{dc(\ell)}$  is a function of the switching state  $S_n$  and the current flow to the load/grid  $i_s$  as given in Eq. (27):

$$i_{dc(\ell)} = h(S_i, v_{dc}, k) \quad (27)$$

### 3.1.3.3. Model predictive control algorithm

The objectives of the MPC control algorithm are the following:

- Obtain the desired output load current fixed by the reference.
- Minimize the DC-link capacitor voltage drift.

To deal with these constraints, a cost function is build, whose objective is to minimize the quadratic error, between the reference and the predicted value of the state variable  $x[k + 1]$ , given a switching state  $S_i$ . The cost function  $g_i$  can be expressed as in Eq. (28):

$$g_i = w_1 \sum_{i=1}^n \left( i_s^{*(\alpha\beta)}[k + 1] - i_s^{(\alpha\beta)}[k + 1] \right)^2 + w_2 \sum_{i=1}^n \left( v_{dc(t)}^*[k + 1] - v_{dc(t)}[k + 1] \right)^2 \quad (28)$$

In Eq. (28),  $w_1$  and  $w_2$  are weighting factors used to give the priority to the control the state variables and must be adjusted for each system in particular. The switching state to be synthesized  $S_n$  will result from the optimization of the cast function  $g_n$  given as in (29)

$$S_i = \min \{g_i\} \quad (29)$$

Using the predictive model for the system state variables given in Eqs. (24) and (26), and the cost function optimization presented in Eqs. (28) and (29), the MPC algorithm can be constructed as the flow diagram presented in **Figures 15** and **16**.

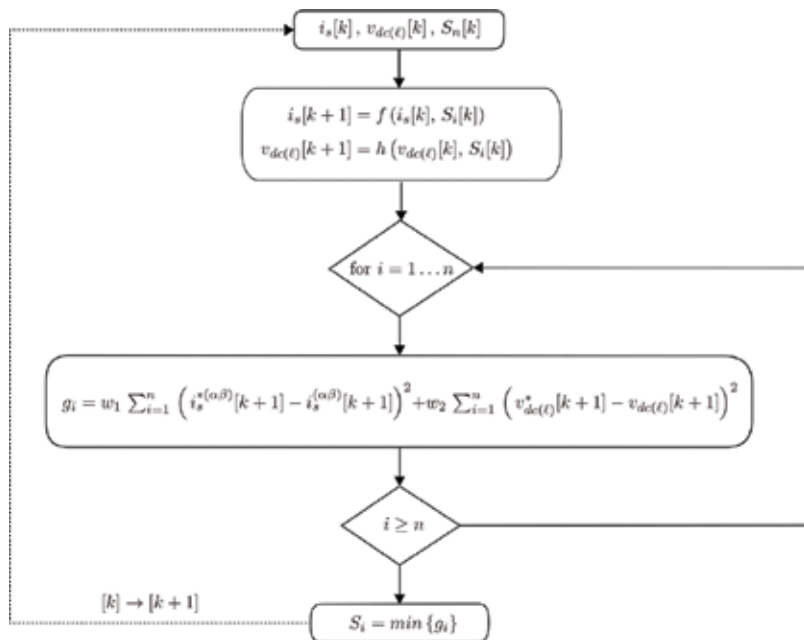


**Figure 15.** MPC algorithm.

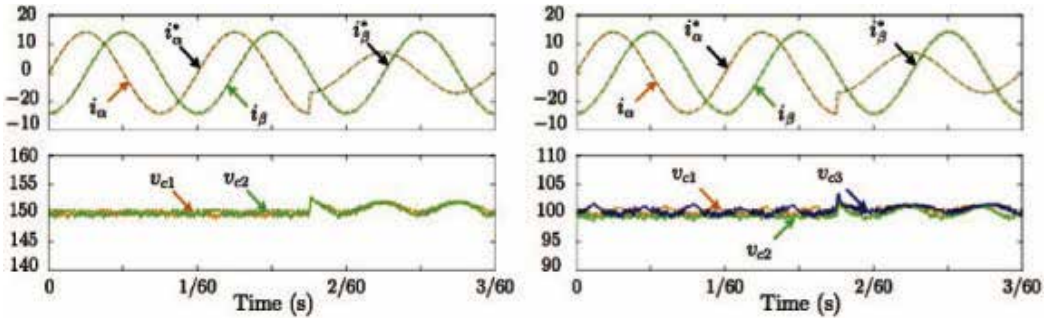


Figure 16. MPC simulation results.

### 3.1.4. The direct power control approach

Direct power control strategy is based on the power flow balance between the power source, e.g. the wind turbine generator system, and the output power, which is demanded by the grid and the power stored in the DC-link interface. So, the apparent power is known to be as in Eqs. (30) and (31):

$$S = v i^* \quad (30)$$

$$S = p + jq \quad (31)$$

Active and reactive power components can be written in the  $\alpha\beta$  stationary reference frame as in Eq. (32):

$$\begin{cases} P_s = v_s^\alpha i_s^\alpha + v_s^\beta i_s^\beta \\ Q_s = v_s^\alpha i_s^\beta - v_s^\beta i_s^\alpha \end{cases} \quad (32)$$

Active and reactive power flow is given by the instantaneous variation of active and reactive power as written in Eq. (33):

$$\begin{cases} \frac{d}{dt} P_s = v_s^\alpha \frac{d}{dt} i_s^\alpha + i_s^\alpha \frac{d}{dt} v_s^\alpha + v_s^\beta \frac{d}{dt} i_s^\beta + i_s^\beta \frac{d}{dt} v_s^\beta \\ \frac{d}{dt} Q_s = v_s^\alpha \frac{d}{dt} i_s^\beta + i_s^\alpha \frac{d}{dt} v_s^\beta - v_s^\beta \frac{d}{dt} i_s^\alpha - i_s^\beta \frac{d}{dt} v_s^\alpha \end{cases} \quad (33)$$

The power stored in the DC-link capacitor is given Eq. (34):

$$S_{dc} = v_d S_k i_s \quad (34)$$

where  $S_k$  stands for the switching state vector of the converter and can be defined as in Eq. (35):

$$S_k = [S_1 \ S_2 \ S_3]^T \quad (35)$$

In the case of the NPC converter,  $S_k$  is represented per phase, so  $k \in \{a, b, c\}$ .

The DC-link voltage dynamics can be written as in Eq. (36), so

$$C \frac{d}{dt} v_c = S_k i \quad (36)$$

The generator can be considered as a symmetrical three-phase voltage source, so the corresponding voltages in the stationary reference frame  $\alpha\beta$  are to be found as Eqs. (37) and (38):

$$v_\alpha = \widehat{V}_s \sin(\omega t) \quad (37)$$

$$v_\beta = -\widehat{V}_s \sin(\omega t) \quad (38)$$

Active and reactive power dynamics can be computed using Eq. (33) and taken the converter-grid model presented in Eq. (15) into consideration, building the following model, based on the power flow:

$$P[k+1] = P[k] + f_{pi}[k] T_s \quad (39)$$

$$Q[k+1] = Q[k] + f_{qi}[k] T_s \quad (40)$$

## 4. New converter topologies for WECS

Since most WECS operate in low voltage, they require parallel connection of several converters to be able to handle all the power. An alternative to parallel connection has been adopted by mainstream manufacturers by providing multiple three-phase winding outputs of the generator enabling the connection of back-to-back converters as independent channels to the grid. In this field of application, the dual three-phase generator or multiple three-phase winding generators have become a popular solution.

As presented previously, multichannel configurations are commonly based on 3L-NPC topologies, which introduce DC voltage drift and a linear increasing number of semiconductors and capacitors as function of the number of channels (number of multiple generator windings). These facts introduce the idea of new converter topologies, capable of handling multiple three-phase groups, at the same time, with a single DC-link.

In this line of research, a nine-switch back-to-back topology for wind energy conversion system, as shown in **Figure 17**, is proposed [17–19]. The topology is derived from two three-phase voltage source converters that share a positive and a negative busbar, respectively. Hence three switches are eliminated of the 12 needed for a back-to-back configuration. This comes at expense of some forbidden switching states and limitations in the modulation index of one of the converters, which depends on the difference of the input and output converter frequencies.

### 4.1. Converter modulation

Unlike the conventional 12-switch back-to-back converter topology, the 9-switch topology introduces some restrictions for the rectifier and inverter modulation. The allowed switching states per leg referred to rectifying stage of the converter **Figure 18** are shown in **Table 4**.

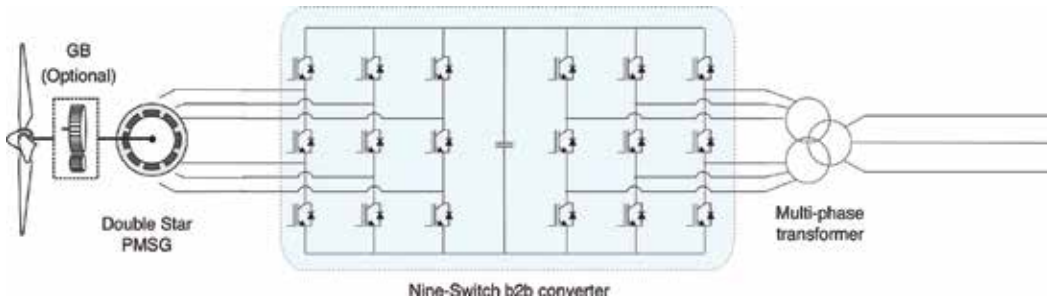


Figure 17. Nine-switch converter back-to-back topology.

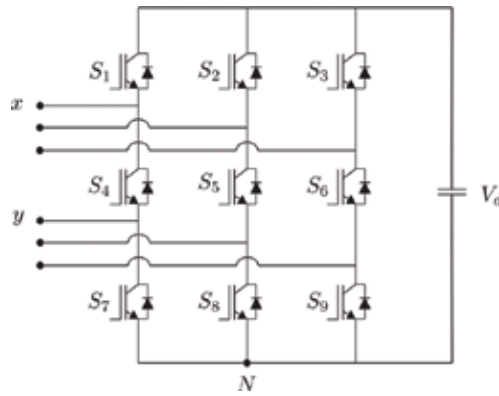


Figure 18. Nine-switch converter topology, rectifying stage.

$S_1$	$S_4$	$S_7$	$v_{xN}$	$v_{yN}$
	1	0	$V_d$	$V_d$
	0	0	0	0
	0	1	$V_d$	0

Table 4. Allowed switching states (one leg shown).

The modulation strategy proposed is a classical 12-switch back-to-back converter PWM modulation, where the restrictions for the middle switches are obtained from Figure 19 and implemented as follows:

$$S_j = \bar{S}_{j-3} \oplus S_{j+3} \quad \forall j \in [4, 5, 6] \tag{41}$$

Thus, the DC-link enables the decoupling of the generator and grid side, then constant frequency mode modulation scheme can be implemented; thus, both voltage reference space vectors having a constant phase shifting angle  $\delta$  will always to be found at least in contiguous sectors; then in this case, the maximum modulation index is given by Eq. (42):

$$m = \frac{1}{\sqrt{3}} \tag{42}$$

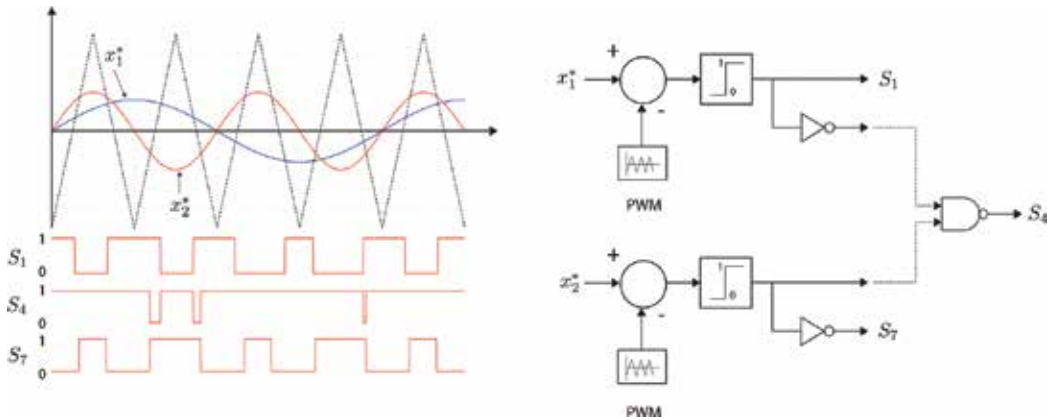


Figure 19. Nine-switch converter modulation strategy implementation.

#### 4.2. DC-link voltage control

DC-link voltage control is achieved using a modified structure of the active and reactive control scheme presented in Eqs. (2)–(3) in Section 2.2 of this chapter.

A virtual flux-oriented control (VFOC) strategy with active and reactive control is implemented for each inverter output. The active power delivered by the inverter is used to control the DC-link capacitor voltage, while the reactive power is set on each three-phase output group to obtain unity power factor operation, just as a common back-to-back VSC. The control implementation for one channel is shown in Figure 20.

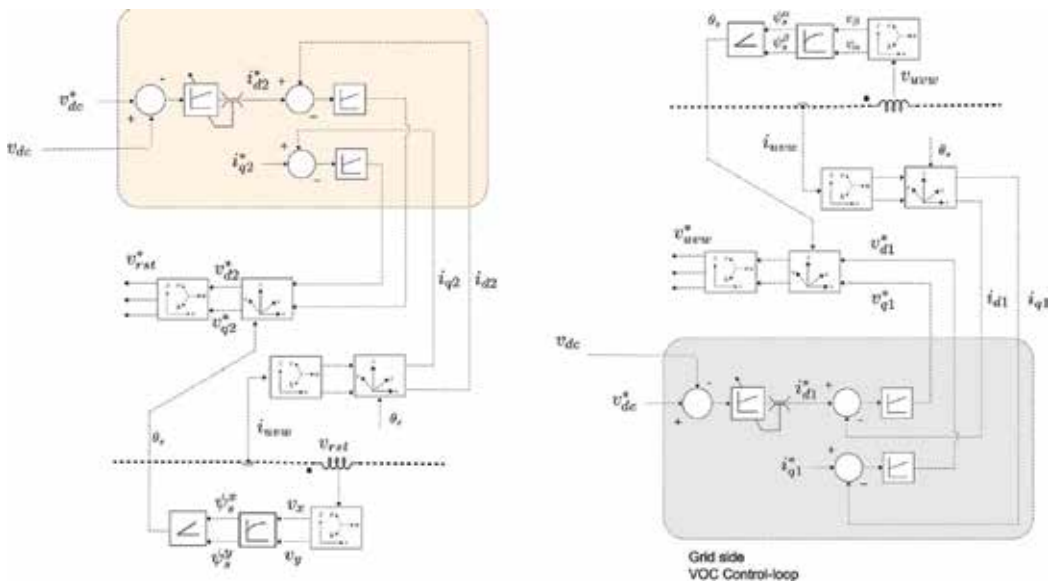


Figure 20. Nine-switch converter grid side control scheme.

Results for the generator side performance are shown in **Figure 21**. In **Figure 21(a)** and **(b)**, during the speed step-up, no electrical torque is produced, thus allowing the mechanical torque to speed up the generator as shown in **Figure 21(a)**. Once the wind turbine reaches the speed reference  $\omega_r^*$  provided by the MPPT controller, the electrical torque starts to build up, until it reaches the desired setting point, converging to its steady state; the FOC outer loop PI controller ensures zero steady-state speed error, while the inner control loop ensures  $i_q$  current, hence mechanical torque tracking.

In **Figure 22**, a derivation of the previously topology is presented, but in a multiphase, multichannel configuration, so each nine-switch converter is providing dual power flow. This fact forces the converter to operate in VFM modulation mode, thus reducing the DC-link modulation index.

### 4.3. Future work

The nine-switch converter topology has proven to have many advantages to deal with multiphase, multichannel WECS configurations, by having the ability to manage simultaneously different voltage space vector references in a single DC-link capacitor. This feature ensures a simple control scheme, based in active and reactive power control.

Future work on this converter topology includes the research on MBPC and sliding mode control of the nine-switch converter in back-to-back and bidirectional configurations.

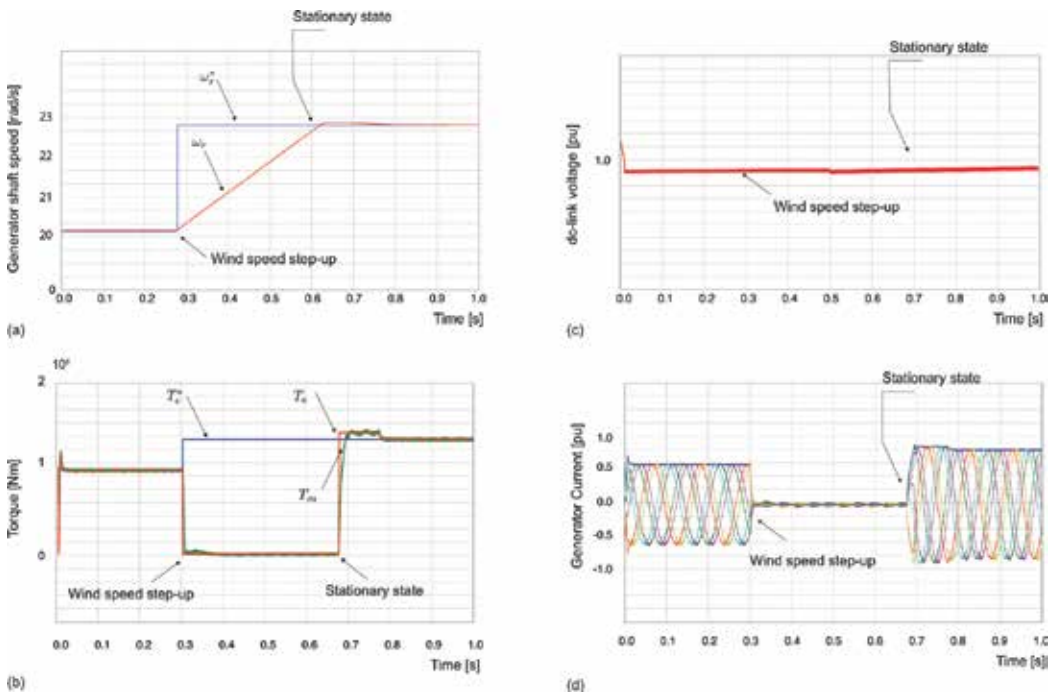


**Figure 21.** Generator side simulation results: (a) rotor speed, (b) torque, (c) DC-link voltage and (d) generator side currents.



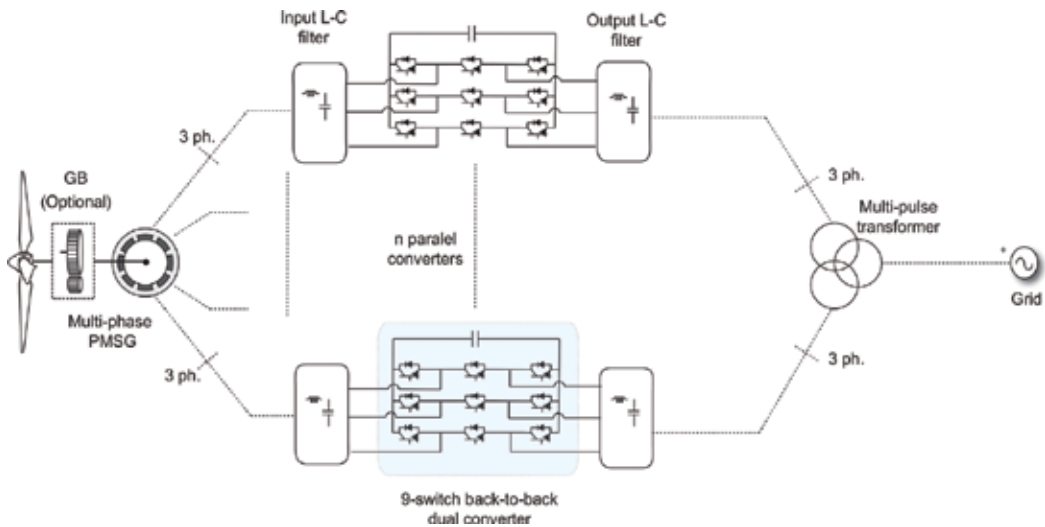


Figure 22. Multichannel nine-switch converter topology.

## 5. Conclusions

In this chapter, an overview on WECS is presented with the main focus on full-scale power converters employed with a squirrel cage, permanent magnet and wound rotor synchronous generators. With the combination of different types of generators and power converters, a variety of WECS configurations have been investigated. Various technical issues related to CHB and NPC multilevel converter configurations were discussed referred to their DC-link voltage stability as function of its modulation scheme.

The operating principle of the FCS-MPC strategy is presented for ideal and implementation cases. The cost function flexibility and potentiality in achieving different control and technical requirements are discussed. The generalized approach based on FS-MPC strategy has been presented for multilevel NPC converters. The dynamics of the load/grid currents and DC-link capacitor voltages are formulated as a function of switching states and the mathematical prediction model of the converter. The proper selection of the switching states leads to the minimization of the cost function. It has to be noted that the weighting factors assigned to each term on the cost function are dependent on the operational requirements and the stability of the mathematical model. The proposed method shows an intuitive and promising approach to balance the DC-link capacitor voltages, even with the perturbations in the system model.

The main drawback of NPC converter topologies is the requirement of neutral point current compensation, due to the natural path established in some switching states. On the other hand, for CHB converter topologies, no neutral point current is allowed to flow, due to its floating neutral condition, leading to DC-link voltage stability.

DC-link voltage stability is hardly related not only to the grid side active and reactive power demands and voltage symmetry but also to the power converter topology and modulation

strategy. As presented, neutral point clamped topologies are more attractive from the point of view of the multilevel voltage output wave form, which has better performance in terms of THD and grid code compatibility. On the other side, H-Bridge-based topologies present a better DC-voltage stability and simpler control schemes. In these fields, the nine-switch converter appears as suitable alternative. An extensive study with the implementation of MPC and sliding mode control for the nine-switch topology has to be undertaken, to evaluate its performance under grid fault operation and to evaluate restricted switching states and voltage stability.

## Author details

Carlos A. Reusser

Address all correspondence to: carlos.reusser@usm.cl

Department of Electronics, Universidad Tecnica Federico Santa Maria, Valparaiso, Chile

## References

- [1] W. E. Council. World Energy Resources 2013 Survey. World Energy Council. 2013; pp. 1-468
- [2] REN21. Renewable Energy Policy Networks for the 21st Century. Renewables 2014 Global Status Report. 2015. www.ren21.net
- [3] Wu B, Lang Y, Zagari N, Kouro S. Power Conversion and Control of Wind Energy Systems. Vol. 24. Wiley-IEEE Press; Aug 6, 2011. ISBN-10: 0470593652; ISBN-13: 978-0470593653
- [4] Blaabjerg F, Liserre M, Ma K. Power electronics converters for wind turbine systems. IEEE Transactions on Industry Applications. March-April 2012;48(2):281-290
- [5] Lubosny Z. Wind Turbine Operation in Electric Power Systems: Advanced Modeling, Vol. 1. Springer; December 2010
- [6] Teodorescu R, Liserre M, Rodriguez P. Grid Converter Structures for Wind Turbine Systems. Wiley-IEEE Press; 2011. pp. 123-143
- [7] Kouro S, Malinowski M, Gopakumar K, Pou J, Franquelo LG, Wu B, Rodriguez J, Perez MA, Leon JI. Recent advances and industrial applications of multilevel converters. IEEE Transactions on Industrial Electronics. Aug 2010;57(8):2553-2580
- [8] Rodriguez J, Rivera M, Kolar J, Wheeler P. A review of control and modulation methods for matrix converters. IEEE Transactions on Industrial Electronics. Jan 2012;59(1):58-70
- [9] Thongam JS, Bouchard P, Ezzaidi H, Ouhrouche M. Wind speed sensorless maximum power point tracking control of variable speed wind energy conversion systems. In: 2009

- IEEE International Electric Machines and Drives Conference. Miami, FL; 2009. pp. 1832-1837. DOI: 10.1109/IEMDC.2009.5075452
- [10] Srighakollapu N, Sensarma P. Sensorless maximum power point tracking control in wind energy generation using permanent magnet synchronous generator, 2008 34th Annual Conference of IEEE Industrial Electronics. Orlando, FL; 2008. pp. 2225-2230
- [11] Malinowski M, Kazmierkowski M, Trzynadlowski A. A comparative study of control techniques for pwm rectifiers in ac adjustable speed drives. *IEEE Transactions on Power Electronics*. Nov 2003;**18**(6):1390-1396
- [12] Busca C, Stan A-I, Stanciu T, Stroe D. Control of permanent magnet synchronous generator for large wind turbines. In: 2010 IEEE International Symposium on Industrial Electronics (ISIE); July 2010. pp. 3871-3876
- [13] Tolbert LM, Peng FZ, Habetler TG. Multilevel pwm methods at low modulation indices. *IEEE Transactions on Power Electronics*. Jul 2000;**15**(4):719-725
- [14] Bin W. *High-Power Converters and AC Drives*. 1st ed. Wiley-IEEE Press; 2006. pp. 1-468
- [15] Shu Z, He X, Wang Z, Qiu D, Jing Y. Voltage balancing approaches for diode-clamped multilevel converters using auxiliary capacitor-based circuits. *IEEE Transactions on Power Electronics*. May 2013;**28**(5):2111-2124
- [16] Busquets-Monge S, Bordonau J, Rocabert J. A virtual-vector pulsewidth modulation for the four-level diode-clamped dc-ac converter. *IEEE Transactions on Power Electronics*. July 2008;**23**(4):1964-1972
- [17] Reusser CA, Kouro S. Nine switch multi-channel dual converter for WECS. In: 41st Annual Conference of the IEEE Industrial Electronics Society, IECON 2015; Nov 2015. pp. 005363-005368
- [18] Reusser CA, Kouro S. Back-to-back wind energy conversion system configuration based on 9-switch dual converter and open-end-winding PMSG. In: 2015 IEEE 13th Brazilian Power Electronics Conference and 1st Southern Power Electronics Conference (COBEP/SPEC); Nov 2015. pp. 1-6
- [19] Reusser CA, Kouro S, Cardenas R. Dual three-phase pmsg based wind energy conversion system using 9-switch dual converter. In: 2015 IEEE Energy Conversion Congress and Exposition (ECCE); Sept 2015. pp. 1021-1022

*Edited by Francisco Beltran-Carbajal*

This book focuses on recent and innovative methods on vibration analysis, system identification, and diverse control design methods for both wind energy conversion systems and vibrating systems. Advances on both theoretical and experimental studies about analysis and control of oscillating systems in several engineering disciplines are discussed. Various control devices are synthesized and implemented for vibration attenuation tasks. The book is addressed to researchers and practitioners on the subject, as well as undergraduate and postgraduate students and other experts and newcomers seeking more information about the state of the art, new challenges, innovative solutions, and new trends and developments in these areas. The six chapters of the book cover a wide range of interesting issues related to modeling, vibration control, parameter identification, active vehicle suspensions, tuned vibration absorbers, electronically controlled wind energy conversion systems, and other relevant case studies.

Published in London, UK

© 2018 IntechOpen  
© Bet\_Noire / iStock

**IntechOpen**

